Fall 1994

Dosimetry of High-Energy Heavy-Ion Beams Using Energy-Dependent Green's Functions

Sang Yull Chun
Old Dominion University

DOSIMETRY OF HIGH-ENERGY HEAVY-ION BEAMS USING ENERGY-DEPENDENT GREEN'S FUNCTIONS

by

Sang Yull Chun
M.S. May 1988, Hampton University

A Dissertation submitted to the Faculty of
Old Dominion University in Partial Fulfillment of the
Requirement for the Degree of

DOCTOR OF PHILOSOPHY

PHYSICS

OLD DOMINION UNIVERSITY

September, 1994

Approved by:

_____
Govind S. Khandelwal (Director)

_____

_____

_____

ABSTRACT

DOSIMETRY OF HIGH-ENERGY HEAVY-ION BEAMS
USING ENERGY-DEPENDENT GREEN'S FUNCTIONS

Sang Yull Chun

Old Dominion University, 1994
Director: Dr. Govind S. Khandelwal

A theoretical description of the transport of high-charge and high-energy (HZE) ion bombardment of biological tissue is developed. The energy-dependent Green's functions and particle fluxes are obtained for two boundary distributions – the monoenergetic and the Gaussian. Approximate energy-dependent Green's functions for the collision terms are obtained for computational simplicity. As an application of the energy-dependent Green's function method, dosimetric quantities, such as dose, dose-equivalent, and average quality factor, for 600A MeV ^{56}Fe, 517A MeV ^{40}Ar, and 625A MeV ^{20}Ne ion beams incident on a water target are obtained and compared with the values obtained from the energy-independent Green's function method and existing experimental values.

DEDICATION

This work is dedicated to my parents whose patience and understanding have made this endeavor possible.

ACKNOWLEDGMENTS

First of all, I would like to express my sincere appreciations to two distinguished physicists, Prof. Govind S. Khandelwal and Dr. John W. Wilson. Without the direction and strong encouragement of my advisor, Prof. Govind S. Khandelwal, this dissertation would not have been completed. I deeply thank my research advisor at NASA Langley Research Center, Dr. John W. Wilson, for his thoughtful guidance and great patience throughout the period of my research.

I thank my dissertation committee members for giving me direction and advice. Especially, I thank Prof. John H. Heinbockel for helping me correct many mistakes in this dissertation. I thank the chairman and other faculty members in this department who guided me through their courses and lectures. I thank Dr. Lawrence W. Townsend for encouraging me to pursue my academic goals.

I would like to express very special appreciation to my wife for her understanding and assistance.

This work was supported by the Langley Research Center, National Aeronautics and Space Administration under Research Grant NCC1-42.

TABLE OF CONTENTS

LIST OF TABLES

LIST OF FIGURES

CHAPTER 1
INTRODUCTION

The interaction of a living organism with high-charge and high-energy (HZE) ions has become an increasingly important area of radiation protection physics because of the hazard the ions pose for biological systems.[1–7] The correct estimation of the biological damage by heavy ions is very difficult, however, due to the production of secondary heavy ions by primary or incident heavy ions. Recently, special attention has been paid to the safety of crew members in spacecraft[8,9] and airplanes flying at high altitudes[6,10–12] since biological damage can be produced by the cosmic rays, which contain heavy ions. As more extensive space-travel occurs, and as more new airline routes are opened near the earth's pole to save time and fuel, possible biological damage to the crew members and passengers by heavy ions in cosmic rays will increase.

Clearly, there is a need to shield spacecraft and high-altitude aircraft against heavy ions in cosmic rays. Therefore, it has been necessary to develop theoretical and computational benchmark models in order to understand the complex reaction mechanism so that possible physical damage can be estimated. In addition, it is important to understand this complicated process in radiation therapy.[13] Since the charges of heavy ions are relatively large and correspondingly require thick shielding structures, the correct estimate of biological damage due to heavy ions is very crucial in estimating the cost of shielding and radiotherapy.

In the present work, an efficient and simple heavy-ion transport model is studied to predict particle fluxes and radiobiological dosimetric quantities, such as dose, dose-

equivalent, and average quality factor. Using a deterministic method, approximate solutions of the heavy-ion transport equation are derived. Since our attention is mainly on the heavy ions in cosmic rays, especially galactic cosmic rays, we also review their compositions[14] and characteristics.

1.1 HEAVY IONS IN COSMIC RAYS

In these days, many individuals are exposed to possible radiation sources in their routine jobs. In addition to the radioactivity from accidental and experimental releases at nuclear facilities and other installations, occupational exposure to natural radiation sources and medical exposure for radiation therapy are our major concerns. Obviously, there exist more potential biological damages due to these natural and artificial radiation sources than ever before.

The most important natural radiation sources are "cosmic rays." As a primary radiation source, cosmic rays are mainly divided into two groups: solar cosmic rays and galactic cosmic rays. The solar cosmic rays consist of energetic particles produced by solar flares or solar wind, and their composition and intensity are strongly affected by solar activity.[5] The galactic cosmic rays have fairly low fluxes with high energies; by contrast, the solar cosmic rays have high fluxes with relatively low energies. Not only the flux of galactic cosmic rays, which is consistently high at low-altitude, but the sudden rise of a radiation level due to the emission of the high-energy solar particles, which can arrive at the earth's surface within approximately 30 minutes, affects the safety of crew members and passengers in spacecraft or high-altitude airplanes.[5]

To describe the possible biological damage by cosmic radiation, we take an example from reference 10 and reference 11. The ICRP (International Commissions on Radiological Protection) recommendation[15] for a pregnant woman is approximately 2 mSv ($\propto$ MeV/g) for the entire pregnancy, with the recommendation that the exposure in any month should not exceed 0.5 mSv. As shown in Figure 1.1 which is taken

from reference 10, the average dose-equivalent rate profile along the aircraft flight trajectories at 17 km from the earth's surface is around 17 μSv per hour for the fligh route of New York to Tokyo. If a pregenant woman stays 30 hours per month in flight as a crew member or as a passenger, not only the monthly dose-equivalent, at the current stage of the solar cycle, but the accumulated dose-equivalent in a four-month period exceeds the pregnancy limit of the ICRP recommendation.

Next, let us look at the composition of cosmic rays. As shown in Table 1.1 and in Figure 1.2,[14] the most dominant constituent of cosmic radiation is the proton. Around 5 to 10 percent consists of alpha particles. The heavy ions comprise only less than 1 percent. Even though the abundance of heavy ions in cosmic rays is quite small, the heavy ions in cosmic rays are very important in a description of radiation protection. It has been known that the relative abundance of heavy ions in cosmic rays increases rapidly by three or four orders of magnitude above the galactic background level during solar activity.[5] In addition, heavy ions in cosmic rays have relatively large energies and can penetrate very thick shielding materials, although they have low intensity and short ranges. The high-charge of heavy ions causes them to produce very dense tracks inside a shielding material,[16] and such intense ionization can cause severe biological damages.

The low-energy protons and alpha particles in cosmic rays, which make up approximately 95 to 98 percent of the total flux, induce reactions that produce other heavy ions, protons, and neutrons from residual nuclei. The produced heavy ions induce other secondary productions. The secondary particles produced in this heavy-ion cascade process contain many neutrons. These secondary neutrons penetrate shielding materials very easily without decreasing the dose rate inside the shielding.[17,18] As a result, there exists very strong concern to prevent possible biological damages due to heavy ions in cosmic rays.

1.2 DYNAMIC MODELING OF TRANSPORT PROCESS

To model the transport process of heavy ions in cosmic rays, we should understand the nature of the energy spectra of cosmic rays. The differential energy spectra of cosmic rays are shown as a function of kinetic energy per nucleon in Figure 1.3.[16] The energy spectra of the various major components of cosmic rays indicate that proton, deuteron, alpha particle and other heavier ions follow very similar propagation mechanism, although their spectral intensity varies with the type of ion. The energy spectrum is roughly expressed in terms of a power law as $N(E)\mathrm{d}E = kE^{\gamma}\mathrm{d}E$, where k and γ are appropriate constants, and $N(E)$ is the number of nuclei with kinetic energy E.

Even though very close similarities can be noticed for the individual reaction events, the overall interaction schemes and tracks are different. For example, in the production of cascade particles by high-energy protons and alpha particles in the earth's atmosphere, the alpha particles initiate more cascade processes and have wider tracks.[1,14,16] For heavy ions, such as ^{56}Fe with charge $Z = 26$, the tracks are very dense and relatively wide, compared to those of protons. In addition, the relative rate of energy loss of heavy ions is several hundred times higher than that of protons.

To construct a transport model for the propagation of heavy ions inside a medium, we must consider the interaction mechanism of charged particles in the medium. When a high-energy nucleon, as a primary radiation source, passes through a medium, it will either penetrate the medium without interacting with constituent electrons or nuclei, or it will lose energy by interacting with atomic electrons (electronic collision) and with the nucleons inside a nucleus (nuclear interaction). These interactions may be elastic or inelastic. In moving through a target material, the charged particle loses its energy mainly by electronic collisions. As the incident energy of ions gets higher, however, the nuclear interactions play a major role in the energy loss mechanism. These interactions of heavy ions with a target nucleus result in a cascade process in

which other nuclear fragments (target fragments or projectile fragments) are ejected due to the secondary production of particles. These characteristic processes are linked dynamically.

The energy spectra of attenuated particles and produced particles after the collision can be calculated using many exisiting dynamic models. The result depends on the geometry and the composition of shielding structure. To estimate the biological damage of nucleons and heavy ions, an efficient method to evaluate charged particle spectra is very important. Since the simplicity of the model is the most critical factor for more complex applications to estimate the radiobiological damage of radiation, there have been many investigations for simple benchmark calculations.[19] The computational efforts to generate radiobiological data, such as dose, dose-equivalent, and linear energy transfer (LET) distribution, have ranged from the Monte Carlo method[20,21] to the Green's function method[22,23]. These are categorized mainly by two methods: (1) statistical approach, such as the Monte Carlo method, and (2) deterministic method, such as the Discrete-Ordinate method,[24,25] and the Green's function method.

In principle, the radiation transport calculations with very complex geometry are well suited to the Monte Carlo method. In the deterministic method, one solves an appropriate heavy-ion transport equation analytically to obtain the solution of the heavy-ion transport equation.[26] In the Monte Carlo method, computational efforts are very stiffly increased to evaluate a statistical error, and it is very difficult to handle the large amount of data. On the other hand, the analytical method to solve heavy-ion transport equation is very difficult due to the nonlinearlity of the problem. Since there exist many difficulties in the statistical method, the deterministic method has been continuously developed in order to obtain the solution of the heavy-ion transport equation[26–30] even though this method is limited to one-dimensional applications. Since heavy-ion transport equation is an integro-differential equation, it is very hard

to get an analytical solution even for a simple geometry. With several customary assumptions for the sake of simplicity, there have been many investigations[22,23,26–30] to obtain analytical solutions and their approximations.

1.3 GREEN'S FUNCTION METHOD

The analytical solution and other approximations[22,23] of the Boltzmann-like heavy-ion transport equation have been derived by Wilson up to the first-collision term[26] assuming that heavy ions penetrate a shielding material one-dimensionally. Wilson's heavy-ion transport equation is given by

$$\left\{\vec{\Omega}\cdot\nabla-\frac{1}{A_j}\frac{\partial}{\partial E}S_j(E)+\sigma_j(E)\right\}\phi_j(\vec{x},E,\hat{\Omega})$$

$$=\sum_{k>j}\int \mathrm{d}E'\,\mathrm{d}\vec{\Omega}'\,\sigma_{jk}(E,E',\hat{\Omega},\hat{\Omega}')\,\phi_k(\vec{x},E',\hat{\Omega}') \qquad (1.1)$$

where $\phi_j(\vec{x},E,\hat{\Omega})$ is the number of the ions of type j with atomic mass A_j in a volume element at $\vec{x}$ traveling within $\mathrm{d}\hat{\Omega}$ about $\hat{\Omega}$ with an energy between E and $E+\mathrm{d}E$, $\sigma_j(E)$ is the macroscopic cross section of the ions of type j (total probability of collisions per unit distance traveled along the $\vec{x}$-direction with energy E), $S_j(E)$ is the corresponding energy loss per unit length (stopping power), and $\sigma_{jk}(E,E',\hat{\Omega},\hat{\Omega}')$ is the production cross section of the fragment ions of type j by the collision of the ions of type k with energy E' and direction $\vec{\Omega}'$. The lefthand side in Eq. (1.1) represents the drift of particles and the collisional particle losses due to atomic collisions and nuclear interactions. The righthand side represents the production of particles. The major advantage of Wilson's approach is that a single particle balance equation is derived for describing atomic processes as well as nuclear processes. Compared to the statistical approaches, Wilson's solution technique[26] for obtaining an analytical solution is relatively simple and efficient, but still provides a high computational

accuracy even with the straight-ahead approximation.[29]

In the recent studies of Wilson et al.,[22,23] it is shown that the Green's function method provides a better solution technique. In the Green's function method, an arbitrary solution of the Boltzmann equation within a closed region is written as a superposition of the products of Green operators and the incident flux at its boundary. The Green's function method for a realistic (laboratory) beam distribution at the boundary meets the objective of space-validated codes.[22] Using the superposition rule, the solution of Eq. (1.1) is obtained as[31]

$$\phi_j(\vec{x},E,\vec{\Omega}) = \sum_m \int G_{jm}(\vec{x}-\vec{x}_\Gamma,\hat{\Omega}-\hat{\Omega}',E,E') \times \phi_m(\vec{x}_\Gamma,\hat{\Omega}',E')\,\mathrm{d}\vec{x}_\Gamma\,\mathrm{d}\hat{\Omega}'\mathrm{d}E' \tag{1.2}$$

where $\phi_m(\vec{x}_\Gamma,\hat{\Omega}',\vec{E}')$ is the incident beam distribution at the boundary $\vec{x}_\Gamma$.

In Eq. (1.2), the solution $\phi_j(\vec{x},E,\vec{\Omega})$ can be expressed as a complete series of the Green's functions, and this method is called the perturbative Green's function method. It also can be obtained in terms of approximate Green's functions, so called the nonperturbative Green's function method. In the perturbative Green's function method, the solution is obtained up to the highest-order term such that the contribution of higher-order collision terms is negligible. The main impetus for developing approximate solutions with the nonperturbative method is because of the computational simplicity, and this aspect is well demonstrated elsewhere.[22,23] Even for a one-dimensional case, the energy-dependent perturbative method requires tremendous computational time and cost.

1.4 OBJECTIVES OF THE PRESENT WORK AND SUMMARY

The computational results of perturbative and nonperturbative Green's function methods show reasonable agreement with experimental values.[22,23] However, in the

previous Green's function approach, there exists a major limitation for it to be a realistic computational model. This is the assumption that nuclear cross sections are independent on the collision energy. In the previous Green's function methods,[1,22,23] the nuclear cross sections in Eq. (1.1) are assumed such that $\sigma_j(E) \approx \sigma_j$ and $\sigma_{jk}(E, E', \hat{\Omega}, \hat{\Omega}') \approx \sigma_{jk}$. We will call this method "the energy-independent Green's function method." This assumption is reasonable for the transport of high-energy and heavy ions because nucleon-nucleon cross sections and, correspondingly, nucleus-nucleus cross sections are almost constant above $1A$ GeV. However, nucleon-nucleon cross sections and nucleus-nucleus cross sections below $1A$ GeV vary drastically with energy. There is no clear justification of the use of the energy-independent method below $1A$ GeV. To check the validity of the energy-independent Green's function method below $1A$ GeV and to obtain optimized values of the energy-independent nuclear cross section for the energy-independent Green's function method, the construction of energy-dependent formalism is inevitable. In the present work, energy-dependent nuclear cross sections are used, and we call the method "the energy-dependent Green's function method."

One of the main objectives of this work is to develop a solution technique for the energy-dependent Green's function method and to understand the energy-dependence of the nuclear cross section in the solution of the energy-dependent Green's function method. After evaluating the energy-dependent Green's function, we obtained particle fluxes and compared them with experimental values. In addition, dose and dose-equivalent values for 517A MeV ^{40}Ar, and 625A MeV ^{20}Ne ion beams are obtained for monoenergetic and Gaussian distributions at the boundary. Since previous Green's function methods are based on the multiple charged-ion approach[1,26,27] with the straight-ahead approximation[29] and the velocity conserving assumption,[27] we also use these assumptions in the present work.

In this work, we develop approximate energy-dependent Green's functions since

exact solutions are too complex for a numerically efficient code. For higher-order perturbative solutions, we make use of nonperturbative methods.[23] The contribution of the higher-order terms is obtained by the use of the approximate Green's functions without the ionization-loss since nuclear interaction is a dominant process for high-energy incident ion beams. The development of the approximate energy-dependent Green's functions is based on the fact that the range of ions below $1A$ GeV is on the order of one or two nuclear mean free paths. As a result, the energy-dependence of the nuclear cross section will be apparent only in the first generation or in the second generation of secondary ion fragments. The first few interaction terms are evaluated from the perturbation theory with full energy-dependence, and approximate energy-dependent Green's functions are constructed to approximate collision terms.

To summarize, the transport mechanism of energetic and heavy ions is formulated using a particle balance equation, so called the Boltzmann heavy-ion transport equation. The nuclear fragmentation cross sections are generated through a simple nuclear reaction model. While the previous Green's function method to solve the Boltzmann heavy-ion transport equation is based on energy-independent nuclear fragment cross sections, the present approach uses energy-dependent nuclear cross sections. The present approach resolves a major deficiency in the Green's function method. With the straight-ahead approximation[29] and the velocity conserving assumption,[27] the energy-dependent solution of the heavy-ion transport equation is derived. Computational efficiency is achieved by developing approximate energy-dependent Green's functions. We compare the calculated results with the values obtained from the energy-independent Green's function method, and check the validity of these approximations. We calculate particle fluxes and other dosimetric quantities, such as dose, dose-equivalent, and average quality factor for $517A$ MeV ^{40}Ar, and $625A$ MeV ^{20}Ne ions incident on a water target. We compared the calculational results with the experimental values measured on the Lawrence Berkley

Laboratory BEVALAC accelerator.[32–34]

In Chapter II, we show a solution technique for the energy-dependent heavy-ion transport formalism. The approximate Green's functions are also developed in this chapter. Chapter III is for describing nuclear and atomic data bases, which we used to generate transport coefficients. In Chapter IV and Chapter V, we present computational results. The energy-dependent Green's function, particle flux, depth-dose distribution, and quality factor are discussed. In Chapter VI, we summerize the present work and discuss possible directions for future work.

Table 1.1. Abundances of nuclei in cosmic rays relative to hydrogen.

Element	Abundances
Hydrogen	1
Helium	1.5×10^{-1}
Lithium, Berylium, Boron	2.3×10^{-3}
Carbon, Nitrogen, Oxygen	8.7×10^{-3}
Neon	2.0×10^{-3}
Iron	7.6×10^{-4}
All other Heavy Ions	$\approx 1.5 \times 10^{-7}$

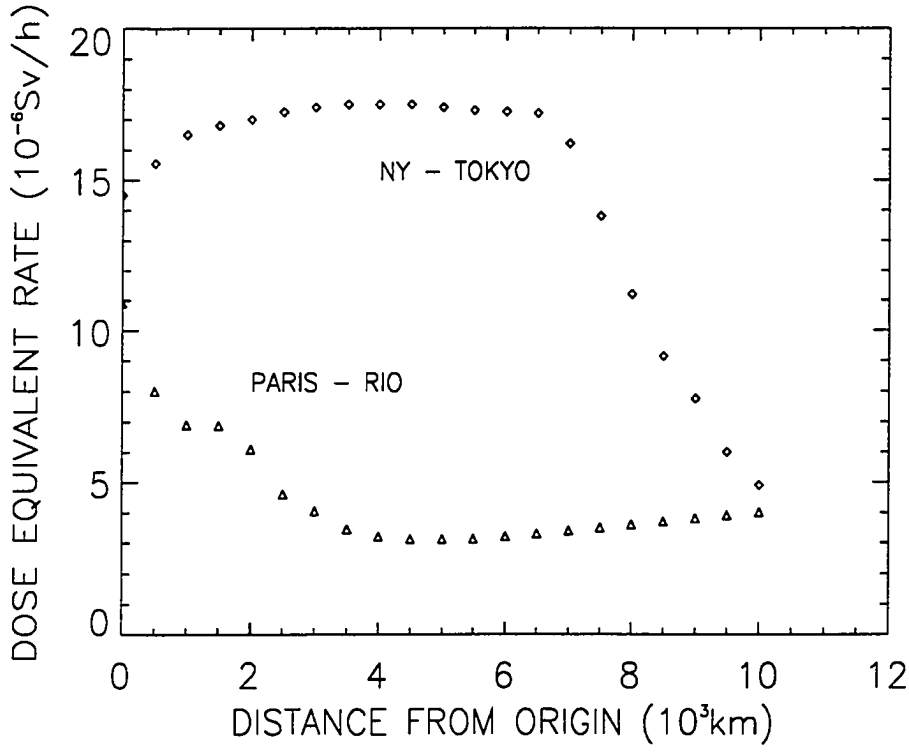

Figure 1.1 Dose-equivalent rate profiles along the aircraft flight trajectories at 17 km from the earth's surface. The dose rate for N.Y. - Tokyo is in excess of 15 mSv per 1000 hours since the route is at high altitudes.

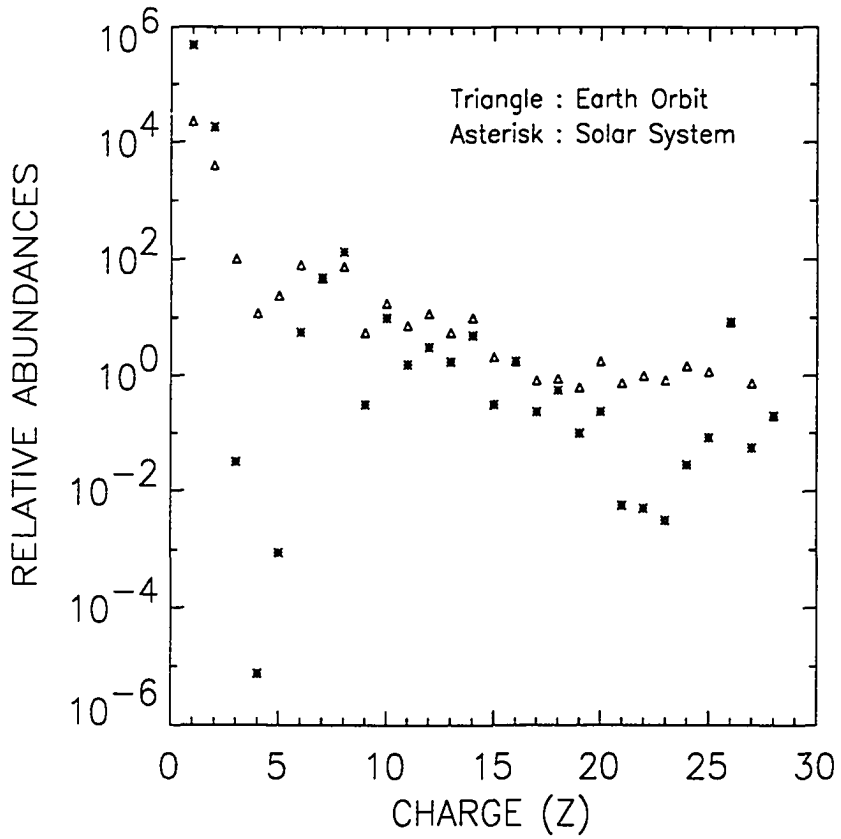

Figure 1.2 The relative abundances of heavy ions in cosmic rays observed on the earth (triangles) and for the general solar system (asterisks).

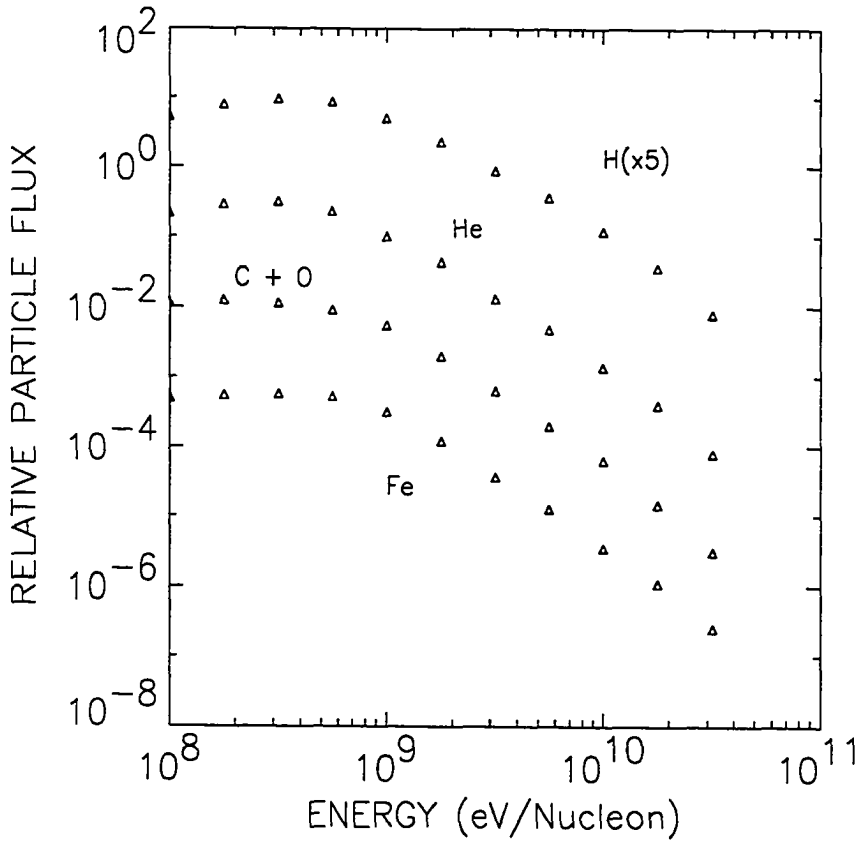

Figure 1.3 The energy spectra of the most abundant cosmic-ray particles. The hydrogen spectrum shows significantly high-level of intensity, and the general shapes of spectra are similar.

CHAPTER 2
GREEN'S FUNCTION SOLUTION OF TRANSPORT EQUATION

The central idea of the Boltzmann transport equation is to determine particle distributions in a given medium by considering a particle balance. The assumptions to describe physical systems (projectile and target particles) and collision processes are: (1) A point particle at $\vec{x}$ is characterized by an energy E and an angular direction $\hat{\Omega}$. (2) The particles are assumed to travel in straight lines between collisions. (3) The collisions are assumed to be instantaneous, and the position $\vec{x}$ remains unaltered during the collisions. The energy and angular direction are denoted by E' and $\hat{\Omega}'$ respectively before the collision, and E and $\hat{\Omega}$ after the collision.

In the Green's function method, the Green's function is introduced as a solution for a monoenergetic boundary distribution to solve a heavy-ion transport equation.[31] The energy-dependence of nuclear cross sections is imparted into the survival probability. In the present work, we solve a heavy-ion transport equation. From the energy-dependent Green's function (i.e. when the nuclear cross section depends on the energy), the energy-independent Green's function (i.e. when the nuclear cross section is assumed to be independent on the energy) is derived. The collision terms of the energy-dependent Green's function are approximated.

2.1 BOLTZMANN TRANSPORT EQUATION FOR HZE IONS

When a particle in a volume element $\mathrm{d}\vec{x}$ travels along a direction $\hat{\Omega}$ within a cone $\mathrm{d}\hat{\Omega}$ with an energy between E and $E + \mathrm{d}E$, the total number of particles at time t is given by a quantity $N(\vec{x}, E, \hat{\Omega}, t)\,\mathrm{d}\vec{x}\,\mathrm{d}E\,\mathrm{d}\hat{\Omega}$ where $N(\vec{x}, E, \hat{\Omega}, t)$ is the number density

of particles in a volume element at time t. The angular flux $\psi(\vec{x}, E, \hat{\Omega}, t)$ is defined by $\psi(\vec{x}, E, \hat{\Omega}, t) \equiv vN(\vec{x}, E, \hat{\Omega}, t)$ where v is the speed of the particle. The total number of collisions per unit time in $\mathrm{d}\vec{x}$ is $\Sigma(\vec{x}, E)\,\psi(\vec{x}, E, \hat{\Omega}, t)\,\mathrm{d}A\,\mathrm{d}l\,\mathrm{d}E\,\mathrm{d}\hat{\Omega}$ where $\Sigma(\vec{x}, E)$ is the collision probability per unit distance for the particle at $\vec{x}$ with energy E. The quantities $\mathrm{d}A$ and $\mathrm{d}l$ are the area element and length element respectively, where $\mathrm{d}|\vec{x}|=\mathrm{d}A\,\mathrm{d}l$. The change of particle number due to collisions in $\mathrm{d}x\,\mathrm{d}E\,\mathrm{d}\hat{\Omega}$ during $\mathrm{d}t$ is given by $\Sigma(\vec{x}, E)\; v\, N(\vec{x}, E, \hat{\Omega}, t)\,\mathrm{d}A\,\mathrm{d}l\,\mathrm{d}E\,\mathrm{d}\hat{\Omega}\,\mathrm{d}t$.

Since the change of the particle number in $\mathrm{d}\vec{x}\,\mathrm{d}E\,\mathrm{d}\hat{\Omega}$ during the time $\mathrm{d}t$ is $\{N(\vec{x}, E, \hat{\Omega}, t + \mathrm{d}t) - N(\vec{x}, E, \hat{\Omega}, t)\}\,\mathrm{d}A\,\mathrm{d}l\,\mathrm{d}E\,\mathrm{d}\hat{\Omega}$ and the total number of particles scattered from $\mathrm{d}\vec{x}\,\mathrm{d}E\,\mathrm{d}\hat{\Omega}$ during the time $\mathrm{d}t$ through $\vec{x}+\mathrm{d}l\,\hat{\Omega}$ is $\{N(\vec{x}+\mathrm{d}l\,\hat{\Omega}, E, \hat{\Omega}, t) - N(\vec{x}, E, \hat{\Omega}, t)\}\,\mathrm{d}A\,\mathrm{d}l\,\mathrm{d}E\,\mathrm{d}\hat{\Omega}$, the particle balance equation is written as

$$
\begin{aligned}
&\{N(\vec{x}, E, \hat{\Omega}, t + \mathrm{d}t) - N(\vec{x}, E, \hat{\Omega}, t)\}\,\mathrm{d}A\,\mathrm{d}l\,\mathrm{d}E\,\mathrm{d}\hat{\Omega} \\
&\quad = -\Big\{N(\vec{x} + \mathrm{d}l\,\hat{\Omega}, E, \hat{\Omega}, t) - N(\vec{x}, E, \hat{\Omega}, t)\Big\}\, v\,\mathrm{d}t\,\mathrm{d}A\,\mathrm{d}E\,\mathrm{d}\hat{\Omega} \\
&\qquad - \Sigma(\vec{x}, E)\, N(\vec{x}, E, \hat{\Omega}, t)\, v\,\mathrm{d}t\,\mathrm{d}A\,\mathrm{d}l\,\mathrm{d}E\,\mathrm{d}\hat{\Omega} \\
&\qquad + q(\vec{x}, E, \hat{\Omega}, t)\,\mathrm{d}A\,\mathrm{d}l\,\mathrm{d}E\,\mathrm{d}\hat{\Omega}\,\mathrm{d}t
\end{aligned}
\tag{2.1}
$$

where $\mathrm{d}l = v\,\mathrm{d}t$, and $q(\vec{x}, E, \hat{\Omega}, t)$ denotes the number of particles produced per unit volume due to collisions and internal sources along the angular direction $\mathrm{d}\hat{\Omega}$ about $\hat{\Omega}$ with energy E during the time interval $\mathrm{d}t$. The second term on the righthand side of Eq. (2.1) represents the loss of particles due to collisions. The Eq. (2.1) can be written in terms of the angular flux $\psi(\vec{x}, E, \hat{\Omega}, t)$ as

$$
\begin{aligned}
&\frac{1}{v}\frac{\partial}{\partial t}\psi(\vec{x}, E, \hat{\Omega}, t) + \frac{\partial}{\partial l}\psi(\vec{x}, E, \hat{\Omega}, t) + \Sigma(\vec{x}, E)\,\psi(\vec{x}, E, \hat{\Omega}, t) \\
&\qquad = \int \mathrm{d}E'\,\mathrm{d}\hat{\Omega}'\,\Sigma_s(\vec{x}, E' \to E, \hat{\Omega}' \to \hat{\Omega})\,\psi(\vec{x}, E', \hat{\Omega}', t)
\end{aligned}
\tag{2.2}
$$

since $q(\vec{x}, E, \hat{\Omega}, t)$ is expressed as $\int \mathrm{d}E'\,\mathrm{d}\hat{\Omega}'\,\Sigma_s(\vec{x}, E' \to E, \hat{\Omega}' \to \hat{\Omega})\,\psi(\vec{x}, E', \hat{\Omega}', t)$

where $\Sigma_s(\vec{x}, E' \to E, \hat{\Omega}' \to \hat{\Omega})$ is the probability per unit length when the projectile with energy E' and direction $\hat{\Omega}'$ is scattered into a direction $\hat{\Omega}$ with energy E.

The solution $\psi(\vec{x}, E, \hat{\Omega}, t)$ of Eq. (2.2) can be written as $\phi(\vec{x}, E, \hat{\Omega})\, e^{\lambda t}$ where λ is the decay constant of the incoming particle and $\phi(\vec{x}, E, \hat{\Omega})$ is the time-independent particle angular flux at $\vec{x}$ with energy E in the direction $\hat{\Omega}$ at time t. Thus, Eq. (2.2) becomes

$$\left\{\frac{\lambda}{v} + \hat{\Omega}\cdot\nabla + \Sigma(\vec{x}, E)\right\}\phi(\vec{x}, E, \hat{\Omega}) = \int \mathrm{d}E'\, \mathrm{d}\hat{\Omega}'\, \Sigma_s(\vec{x}, E' \to E, \hat{\Omega}' \to \hat{\Omega})\, \phi(\vec{x}, E', \hat{\Omega}') \tag{2.3}$$

where $\frac{d}{dl}$ is replaced by $\hat{\Omega}\cdot\nabla$ along the direction of particle motion.

Since we can assume that the volume and the density of the medium are not changed severely during the reaction processes, and a heavy-ion has a relatively long life-time compared to the collision-time, the time-dependent term can be ignored. Then the transport equation for the j-th particle which is produced by the collision with the k-th particle is given by

$$\left\{\hat{\Omega}\cdot\nabla + \tilde{\sigma}_j(E)\right\}\phi_j(\vec{x}, E, \hat{\Omega}) = \sum_{k>j}\int \mathrm{d}E'\, \mathrm{d}\hat{\Omega}'\, \tilde{\sigma}_k(E', E, \hat{\Omega}', \hat{\Omega})\, \phi_{jk}(\vec{x}, E', \hat{\Omega}') \tag{2.4}$$

where $\tilde{\sigma}_j(E)$ is the total scattering cross section of the ions of type j, and $\tilde{\sigma}_{jk}(E', E, \hat{\Omega}', \hat{\Omega})$ is the total production cross section of the ions of type j with energy E and direction $\hat{\Omega}$ by the collision of the ions of type k with energy E' and direction $\hat{\Omega}'$. We assume that the collision is instantaneous at $\vec{x}$.

The total macroscopic cross section $\tilde{\sigma}_j(E)$ and the production cross section $\tilde{\sigma}_{jk}(E', E, \hat{\Omega}', \hat{\Omega})$ can be written as

$$\tilde{\sigma}_j(E) \simeq \sigma_j^{nu}(E) + \sigma_j^{at}(E) \tag{2.5}$$

$$\tilde{\sigma}_{jk}(E', E, \hat{\Omega}', \hat{\Omega}) \simeq \sigma_{jk}^{nu}(E', E, \hat{\Omega}', \hat{\Omega}) + \sigma_{jk}^{at}(E', E, \hat{\Omega}', \hat{\Omega}) \tag{2.6}$$

where the superscripts "nu" and "at" refer to the nuclear process and the atomic process respectively. The atomic cross section $\sigma_{jk}^{at}(E', E, \hat{\Omega}', \hat{\Omega})$ can be rewritten as

$$\sum_k \sigma_{jk}^{at}(E', E, \hat{\Omega}', \hat{\Omega}) = \sum_n \sigma_{jn}^{at}(E)\, \delta(E + \epsilon_n - E')\, \delta(\hat{\Omega}' \cdot \hat{\Omega} - 1)\, \delta_{jn} \tag{2.7}$$

where n represents the electronic excitation level and ϵ_n is the corresponding excitation energy. Since the excitation energy is quite small compared to the particle energy E', we use the Taylor series. The definition of stopping power $S_j(E)$ can be written as

$$S_j(E) = \sum_n \epsilon_n\, \sigma_{jn}^{at}(E) \tag{2.8}$$

and the atomic contribution of the righthand side of Eq. (2.4) can be expressed as

$$\begin{aligned} &\sum_k \int \mathrm{d}E'\, \mathrm{d}\Omega'\, \sigma_{jk}^{at}(E', E, \hat{\Omega}', \hat{\Omega})\, \phi_k(\vec{x}, E', \hat{\Omega}') \\ &\qquad \approx \sum_n \left(1 + \epsilon_n \frac{\partial}{\partial E} + \cdots\right) \sigma_{jn}^{at}(E)\, \phi_j(\vec{x}, E, \hat{\Omega}) \\ &\qquad = \sigma_j^{at}(E)\, \phi_j(\vec{x}, E, \hat{\Omega}) + \frac{\partial}{\partial E}\left[S_j(E)\, \phi_j(\vec{x}, E, \hat{\Omega})\right] + \cdots \end{aligned} \tag{2.9}$$

Then the heavy-ion transport equation is obtained by dropping the notation "nu" in the nuclear cross sections as

$$\begin{aligned} &\left\{\vec{\Omega} \cdot \nabla - \frac{\partial}{\partial E} \widetilde{S}_j(E) + \sigma_j(E)\right\} \phi_j(\vec{x}, E, \hat{\Omega}) \\ &\qquad = \sum_{k>j} \int \mathrm{d}E'\, \mathrm{d}\hat{\Omega}'\, \sigma_{jk}(E', E, \hat{\Omega}', \hat{\Omega})\, \phi_k(\vec{x}, E', \hat{\Omega}') \end{aligned} \tag{2.10}$$

where the stopping power of a heavy-ion is defined by

$$\widetilde{S}_j(E) = \frac{1}{A_j} \frac{\partial}{\partial E} S_j(E) \tag{2.11}$$

and $\phi_j(\vec{x}, E, \hat{\Omega})$ is the particle flux of the ions of type j, $\sigma_j(E)$ is the macroscopic nuclear cross section, $\widetilde{S_j}(E)$ is the stopping power (the energy loss per unit length), and $\sigma_{jk}(E', E, \hat{\Omega}', \hat{\Omega})$ is the nuclear fragmentation cross section where E' and $\hat{\Omega}'$ are the energy and the direction of an incoming ion, and E and $\hat{\Omega}$ refer to those of an outgoing particle.

Let us assume that $\phi_m(\vec{x}_\Gamma, E_0, \hat{\Omega}_0)$ represents the particle flux at a boundary $\vec{x}_\Gamma$, where $\vec{x}_\Gamma$ is the position vector of the incident ion of type m at the boundary, and $\vec{\Omega}_0$ is the angular direction vector of the incident ion. The direction $\hat{\Omega}$ of a scattered ion satisfies the condition $\hat{\Omega} \cdot \hat{n}(\vec{x}_\Gamma) < 0$, where $\hat{n}(\vec{x}_\Gamma)$ is the outwardly directed normal vector to the boundary surface at the point $\vec{x}_\Gamma$. For a monoenergetic beam, the flux at the boundary is assumed as a delta function. Thus, $\phi_m(\vec{x}_\Gamma, E_0, \hat{\Omega}_0) = \delta(\vec{x} - \vec{x}_\Gamma)\,\delta(E - E_0)\,\delta(\hat{\Omega} - \hat{\Omega}_0)$. For a realistic laboratory beam distribution at the boundary, the initial beam can be assumed to be a Gaussian distribution function with a given energy spread Δ. Therefore, $\phi_m(\vec{x}_\Gamma, \vec{\Omega}_0, E_0) = \delta(\vec{x} - \vec{x}_\Gamma)\,\delta(\vec{\Omega} - \vec{\Omega}_0)\,\frac{1}{\sqrt{2\pi}\Delta}\,\exp\left[-\frac{(E_0 - E_0')^2}{2\Delta^2}\right]$, where E_0' is the mean energy of the incident ion.

If the incident energy is sufficiently high, the energy shift caused by atomic collisions becomes negligible. Therefore, the heavy-ion transport equation can be approximated without the ionization-loss term as

$$\left\{\vec{\Omega} \cdot \nabla + \sigma_j(E)\right\} \phi_j(\vec{x}, E, \hat{\Omega}) = \sum_{k>j} \int \mathrm{d}E'\, \mathrm{d}\hat{\Omega}'\, \sigma_{jk}(E', E, \hat{\Omega}', \hat{\Omega})\, \phi_k(\vec{x}, E', \Omega') \tag{2.12}$$

which is valid for a high-energy approximation. This equation will be used later in Section 2.4, and the solution will be used as a higher-order approximation.

Going back to Eq. (2.10), we know that it is an integro-differential equation, and the analytical solution is very hard to obtain. Using the straight-ahead approximation[29] and the velocity conserving fragmentation assumption,[27] the one-

dimensional form of Eq. (2.10) is written as

$$\left\{\frac{\partial}{\partial x}-\frac{\partial}{\partial E}\widetilde{S_j}(E)+\sigma_j(E)\right\}\phi_j(x,E)=\sum_{k>j}\sigma_{jk}(E)\,\phi_k(x,E) \tag{2.13}$$

where the fragmentation cross section $\sigma_{jk}(E)$ can be expressed in terms of the energy-dependent multiplicity. The boundary conditions at x=0 are given by $\phi_m(0,E)=\delta(E-E_0)$ for a monoenergetic distribution, and $\phi_m(0,E)\equiv f_m(E_0)=\frac{1}{\sqrt{2\pi}\Delta}\exp\left[-\frac{(E_0-E_0')^2}{2\Delta^2}\right]$ for a Gaussian distribution, where Δ is the energy spread.

2.2 FIRST-ORDER ENERGY-DEPENDENT GREEN'S FUNCTION

Let us assume with Bethe[1,32] the following: $\widetilde{S_j}(E)=\frac{\nu_j}{\nu_p}\widetilde{S_p}(E)$ where ν_j is $\nu_j\equiv\frac{Z_j^2}{A_j}$, and "$p$" refers to the proton. This assumption is valid for all energies above 100 keV/nucleon provided that the ion remains fully stripped[1]. The range $R_j(E)$ of an ion is defined by

$$R_j(E)\equiv\int_0^E\frac{\mathrm{d}E'}{\widetilde{S_j}(E')} \tag{2.14}$$

and the inverse function of $R_j(E)$ is written as $E=R_j^{-1}[R_j(E)]$. We will use the notation r_j instead of $R_j(E)$ in (x,r_j)-space hereafter.

Now, multiply both sides of Eq. (2.13) by $\widetilde{S_j}(E)$. Eq. (2.13) can be transformed to (x,r_j)-space from (x,E)-space as

$$\left\{\frac{\partial}{\partial x}-\frac{\partial}{\partial r_j}+\sigma_j(r_j)\right\}\overline{\phi}_j(x,r_j)=\sum_{k>j}\frac{\nu_j}{\nu_k}\sigma_{jk}(r_j)\,\overline{\phi}_k(x,r_j) \tag{2.15}$$

where ν_k is defined by $\nu_k\equiv\frac{Z_k^2}{A_k}$ and $\overline{\phi}_{j(k)}(x,r_j)=\widetilde{S}_{j(k)}(E)\phi_{j(k)}(x,E)$. It is convenient to solve Eq. (2.15) if we introduce the characteristic coordinates[28]

$$\eta_j=x-r_j \tag{2.16}$$

$$\xi_j=x+r_j \tag{2.17}$$

and a new field function

$$\chi_j(\eta_j,\xi_j) = \widetilde{S_j}(E)\phi_j(x,E) \tag{2.18}$$

where η_j varies along a path from $-\xi_j$ to ξ_j, and ξ_j is constant along the particle trajectory. In a similar fashion, the field function $\chi_k(\eta_k,\xi_k)$ is transformed into (η_k,ξ_k)-space for the k-th particle using the characteristic coordinate transformation. As a result, Eq. (2.15) becomes

$$\left\{2\frac{\partial}{\partial\eta_j} + \sigma_j(\eta_j,\xi_j)\right\}\chi_j(\eta_j,\xi_j) = \sum_{k>j}\sigma_{jk}(\eta_j,\xi_j)\,\chi_k(\eta_k,\xi_k) \tag{2.19}$$

where (η_j,ξ_j) and (η_k,ξ_k) are related by

$$\eta_j + \xi_j = \eta_k + \xi_k \tag{2.20}$$

$$\eta_j - \xi_j = \frac{\nu_k}{\nu_j}(\eta_k - \xi_k) \tag{2.21}$$

Eq. (2.19) is an ordinary differential equation and can be solved using an integrating factor, $\exp\left\{\frac{1}{2}\int_{-\xi_j}^{\eta_j}\sigma_j\left(\frac{\xi_j-\eta_j''}{2}\right)\mathrm{d}\eta_j''\right\}$. The quantities η_k and ξ_k are given by

$$\eta_k = \frac{\nu_k+\nu_j}{2\nu_k}\eta_j' + \frac{\nu_k-\nu_j}{2\nu_k}\xi_j \tag{2.22}$$

$$\xi_k = \frac{\nu_k-\nu_j}{2\nu_k}\eta_j' + \frac{\nu_k+\nu_j}{2\nu_k}\xi_j \tag{2.23}$$

and the solution of Eq. (2.19) is obtained as

$$\begin{aligned}\chi_j(\eta_j,\xi_j) = {} & \exp\left\{-\frac{1}{2}\int_{-\xi_j}^{\eta_j}\sigma_j\left(\frac{\xi_j-\eta_j''}{2}\right)\mathrm{d}\eta_j''\right\}\chi_j(-\xi_j,\xi_j) \\ & + \frac{1}{2}\sum_{k>j}\frac{\nu_j}{\nu_k}\int_{-\xi_j}^{\eta_j}\sigma_{jk}\left(\frac{\xi_j-\eta_j'}{2}\right)\chi_k(\eta_k,\xi_k) \\ & \times\exp\left\{-\frac{1}{2}\int_{\eta_j'}^{\eta_j}\sigma_j\left(\frac{\xi_j-\eta_j''}{2}\right)\mathrm{d}\eta_j''\right\}\mathrm{d}\eta_j'\end{aligned} \tag{2.24}$$

For the Green's function solution, the boundary condition $\chi_j(-\xi_j, \xi_j)$ is expressed in terms of delta functions as

$$\chi_j(-\xi_j, \xi_j) = \delta_{jm}\,\delta(\xi_j - r_m) \tag{2.25}$$

where $r_m = R_j(E_0)\,\delta_{jm}$, and E_0 is the incident energy of an incoming heavy-ion.

Using the notation, $\exp\left\{\alpha_j\binom{b}{a}\right\} \equiv \exp\left\{-\frac{1}{2}\int_a^b \sigma_j\left(\frac{\xi_j-\eta_j''}{2}\right)\mathrm{d}\eta_j''\right\}$, the solution of Eq. (2.19) can be obtained in a series form:

$$\chi_j(\eta_j, \xi_j) \approx \sum_{i=0}^{\infty} \chi_j^{(i)}(\eta_j, \xi_j) \tag{2.26}$$

where $\chi_j^{(i)}(\eta_j, \xi_j)$ is the i-th order perturbation term of the total particle flux $\chi_j(\eta_j, \xi_j)$. The perturbation terms are then given by

$$\chi_j^{(0)}(\eta_j, \xi_j) = \exp\left\{\alpha_j\binom{\eta_j}{\xi_j}\right\}\delta_{jm}\,\delta(\xi_j - r_m) \tag{2.27}$$

$$\begin{aligned}\chi_j^{(1)}(\eta_j, \xi_j) = \frac{1}{2}\sum_k \frac{\nu_j}{\nu_k}\int_{-\xi_j}^{\eta_j}\sigma_{jk}\left(\frac{\xi_j-\eta_j'}{2}\right)\exp\left\{\alpha_j\binom{\eta_j}{\eta_j'}\right\}\mathrm{d}\eta_j' \\ \times \exp\left\{\alpha_k\binom{\eta_k}{-\xi_k}\right\}\delta_{km}\,\delta(\xi_k - r_m)\end{aligned} \tag{2.28}$$

and

$$\begin{aligned}\chi_j^{(2)}(\eta_j, \xi_j) = \frac{1}{2}\sum_k \frac{\nu_j}{\nu_k}\int_{-\xi_j}^{\eta_j}\sigma_{jk}\left(\frac{\xi_j-\eta_j'}{2}\right)\exp\left\{\alpha_j\binom{\eta_j}{\eta_j'}\right\}\mathrm{d}\eta_j' \\ \times \frac{1}{2}\sum_l \frac{\nu_k}{\nu_l}\int_{-\xi_k}^{\eta_k}\sigma_{kl}\left(\frac{\xi_k-\eta_k'}{2}\right)\exp\left\{\alpha_k\binom{\eta_k}{\eta_k'}\right\}\mathrm{d}\eta_k' \\ \times \exp\left\{\alpha_l\binom{\eta_l}{-\xi_l}\right\}\delta_{lm}\,\delta(\xi_l - r_m)\end{aligned} \tag{2.29}$$

where the particle indices obey the condition $j < k < l$. The n-th order perturbation

term is generalized as

$$\chi^{(n)}(\eta_j,\xi_j) = \frac{1}{2}\sum_{j_1}\frac{\nu_j}{\nu_{j_1}}\int_{-\xi_j}^{\eta_j}\sigma_{j\,j_1}\Big(\frac{\xi_j-\eta'_j}{2}\Big)\exp\Big\{\alpha_j\binom{\eta_j}{\eta'_j}\Big\}\,\mathrm{d}\eta'_j$$

$$\times\frac{1}{2}\sum_{j_2}\frac{\nu_{j_1}}{\nu_{j_2}}\int_{-\xi_{j_1}}^{\eta_{j_1}}\sigma_{j_1 j_2}\Big(\frac{\xi_{j_1}-\eta'_{j_1}}{2}\Big)\exp\Big\{\alpha_{j_1}\binom{\eta_{j_1}}{\eta'_{j_1}}\Big\}\,\mathrm{d}\eta'_{j_1}$$

$$\vdots$$

$$\times\frac{1}{2}\sum_{j_n}\frac{\nu_{j_{n-1}}}{\nu_{j_n}}\int_{-\xi_{j_{n-1}}}^{\eta_{j_{n-1}}}\sigma_{j_{n-1}\,j_n}\Big(\frac{\xi_{j_{n-1}}-\eta'_{j_{n-1}}}{2}\Big)\exp\Big\{\alpha_{j_{n-1}}\binom{\eta_{j_{n-1}}}{\eta'_{j_{n-1}}}\Big\}\,\mathrm{d}\eta'_{j_{n-1}}$$

$$\times\Big\{\alpha_{j_n}\binom{\eta_{j_n}}{-\xi_{j_n}}\Big\}\,\delta_{j_n m}\,\delta(\xi_{j_n}-r_m) \tag{2.30}$$

where the indices obey the condition $j < j_1 < j_2 < \cdots < j_n < m$ and the boundary condition is given by $\chi_{j_n}(-\xi_{j_n},\xi_{j_n}) = \delta(j_n - r_m)\,\delta_{j_n m}$.

For the monoenergetic boundary condition, the solution of Eq. (2.19) is given by the Green's function and the boundary condition is given by $G_{jm}(0,E,E_0) = \delta_{jm}\,\delta(E-E_0)$. The Green's function solution of Eq. (2.19) is expressed as

$$G_{jm}(x,E,E_0) \approx \sum_{i=0}^{\infty} G_{jm}^{(i)}(x,E,E_0) \tag{2.31}$$

In (x,E)-space, the quantity $\exp\{\alpha_j\binom{b}{a}\}$ is defined in terms of the survival probability $P_j(E)$ such that $\exp\Big\{\alpha_j\binom{b}{a}\Big\} = P_j(E_a)/P_j(E_b)$, where $P_j(E)$ is defined by[1,26]

$$P_j(E) \equiv \exp\Big[-\int_0^E \sigma_j(E')\frac{1}{\widetilde{S}_j(E')}\,\mathrm{d}E'\Big] \tag{2.32}$$

Then, the zero-th order Green's function solution which represents the attenuation of incoming particles becomes

$$G_{jm}^{(0)}(x,E,E_0) = \frac{\widetilde{S}_j(E_0)}{\widetilde{S}_j(E)}\,\frac{P_j(E_0)}{P_j(E)}\,\delta_{jm}\,\delta\Big[E_0 - R_j(E) - x\Big] \tag{2.33}$$

where E is the energy of the outgoing particle of type j

$$E = R_j^{-1}\left[r_m - x\right]\delta_{jm} \tag{2.34}$$

The first-collision term or the first-order perturbation term is given by

$$G_{jm}^{(1)}(x, E, E_0) = \frac{1}{\widetilde{S}_j(E)} \sum_{k>j} \frac{\nu_j}{|\nu_k - \nu_j|} \sigma_{jk}(E') \frac{P_k(E_0)}{P_k(E')} \frac{P_j(E')}{P_j(E)} \delta_{km} \tag{2.35}$$

where

$$E' = R_k^{-1}\left[\frac{\nu_j}{\nu_k - \nu_j}(x + r_j - r_m)\right]\delta_{km} \tag{2.36}$$

The energy domain is obtained from the relationship $-\xi_j < \eta_j' < \eta_j$. We found the energy domain using an inverse transformation. The energy domain is given by

$$R_j^{-1}\left[\frac{\nu_m}{\nu_j}(r_m - x)\right] < E < R_j^{-1}\left[\frac{\nu_m}{\nu_j} r_m - x\right] \tag{2.37}$$

otherwise $G_{jm}^{(1)}(x, E, E_0)$ becomes zero. For $\nu_j \leq \nu_m$, the inverse relation of the energy domain Eq. (2.37) provides the limits of the incident beam energy E_0 as

$$R_m^{-1}\left[\frac{\nu_j}{\nu_m}(r_j + x)\right] < E_0 < R_m^{-1}\left[\frac{\nu_j}{\nu_m} r_j + x\right] \tag{2.38}$$

For $\nu_j > \nu_m$, the inequalities of Eq. (2.37) and Eq. (2.38) are reversal, and it can happen in the case of neutron removal.

2.3 FIRST-ORDER ENERGY-INDEPENDENT GREEN'S FUNCTION

The energy-independent Green's function solution of Eq. (2.19) can be derived from the energy-dependent solution Eq. (2.24) by replacing the integrating factor $\alpha_j\binom{b}{a}$ by $\mu_j\binom{b}{a}$, defined as $\mu_j\binom{b}{a} \equiv -\frac{1}{2}\sigma_j(b-a)$. Then the energy-independent solution of Eq. (2.19) can be written in terms of $\mu_j\binom{b}{a}$ and σ_j (energy-independent nuclear cross section) as

$$\chi_j^{(0)}(\eta_j, \xi_j) = \exp\left\{\mu_j\binom{\eta_j}{\xi_j}\right\}\delta_{jm}\,\delta(\xi_j - r_m) \tag{2.39}$$

$$\chi_j^{(1)}(\eta_j,\xi_j) = \frac{1}{2}\sum_k \frac{\nu_j}{\nu_k}\sigma_{jk}\int_{-\xi_j}^{\eta_j} \exp\left\{\mu_j\begin{pmatrix}\eta_j\\ \eta_j'\end{pmatrix}\right\} \mathrm{d}\eta_j'$$

$$\times \exp\left\{\mu_k\begin{pmatrix}\eta_k\\ -\xi_k\end{pmatrix}\right\} \delta_{km}\,\delta(\xi_k - r_m) \tag{2.40}$$

and

$$\chi_j^{(2)}(\eta_j,\xi_j) = \frac{1}{2}\sum_k \frac{\nu_j}{\nu_k}\sigma_{jk}\int_{-\xi_j}^{\eta_j} \exp\left\{\mu_j\begin{pmatrix}\eta_j\\ \eta_j'\end{pmatrix}\right\} \mathrm{d}\eta_j' \frac{1}{2}\sum_l \frac{\nu_k}{\nu_l}\sigma_{kl}$$

$$\times \int_{-\xi_k}^{\eta_k} \exp\left\{\mu_k\begin{pmatrix}\eta_k\\ \eta_k'\end{pmatrix}\right\} \mathrm{d}\eta_k' \exp\left\{\mu_l\begin{pmatrix}\eta_l\\ -\xi_l\end{pmatrix}\right\} \delta_{lm}\,\delta(\xi_l - r_m) \tag{2.41}$$

Furthermore, $\chi_j^{(0)}(\eta_j,\xi_j)$ and $\chi_j^{(1)}(\eta_j,\xi_j)$ can be expressed as

$$\chi_j^{(0)}(\eta_j,\xi_j) = \exp\left\{-\frac{1}{2}\sigma_j(\eta_j+\xi_j)\right\}\delta_{jm}\,\delta(\xi_j - r_m) \tag{2.43}$$

$$\chi_j^{(1)}(\eta_j,\xi_j) = \frac{\nu_j}{\nu_k-\nu_j}\exp\left\{-\frac{1}{2}\sigma_j(\eta_j-\eta_j') - \frac{1}{2}\sigma_k(\xi_j+\eta_j')\right\}\delta_{km} \tag{2.42}$$

where

$$\eta_j' = \left\{\frac{2\nu_k}{\nu_k-\nu_j}r_m - \frac{\nu_k+\nu_j}{\nu_k-\nu_j}\xi_j\right\}\delta_{km} \tag{2.43}$$

The n-th order perturbation term can be generalized as

$$\chi^{(n)}(\eta_j,\xi_j) = \frac{1}{2}\sum_{j_1}\frac{\nu_j}{\nu_{j_1}}\sigma_{jj_1}\int_{-\xi_j}^{\eta_j}\exp\left\{\mu_j\begin{pmatrix}\eta_j\\ \eta_j'\end{pmatrix}\right\}\mathrm{d}\eta_j'$$

$$\times\frac{1}{2}\sum_{j_2}\frac{\nu_{j_1}}{\nu_{j_2}}\sigma_{j_1j_2}\int_{-\xi_{j_1}}^{\eta_{j_1}}\exp\left\{\mu_{j_1}\begin{pmatrix}\eta_{j_1}\\ \eta_{j_1}'\end{pmatrix}\right\}\mathrm{d}\eta_{j_1}'$$

$$\vdots$$

$$\times\frac{1}{2}\sum_{j_n}\frac{\nu_{j_{n-1}}}{\nu_{j_n}}\sigma_{j_{n-1}j_n}\int_{-\xi_{j_{n-1}}}^{\eta_{j_{n-1}}}\exp\left\{\mu_{j_{n-1}}\begin{pmatrix}\eta_{j_{n-1}}\\ \eta_{j_{n-1}}'\end{pmatrix}\right\}\mathrm{d}\eta_{j_{n-1}}'$$

$$\times\left\{\mu_{j_n}\begin{pmatrix}\eta_{j_n}\\ -\xi_{j_n}\end{pmatrix}\right\}\delta_{j_nm}\,\delta(\xi_{j_n}-r_m) \tag{2.44}$$

where the indices obey the condition $j < j_1 < j_2 < \cdots < j_n < m$, and the boundary condition is given by $\chi_{j_n}(-\xi_{j_n}, \xi_{j_n}) = \delta(j_n - r_m)\,\delta_{j_n m}$. The energy domains for the first collision are given in Eq. (2.37) and in Eq. (2.38).

Through an inverse transformation from (η_j, ξ_j)-space to (x, E)-space, the energy-independent Green's functions in (x, E)-space are obtained as

$$G_{jm}^{(0)}(x, E, E_0) = \exp\{-\sigma_j x\}\,\delta_{jm}\,\delta(x + r_j - r_m) \tag{2.45}$$

and

$$G_{jm}^{(1)}(x, E, E_0) = \frac{1}{\widetilde{S_j}(E)}\,\sigma_{jk}\,\frac{\nu_j}{|\nu_k - \nu_j|}\,\delta_{km} \times \exp\left\{-\frac{1}{2}\sigma_j(x - r_j - \eta') - \frac{1}{2}\sigma_k(x + r_j + \eta')\right\} \tag{2.46}$$

where E is given in Eq. (2.34), and η' is given by

$$\eta' = \left\{\frac{2\nu_k}{\nu_k - \nu_j} r_m - \frac{\nu_k + \nu_j}{\nu_k - \nu_j}(r_j + x)\right\}\,\delta_{km} \tag{2.47}$$

The energy domains are the same in the energy-independent formalism.

2.4 APPROXIMATE GREEN'S FUNCTION FOR COLLISION TERM

In the present work, collision terms are approximated. The numerical difficulty increases with the order of perturbation terms. Even for the first-collision term, the numerical integration to calculate particle flux and dose is a time consuming process, especially, for a heavy and high-energy ion. On the other hand, the contribution of higher-order terms to the total flux becomes smaller except for light fragments. In general, the attenuation term and the first-order collision term dominate the entire transport process of particle propagation. For a light ion with a low incident energy, low-energy fragments dominate the transport process. As a result, more accurate calculations for the higher-order perturbation terms are required for light nuclei.

Since the first-order Green's function $G_{jm}^{(1)}(x, E, E_0)$ is a slowly varying linear function of incident energy E_0, we use the following approximation:

$$G_{jm}^{(1)}(x, E, E_0) \approx \overline{G}_{jm}^{(1)}(x, E) + B_{jm}^{(1)}(x, E)\,(E_0' - \overline{E}_0) \tag{2.48}$$

where $\overline{G}_{jm}^{(1)}$ is the averaged Green's function defined by

$$\overline{G}_{jm}^{(1)}(x, E) \equiv \frac{1}{\Delta E_0} \int_{E_{0,\min}}^{E_{0,\max}} G_{jm}^{(1)}(x, E, E_0)\,\mathrm{d}E_0 \tag{2.49}$$

and $\Delta E_0 = E_{0,max} - E_{0,min}$. In Eq. (2.49), $E_{0,min}$ and $E_{0,max}$ are the limits given in Eq. (2.38), $\overline{E}_0$ is the midpoint of the energy interval

$$\overline{E}_0 = \frac{1}{2}(E_{0,\max} + E_{0,\min}) \tag{2.50}$$

and E_0' is the average energy given by

$$E_0' = \frac{\int_{E_{0,\min}}^{E_{0,\max}} E_0\, f_m(E_0)\,\mathrm{d}E_0}{\int_{E_{0,\min}}^{E_{0,\max}} f_m(E_0)\,\mathrm{d}E_0} \tag{2.51}$$

where $f_m(E_0)$ is the particle distribution at its boundary. The parametric slope function $B_{jm}^{(1)}(x, E)$ is expressed in terms of the Green's function as

$$B_{jm}^{(1)}(x, E) = \frac{G_{jm}^{(1)}(x, E, E_{0,\max}) - G_{jm}^{(1)}(x, E, E_{0,\min})}{\Delta E_0} \tag{2.52}$$

In order to evaluate $\overline{G}_{jm}^{(1)}(x, E, E_0)$ in Eq. (2.49), the energy-dependent Green's function $G_{jm}^{(1)}(x, E, E_0)$ is written as

$$G_{jm}^{(1)}(x, E, E_0) = \frac{1}{\widetilde{S}_j(E)} \frac{\nu_j}{|\nu_m - \nu_j|} \exp\{K(E, E_0)\} \tag{2.53}$$

where

$$K(E, E_0) = \ln \sigma_{jm}(E') + O_m(E')\,R_m(E') + O_j(E)\,R_j(E)$$
$$- O_m(E_0)\,R_m(E_0) - O_j(E')\,R_j(E') \tag{2.54}$$

and E' is given in Eq. (2.36). The extinction coefficient $O_j(E)$ is defined by[1,26]

$$O_j(E) \equiv \frac{1}{R_j(E)} \int_0^E \frac{\sigma_j(E')}{\widetilde{S}_j(E')} \mathrm{d}E' \tag{2.55}$$

Since the function $\exp\left\{K(E, E_0)\right\}$ is a smooth function of the incoming particle energy E_0, we may approximate it as

$$\exp\left\{K(E, E_0)\right\} \approx \exp\left\{K(E, E_{0,\min})\right\} + \frac{\exp\left\{K(E, E_{0,\max})\right\} - \exp\left\{K(E, E_{0,\min})\right\}}{\Delta E_0} (E_0 - E_{0,\min}) \tag{2.56}$$

Then, $G_{jm}^{(1)}(x, E)$ becomes

$$G_{jm}^{(1)}(x, E) = \frac{1}{\widetilde{S}_j(E)} \frac{\nu_j}{|\nu_m - \nu_j|} \delta_{km} \left\{\zeta(E)\, E_0 + \kappa(E)\right\} \tag{2.57}$$

where

$$\zeta(E) = \left[\exp\left\{K(E, E_{0,\max})\right\} - \exp\left\{K(E, E_{0,\min})\right\}\right] \frac{1}{\Delta E_0} \tag{2.58}$$

$$\kappa(E) = \exp\left\{K(E, E_{0,\min})\right\} - \zeta(E) E_{0,\min} \tag{2.59}$$

The parametric functions $\zeta(E)$ and $\kappa(E)$ are introduced to simplify the approximate Green's function. In Eq. (2.58) and Eq. (2.59), we used $E'_{0,\max}$ and $E'_{0,\min}$ which are obtained from the limits in Eq. (2.38), and these are given by

$$E'_{0,\min} = R_m^{-1}\left[\frac{\nu_j}{\nu_m - \nu_j}\left(x + R_j(E) - R_m(E_{0,\min})\right)\right] \tag{2.60}$$

$$E'_{0,\max} = R_m^{-1}\left[\frac{\nu_j}{\nu_m - \nu_j}\left(x + R_j(E) - R_m(E_{0,\max})\right)\right] \tag{2.61}$$

The higher-order terms ($n \geq 2$) are approximated using the g-function.[1,22,23] The g-function is obtained by solving Eq. (2.12). It should be noted that the higher-order approximations are dependent on x for $n \geq 2$. In this work, the n-th order collision

term for a given incident ion is assumed to be[22,23]

$$G_{jm}^{(n)}(x,E,E_0) = \frac{1}{\widetilde{S_j}(E)} \frac{\nu_j}{x|\nu_m - \nu_j|} \sum_{j_1} \sum_{j_2} \cdots \sum_{j_n} \sigma_{jj_1} \cdots \sigma_{j_{n-1}j_n}$$

$$\times g(j,j_1,\cdots j_n,m)\,\delta_{j_n m} \qquad n \geq 2 \tag{2.62}$$

where

$$g(j,m) = e^{-\sigma_j x} \tag{2.63}$$

and

$$g(j,j_1,j_2,\cdots j_n,m) = \frac{1}{\sigma_{j_n} - \sigma_{j_{n-1}}}$$

$$\times \left\{ g(j,j_1,\cdots j_{n-2},j_{n-1},m) - g(j,j_1,\cdots j_{n-2},j_n,m) \right\} \tag{2.64}$$

The g-function is useful in obtaining approximate expressions for the higher-order collision terms of the heavy-ion transport equation. The nonperturbative solution of the Green's function uses the g-function. Wilson et al.[22,23] have derived several approximate perturbative and nonperturbative Green's functions using the g-function.

CHAPTER 3

NUCLEAR AND ATOMIC DATA BASES

The heavy-ion transport calculation requires adequately simple but still accurate nuclear and atomic data bases. In this work, a computer code NUCFRG[27,35–37] is used to generate a nuclear data base. For the atomic data base, Ziegler's empirical forms[38,39] are used. The calculated nuclear and atomic data base values (except the nuclear fragmentation cross sections) agreed within 5 to 10 percent compared with existing quantum mechanical values and experimental values.

3.1 NUCLEAR DATA BASE

In NUCFRG, heavy-ion absorption cross sections are obtained from the energy-dependent parameterization. This method was developed by Townsend et al.[35,40] as an alternative method to the quantum mechanical optical model formalism based on a microscopic optical potential approximation.[41] This is a simple parameterization based on a classical collision model using the Bradt and Peter formula,[42] and is given by

$$\sigma_{\text{abs}}(A_P, A_T, E) = \pi r_0^2 \beta(E) \left[A_P^{1/3} + A_T^{1/3} - \delta(A_P, A_T, E) \right]^2 \tag{3.1}$$

where

$$\beta(E) = 1 + 5\,E^{-1} \tag{3.2}$$

and

$$\delta(A_P, A_T, E) = 0.2 + A_P^{-1} + A_T^{-1} - 0.292 \exp\left[-\frac{E}{792} \right] \cos\left(0.229\,E^{0.453}\right) \tag{3.3}$$

with the uniform nuclear radius r_0=1.26 fm. The energy E is in units of MeV/nucleon, and fm stands for the fermi unit. For a large value of energy, $\beta(E)$ becomes 1 so that δ becomes energy-independent. Eq. (3.1) is accurate within 5 percent above 1 GeV per nucleon where the cross sections are nearly asymptotic, but it is less accurate at low energies.[27,35]

The nuclear fragmentation cross section is a major input data base. At present, however, there exists neither an extensive experimental cross section data base nor an adequate theory to generate the nuclear fragmentation cross sections.[37] The code NUCFRG is based on the geometrical abrasion-ablation model.[43] When high-energy heavy ions penetrate through a shielding material, the projectile nuclei collide with target nuclei in the medium. This interaction process is roughly divided into two major stages in the abrasion-ablation model. One is the abrasion step, in which some portions of the nuclear overlap volumes are sheared away. The next step is the ablation step in which the highly excited prefragments resulting from the abrasive process release energy by emitting nuclear fragments and electromagnetic radiation. This geometrical two-step nuclear fragmentation model is adequate to describe high-energy nucleus-nucleus collisions.

In the code NUCFRG, the total excitation energy is deposited by two processes; (1) the surface distortion excitation energy of the projectile prefragment following the abrasion of nucleons (this quantity is denoted as E_s), and (2) the excitation energy due to the transfer of the kinetic energy of relative motion across the intersecting boundary of the two ions during the ablation stage (this is denoted as E_x). Therefore, the total excitation energy E^* is given by

$$E^*(b) = E_s(b) + E_x(b) \tag{3.4}$$

where both $E_s(b)$ and $E_x(b)$ are given in terms of the impact parameter b through several parametric relations.[27,37]

The number of nucleons removed through the abrasion-ablation process is also defined in terms of the impact parameter b as

$$\Delta A(b) = \Delta_{\rm abr}(b) + \Delta_{\rm abl}(b) \tag{3.5}$$

where $\Delta_{\rm abr}(b)$ and $\Delta_{\rm abl}(b)$ are the numbers of abraded nucleons in the overlap region and removed nucleons from the overlap volume respectively. The number of nucleons removed through the abrasion stage is the amount of nuclear matter stripped away in the collision. This is taken as the volume of the overlap region times an average attenuation factor. The number of nucleons removed during the ablation stage is obtained by assuming that 10 MeV of the total excitation energy is required to remove one nucleon.

The quantity $\Delta_{\rm abr}(b)$ for the projectile ion mass A_P and the target ion mass A_T is expressed as[27,37]

$$\Delta_{\rm abr}(b) = F\,A_P\Big[1 - \frac{1}{2}\exp\Big(\frac{-C_P(b)}{\lambda}\Big) - \frac{1}{2}\exp\Big(\frac{-C_T(b)}{\lambda}\Big)\Big] \tag{3.6}$$

where $C_P(b)$ and $C_T(b)$ are the maximum chord lengths. The chord lengths represent the distances traveled by any target constituent nucleons through the projectile interior of the intersecting surface in the projectile nucleus and target nucleus respectively. The mean free path λ is an energy-dependent quantity,[44] and it is taken as $\lambda = 16.6/E^{0.26}$. The parametric constant F is a value depends on the nature of the collision and the relative size of the colliding nuclei. As shown in the Appendix, one can obtain the effective mean free path by considering the Pauli-blocking and the Fermi-motion for a low-energy nucleus-nucleus collision. Since a nucleon is removed for every 10 MeV of the excitation energy during the ablation stage, the ablation factor $\Delta_{\rm abl}(b)$ is given by

$$\Delta_{\rm abl}(b) = \frac{E_s(b) + E_x(b)}{10} \tag{3.7}$$

where $E_s(b)$ and $E_x(b)$ are the excitation energies. The complete procedure for determining the values of $C_P(b)$, $C_T(b)$, F, $E_s(b)$ and $E_x(b)$ is given in reference 27 and reference 37.

The cross section $\sigma(\Delta A)$ for the mass removal of $\Delta A(b)$ nucleons is obtained using the abrasion-ablation model of Bowman et al.,[43] and it is given by

$$\sigma(\Delta A) = \pi(b_1^2 - b_2^2) \tag{3.8}$$

where b_1 and b_2 are the impact parameters which correspond to the inner radius and the outer radius of a cylinder-in-sphere shape target nucleus. The volume of the intersection of the projectile contains $\Delta_{abr}(b)$ nucleons and the excitation energies give $\Delta_{abl}(b)$ nucleons at the rate of one nucleon for every 10 MeV of excitation energy such that

$$\Delta_{abr}(b_1) + \Delta_{abl}(b_1) = \Delta A - 1/2 \tag{3.9}$$

$$\Delta_{abr}(b_2) + \Delta_{abl}(b_2) = \Delta A + 1/2 \tag{3.10}$$

The charge distribution of the final projectile fragments is normalized by the Rudstam formula[45] as

$$\sigma(\Delta A) = \sum_{Z_F} \sigma(A_F, Z_F) \tag{3.11}$$

where $\sigma(A_F, Z_F)$ is the Rudstam charged target fragmentation distribution, and A_F and Z_F are the mass and charge numbers of the fragment respectively. The Rudstam formula for $\sigma(\Delta A)$ was not used in NUCFRG because ΔA-dependence is so simple and breaks down for heavy targets.[36,37] The charge of the removed nucleons is calculated according to charge conservation as

$$\Delta Z = Z_P - Z_F \tag{3.12}$$

and is divided among the nucleons and alpha particles according to the following rules: (1) The abraded nucleon charge is proportional to the charge fraction of the

projectile nucleus and is given by $Z_{\rm abr} = \frac{Z_P \Delta_{\rm abr}}{A_P}$. (2) The charge release in the ablation process is given by $Z_{\rm abl} = \Delta Z - Z_{\rm abr}$.

For the calculation of the cross section $\sigma(\Delta A)$ for the mass removal of ΔA nucleons, the assumption of straight-line trajectories makes the impact parameter to be the closest distance of approach. As a result, the validity of the abrasion-ablation model rests on the high-energy heavy-ion fragmentation. To extend the calculation to a lower energy heavy-ion fragmentation, the Coulomb correction due to the low-energy trajectory must be included.[46] The impact parameter corresponding to the distance of closest-approach in the Coulomb field satisfies

$$b^2 = \left(r^2 - \frac{Z_P Z_T e^2 r}{E_{\rm tot}}\right) \tag{3.13}$$

where r is the separation distance at impact between the two charge centers; Z_P and Z_T are the charges of the projectile nucleus and the target nucleus respectively; e is the electron charge, and $E_{\rm tot}$ is the total energy in the center of mass system.

The Coulomb correction factor is taken as $\Delta' = E_{\rm tot}/(E_{\rm tot} - 5\Delta A)$ and the impact parameter b for a straight-line trajectory is obtained from $b^2 = r(r - r_m)$, where r_m is the distance of closest-approach at zero impact parameter. The Coulomb trajectory is to move the separation at impact r to a smaller impact parameter b. Thus, the new trajectory reduces the cross sections, especially at low energy. The distance of closest-approach r at a given ΔA is used to calculate the impact parameter, and this value is used to evaluate the Coulomb trajectory corrected cross sections. The average kinetic energy in passing through the reaction zone is obtained by assuming that 10 MeV per nucleon is the average binding energy.

In Table 3.1 and in Table 3.2, we tabulate the nuclear fragmentation cross sections for 470A MeV ^{20}Ne + ^{12}C, 210A MeV ^{46}Ar + ^{12}C, and 1.88A GeV ^{56}Fe incident on several nuclei.[27,47,48] The inclusion of the Coulomb correction improves the nuclear data base for low-energy ion fragmentation, but it is relatively ineffective at

energies above 200 MeV per nucleon. In Figure 3.1 and in Figure 3.2, the calculated fragmentation cross sections for the reaction ^{16}O + ^{92}Mo and for the reaction ^{84}Kr + ^{166}Er below 50 MeV per nucleon are compared with the experimental values.[49,50]

3.2 ATOMIC DATA BASE

A charged particle in passing through a material mainly interacts with the negatively charged electrons which occupy most of the volume of the material but posses little of the mass. The charged particle loses its energy continuously, and finally stops after traveling a finite distance called the range. The electrons in the material are raised to excited energy levels, and these energy increments are taken from the kinetic energy of the incident particle. To calculate the energy loss per unit distance, which is called the stopping power, two different processes should be considered. Since the total energy loss mechanism is divided into two processes (electronic interaction and nuclear interaction), the total stopping power $S_T(E)$ is obtained by summing the electronic stopping power $S_E(E)$ and the nuclear stopping power $S_N(E)$ as

$$S_T(E) = S_E(E) + S_N(E) \tag{3.14}$$

where other processes of energy transfer, such as bremsstrahlung and pair production, are ignored in Eq. (3.14). In the present work, the stopping power and the corresponding particle range are calculated using a semiempirical method developed by Ziegler.[38,39]

The energy loss by ionization above 500 keV is adequately described by the Bethe-Bloch formula.[1,27] For low energies below several hundred keV, a satisfactory approach is not available. The electron transfer, or the charge exchange reactions alter the ion charge over its path and the contribution of the electronic stopping power is quite small. As a result, the energy lost by an ion occurs mainly due to nuclear collisions. The Bethe-Bloch formula for the energy loss per unit path length

is given by

$$S_E(E) = \frac{4\pi N Z_P^2 Z_T e^4}{mc^2}\left\{ln\left[\frac{2mv^2}{(1-\beta^2)I_T}\right] - \beta^2 - \frac{C}{Z_T}\right\} \tag{3.15}$$

where Z_P and Z_T are the charges of the projectile nucleus and the target nucleus respectively, N is the number of target molecules per unit volume, m is the electron mass, c is the velocity of light, I_T is the mean excitation energy, and C is the velocity-dependent shell-correction term.[51–56] For an arbitrary composition of material, the Bragg rule[57–61] is used. The electronic stopping power for a heavy-ion is related to the alpha particle stopping power through the effective charge,[62,63] given by

$$Z^* = Z_P\left\{1 - \exp\left(\frac{-125\beta}{Z_P^{2/3}}\right)\right\} \tag{3.16}$$

In Eq. (3.15), the mean excitation energy I_T is obtained from

$$Z_T\, ln(I_T) = \sum f_n\, ln(\epsilon_n) \tag{3.17}$$

where f_n is the electric dipole oscillator strength of the target atom, and ϵ_n is the corresponding excitation energy. Recently, a powerful model was used to calculate electric dipole oscillator strengths.[64–68] This model describes the atom by single-particle hydrogenic wave functions and treats the initial state and the final state by two different effective charge parameters Z_i and Z_f, respectively. The calculated results for a helium-like atom[68] showed that this model can generate values of the dipole oscillator strengths reasonably well.

For the nuclear stopping power, the Ziegler's empirical formula,[38,39,69] which is a modification of the theory of Lindhard, Scharff, and Schiott,[70] is used. There have been several extensive theoretical studies of the nuclear stopping power using the rms (root-mean-square) value of the interatomic potential. This is an empirical formula called the universal interatomic potential.[71–73] This empirical formula is

used to evaluate the nuclear stopping power of an ion in a solid. The accuracy of the empirical fit was less than 1 percent. In reduced units, the nuclear stopping power is given by

$$S_N(E) = \begin{cases} 1.59\epsilon^{1/2} & \epsilon < 0.01 \\ \dfrac{1.7\epsilon^{1/2}\, ln[\epsilon + \exp(1)]}{1.68\epsilon + 3.4\epsilon^{3/2}} & 0.01 < \epsilon < 10 \\ \dfrac{ln(0.47\epsilon)}{2\epsilon} & 10 < \epsilon \end{cases} \tag{3.18}$$

where ϵ is the reduced energy in units of keV/nucleon

$$\epsilon = \frac{32.53\, A_P A_T E}{Z_P Z_T (A_P + A_T)(Z_P^{2/3} + Z_T^{2/3})} \tag{3.19}$$

and A_P and A_T are the atomic masses of projectile and target respectively.

If we neglect the small lateral deflections of the ion, the range is calculated by the integration of the reciprocal of the stopping power as

$$R(E) = \int_0^E \frac{1}{S(E)}\, dE \tag{3.20}$$

and the penetration length is written as

$$\Delta X = R(E_1) - R(E_2) = \int_{E_2}^{E_1} \frac{1}{S(E)}\, dE \tag{3.21}$$

The range was also calculated from Ziegler's empirical form in which a transport algorithm is used to calculate the range distributions for several ions. Calculated ranges for several heavy ions in water are summarized in Table 3.3 as a function of their incident energies.

Table 3.1 The fragmentation cross sections for the reaction $^{20}Ne+^{12}C$ at 470 MeV/nucleon and $^{40}Ar+^{12}C$ at 210 MeV/nucleon.

ΔZ^a	$^{20}Ne+^{12}C$ 470 MeV/nucleon		$^{40}Ar+^{12}C$ 210 MeV/nucleon	
	Exp.[b]	NUCFRG[d]	Exp.[c]	NUCFRG[d]
1	129 ± 3	125.6 (93)		198.7(160)
2	214 ± 3	133.3 (90)	154 ± 26	105.3 (80)
3	155 ± 3	101.7 (71)	122 ± 16	88.99 (71)
4	140 ± 3	84.75 (43)	144 ± 19	78.18 (62)
5	74 ± 2	70.68 (53)	81 ± 15	70.21 (50)
6	33 ± 1	25.57 (21)	112 ± 15	64.11 (40)
7			90 ± 03	58.94 (59)
8			92 ± 13	54.56 (44)
9			65 ± 11	50.52 (49)
10			83 ± 13	46.98 (33)

a. ΔZ denotes the charge removal number.
b. Webber et al. reference 47 (taken from reference 27).
c. Guerreau et al. reference 48 (taken from reference 27).
d. Values in parentheses are the old NUCFRAG values.

Table 3.2 The fragmentation cross sections of ^{56}Fe projectiles at 1.88 GeV/nucleon on ^{7}Li, ^{10}Be, ^{12}C, and ^{65}Cu.

Z_F^a	Li	Be	C	Cu
13	50 ± 05 (45.32)[b]	50 ± 07 (44.75)	83 ± 11 (44.24)	179 ± 27 (68.66)
14	54 ± 05 (47.86)	75 ± 08 (47.36)	57 ± 10 (46.88)	72 ± 11 (71.08)
15	57 ± 06 (50.85)	57 ± 08 (50.41)	59 ± 10 (49.82)	88 ± 15 (74.09)
16	56 ± 06 (54.50)	63 ± 08 (53.45)	54 ± 10 (52.95)	56 ± 11 (77.62)
17	38 ± 04 (57.82)	54 ± 07 (57.14)	53 ± 07 (56.65)	86 ± 13 (81.40)
18	55 ± 06 (61.70)	54 ± 07 (61.07)	55 ± 09 (60.59)	95 ± 15 (85.60)
19	56 ± 05 (66.32)	65 ± 07 (65.95)	52 ± 07 (65.14)	88 ± 14 (90.94)
20	64 ± 06 (72.10)	68 ± 07 (71.36)	78 ± 11 (70.87)	98 ± 14 (97.05)
21	67 ± 06 (79.27)	77 ± 08 (78.46)	54 ± 09 (77.75)	100 ± 15 (105.2)
22	75 ± 06 (89.10)	83 ± 09 (88.26)	87 ± 11 (87.40)	101 ± 14 (116.3)
23	88 ± 07 (102.9)	88 ± 09 (102.1)	100 ± 11 (101.2)	121 ± 15 (132.1)
24	98 ± 07 (125.3)	111 ± 09 (124.4)	124 ± 13 (123.5)	149 ± 16 (157.4)
25	141 ± 18 (185.3)	156 ± 21 (184.4)	181 ± 27 (184.3)	219 ± 20 (267.9)
Total	1443.82	1558.59	1698.22	3026.13

a. Z_F is the fragment charge number.
b. Quantities in parentheses are the values from refernce 27.

Table 3.3 The calculated ranges (g/cm^2) of several ions from 0.025 GeV/nucleon up to 1.0 GeV/nucleon.

E^a	^{7}Li	^{9}Be	^{12}C	^{16}O	^{20}Ne	^{30}Si	^{40}Ar	^{56}Fe
0.025	0.492	0.357	0.213	0.162	0.132	0.093	0.089	0.067
0.050	1.717	1.243	0.738	0.556	0.447	0.304	0.286	0.203
0.075	3.562	2.577	1.529	1.149	0.922	0.621	0.580	0.402
0.100	5.950	4.307	2.555	1.919	1.537	1.031	0.961	0.658
0.200	20.05	14.50	8.603	6.452	5.166	3.449	3.199	2.164
0.300	39.74	28.74	17.03	12.78	10.23	6.820	6.320	4.259
0.400	63.59	45.99	27.25	20.44	16.37	10.91	10.11	6.802
0.600	119.7	86.53	51.28	38.47	30.80	20.53	19.01	12.78
0.800	183.3	132.6	78.56	58.92	47.13	31.42	29.10	19.55
1.000	251.5	181.9	107.7	80.83	64.67	43.11	39.93	26.82

a. in unit of GeV/nucleon

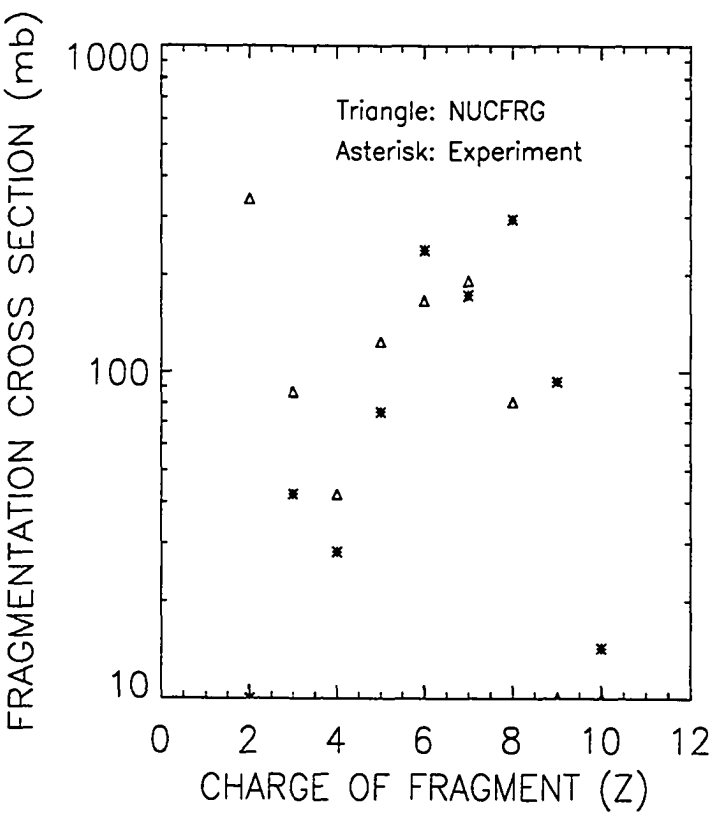

Figure 3.1 Fragmentation cross sections for 11.7 MeV/nucleon ^{16}O + ^{92}Mo collision. The Coulomb correction is included in the NUCFRG results, and the experimental data are taken from reference 49.

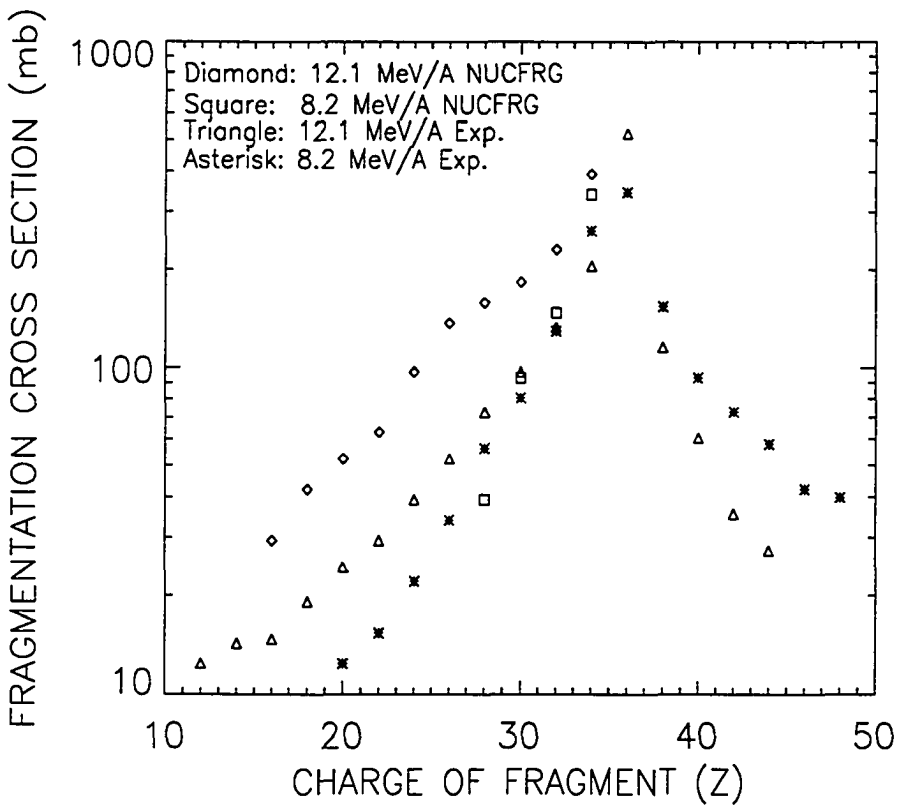

Figure 3.2 Fragmentation cross sections for the reaction $^{84}Kr + ^{166}Er$ collision at 8.2 MeV/nucleon and at 12.1 MeV/nucleon. The Coulomb correction is included in the NUCFRG results, and the experimental data are taken from reference 50.

CHAPTER 4

RESULTS AND COMPARISON 1: GREEN'S FUNCTION

The energy-dependent attenuation coefficient shows a difference of a few to about 10 percent from the values obtained from the energy-independent Green's function method. The first-collision Green's function shows large difference, but its contribution to the total Green's function is relatively small. The difference between the two formalisms is mainly due to the attenuation term and the first-collision term. For most ions with energy above $300A$ MeV, the energy-independent monoenergetic attenuation terms are underestimated. On the other hand, the first-collision terms are overestimated in the energy-independent formalism.

4.1 ENERGY-DEPENDENT GREEN'S FUNCTION: ATTENUATION

The attenuation is the most fundamental feature in the transport of an ion. To understand the energy dependence of the nuclear cross section on the attenuation term, we calculated a relative ratio of the attenuation terms of the energy-dependent Green's function method and the energy-independent Green's function method as a function of depth. We used the nuclear cross sections at $2000A$ MeV in the energy-independent method. In Figure 4.1 through Figure 4.5, we show the ratio of the energy-dependent attenuation coefficients to those values obtained from the energy-independent method for ^{7}Li, ^{12}C, ^{20}Ne, ^{40}Ar, and ^{56}Fe incident on a water target with incident energies between $50A$ MeV and $1000A$ MeV. As shown in Figure 4.1 through Figure 4.5, heavy nuclei have shorter ranges than light nuclei of the same initial energy. Ions with incident energy below $200A$ MeV are completely stopped

within a depth of 5 cm, except for a few light ions such as ^{7}Li. These features are due to the Z^2-dependence of the stopping power. The contribution of energy-dependent nuclear cross sections becomes important when the ion penetrates deeper.

The characteristic shape of the ratio can be investigated from the correlation between the nuclear absorption cross section and the extinction coefficient $O(E)$ given in Eq. (2.55). In Table 4.1, we summarize these two values for ^{12}C, ^{20}Ne, ^{40}Ar, and ^{56}Fe. As shown in the table, most ions have larger extinction coefficients than nuclear absorption cross sections for energies ranging from 50A MeV to 400A MeV. The nuclear absorption cross section decreases slowly up to about 300A to 400A MeV and starts to increase above this energy, while the extinction coefficient continues to decrease up to about 500A MeV to 600A MeV. The nuclear absorption cross sections at 100A MeV and at 2000A MeV are approximately the same. For incident energies below 100A MeV, the ratio is slightly lower than one and continues to decrease. This is due to the fact that the nuclear cross section at 2000A MeV, which we used for the energy-independent nuclear cross sections, is very close or slightly less than the cross section at 100A MeV. Above 100A MeV, the extinction coefficients are smaller than the nuclear cross sections. Since the nuclear cross sections between 100A MeV and 2000A MeV are smaller than those values at 100A MeV and 2000A MeV, the ratio is greater than one.

When the incident ion reaches the depth corresponding to its primary range around 100A MeV, the ratio starts to increase. As shown in Figure 4.2, the range of the ^{12}C ion with 300A MeV is approximately 17 cm in water. When the ^{12}C ion reaches the depth of 15 cm, the energy of the primary ^{12}C ion is approximately 90A MeV. Since the nuclear absorption cross section is smaller than the extinction coefficient at this energy, and these two values become close when the energy of ^{12}C ion reaches 50A MeV, the ratio quickly drops after a slow increase.

The energy-dependence of the nuclear cross section on the attenuation term was

dominant for light nuclei with a deep penetration depth. In Figure 4.6 and Figure 4.7, we showed the ratio as a function of energy at a depth of 5 cm and at a depth of 10 cm. Heavy nuclei, for example ^{56}Fe, show more energy-dependence of nuclear cross sections than lighter ions, such as ^{7}Li. The overall energy-dependence is less than 2 or 3 percent at a depth of 5 cm, while the energy-dependence is increased up to 8 to 10 percent at a depth of 10 cm in water.

The attenuation terms are underestimated in the energy-independent Green's function method for energies between 300A MeV and 1000A MeV. For heavy nuclei, the energy-dependence of the nuclear cross section on the attenuation term becomes significant for deep penetration depths and for high incident energies. At 1000A MeV, most ions show strong energy-dependence of the nuclear cross section on the attenuation term, especially for light nuclei at a deep penetration depth as shown in Figure 4.1 through Figure 4.5.

4.2 ENERGY-DEPENDENT GREEN'S FUNCTION: COLLISION

The propagation of fragments is caused by the secondary production of ions inside a medium. During the propagation process, the projectile ion breaks into pieces by collisions with target nuclei, and the fragment or prefragment particles continue to propagate. In the transport of a heavy-ion, the propagation of the fragments is described by the collision term. The first-collision term represents the ion flux of fragments produced after the first-collision of the incident ion. Since the produced fragments also propagate and collide with other target nuclei until they lose all their energy, other fragments are produced subsequently. Eventually, all kinds of nuclei lighter than the incident ion and the target nuclei are produced.

In this work, we calculated the ion fluxes of ^{7}Li, ^{12}C, ^{20}Ne, ^{30}Si, and ^{40}Ar fragments produced by 600A MeV monoenergetic ^{56}Fe ions incident on a water target. For the energy-independent method, we used the nuclear cross section at 2000A MeV

energy. Note that the nuclear cross sections of heavy ions are almost constant above $1000A$ MeV. The ion flux of the first-collision term depends on the depth, the energy of fragments, and the incident energy. The energy-dependence varies slowly as a function of depth, and the difference between the two methods become significant for heavy fragments.

We compared the ion fluxes of the first-collision Green's function from the two formalisms. In Figure 4.8 through Figure 4.10, we show the ion fluxes of fragments produced by $600A$ MeV ^{56}Fe ions incident on a water target at depths of 5 cm, 10 cm, and 15 cm as a function of the energy of fragments. The energy-dependent Green's function (solid line) was obtained from Eq. (2.35), and the energy-independent Green's function (dotted line) was obtained from Eq. (2.46). The energy-independent Green's function overestimates the flux of the first-collision term. For a light fragment with low energy, the difference of the ion fluxes between the two formalisms becomes large, and those differences are reduced as we increase the energy of the incident ion. For $600A$ MeV ^{56}Fe ions incident on a water target, the largest energy-dependence is seen at a depth of 10 cm for light fragments, and at a depth of 5 cm for heavy fragments. We see that ^{7}Li fragments have the largest energy-dependence among five fragments. As the fragments propagate deeper, the difference of fluxes obtained from the energy-independent method and the energy-dependent method becomes larger.

4.3 APPROXIMATE ENERGY-DEPENDENT GREEN'S FUNCTION

Using the approximate Green's functions, given in Eq. (2.53) and in Eq. (2.62), we recalculated the ion fluxes of fragments. We compared the first-order approximate energy-dependent Green's function, given in Eq. (2.53), with the exact energy-dependent Green's function, given in Eq. (2.35). For a higher-order approximation, energy-dependent nuclear cross sections were used in Eq. (2.62). The first-collision approximate Green's function reproduced the exact energy dependent Green's func-

tion quite accurately. However, it shows slight deviations at deep penetration near the incident ion's range.

In Figure 4.11 through Figure 4.13, we show the results of the first-collision ion fluxes obtained from the approximate Green's functions and the exact energy-dependent Green's functions for the fragments ^{7}Li, ^{12}C, ^{20}Ne, ^{30}Si, and ^{40}Ar produced by ^{56}Fe ions with 600A MeV incident on a water target. The ion fluxes obtained from the approximate energy-dependent Green's function (solid line) are compared with the values obtained from the exact energy-dependent Green's function (dotted line). It shows excellent agreement at depths of 5 cm and 10 cm. A minor deviation is shown for ^{40}Ar at a depth of 10 cm due to the uncertainty of the nuclear fragmentation cross section data base. The linear dependence of the Green's function on the energy of fragments breaks down as the ion propagates deeper. It indicates that the multiplicity of fragments at a deep penetration depth is no longer linearly dependent on energy. The approximate Green's function shows more deviations for light fragments than heavy fragments. The collision terms of the energy-dependent Green's function were reproduced quite reasonably using the first-order collision approximation and the higher-order approximation.

Table 4.1 The nuclear absorption cross sections and the extinction coefficients of ions in water.

E[a]	^{12}C		^{20}Ne		^{40}Ar		^{56}Fe	
	σ^{b}_{abs}	O^{c}	σ_{abs}	O	σ_{abs}	O	σ_{abs}	O
0.025	6.837	6.831	8.855	8.845	12.90	12.88	15.52	15.50
0.050	6.602	6.536	7.841	8.465	11.39	12.33	13.69	14.85
0.075	5.287	6.078	6.827	7.863	9.888	1.45	11.87	13.79
0.100	5.084	5.716	6.566	7.396	9.507	10.76	11.40	12.95
0.200	4.646	5.035	6.009	6.509	8.710	9.449	10.46	11.36
0.300	4.582	4.830	5.942	6.246	8.642	9.076	10.39	10.91
0.400	4.681	4.754	6.065	6.150	8.817	8.939	10.60	10.75
0.600	4.878	4.771	6.313	6.173	9.167	8.967	11.01	10.78
0.800	4.953	4.821	6.400	6.240	9.279	9.061	11.15	10.89
1.000	5.027	4.868	6.487	6.297	9.391	9.137	11.27	10.97
2.000	5.048	4.992	6.517	6.445	9.441	9.326	11.33	11.20

a. in unit of GeV/nucleon
b. σ_{abs}: absorption cross section (m^{-1})
c. O: extinction coefficient (m^{-1})

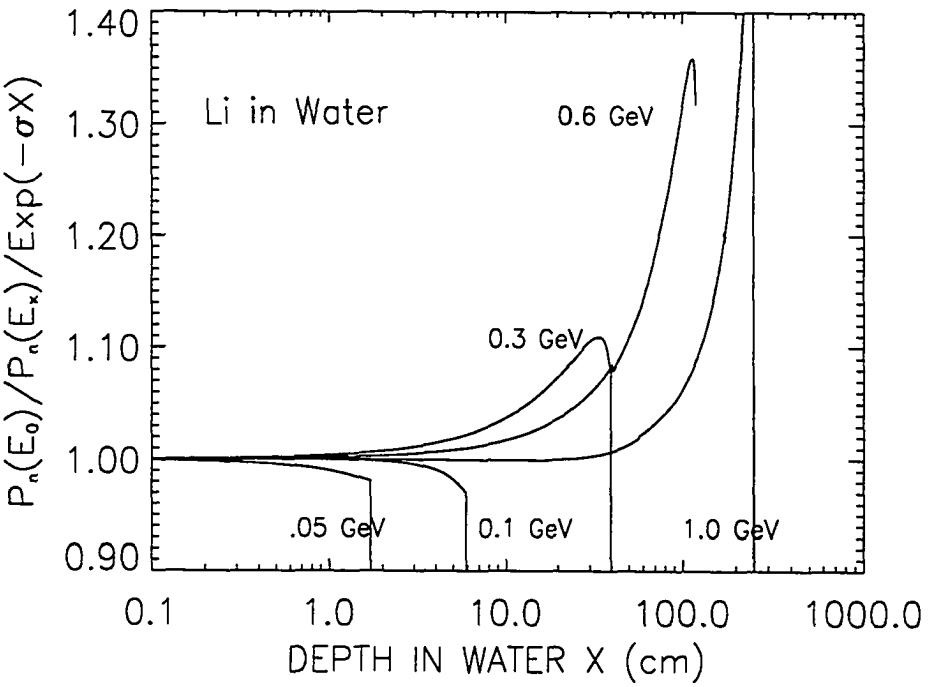

Figure 4.1 The ratio of the attenuation coefficients obtained from the energy-dependent Green's function and from the energy-independent Green's function for ^{7}Li ions incident on a water target as a function of depth.

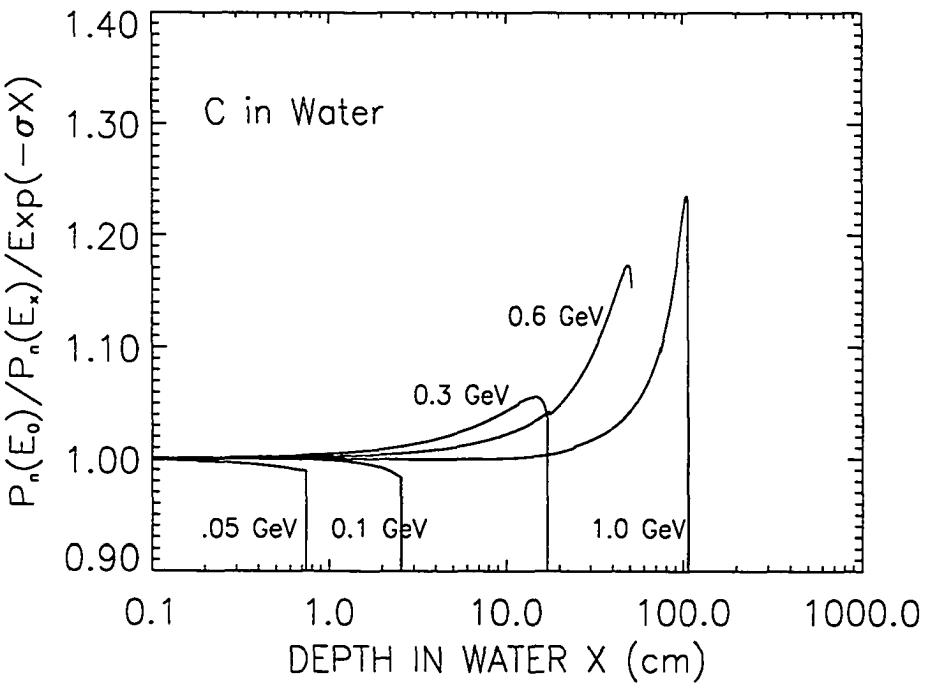

Figure 4.2 The ratio of the attenuation coefficients obtained from the energy-dependent Green's function and from the energy-independent Green's function for ^{12}C ions incident on a water target as a function of depth.

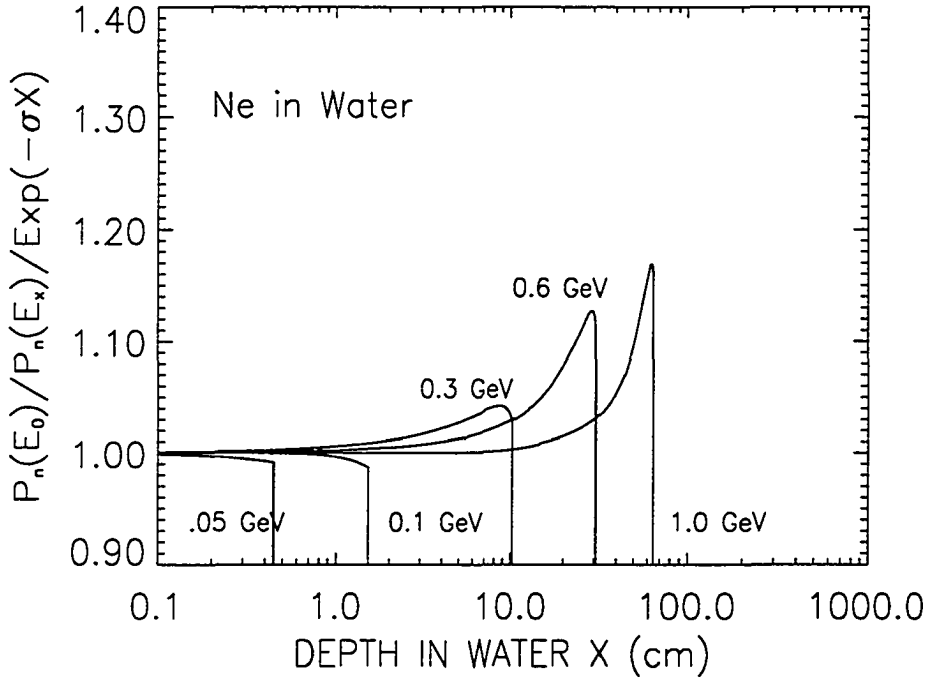

Figure 4.3 The ratio of the attenuation coefficients obtained from the energy-dependent Green's function and from the energy-independent Green's function for ^{20}Ne ions incident on a water target as a function of depth.

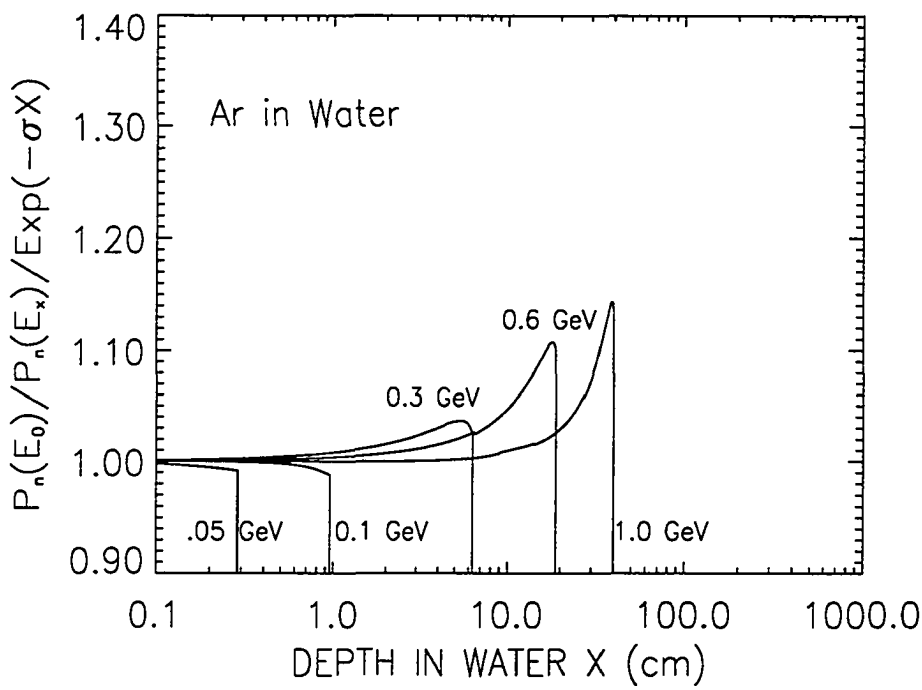

Figure 4.4 The ratio of the attenuation coefficients obtained from the energy-dependent Green's function and from the energy-independent Green's function for ^{40}Ar ions incident on a water target as a function of depth.

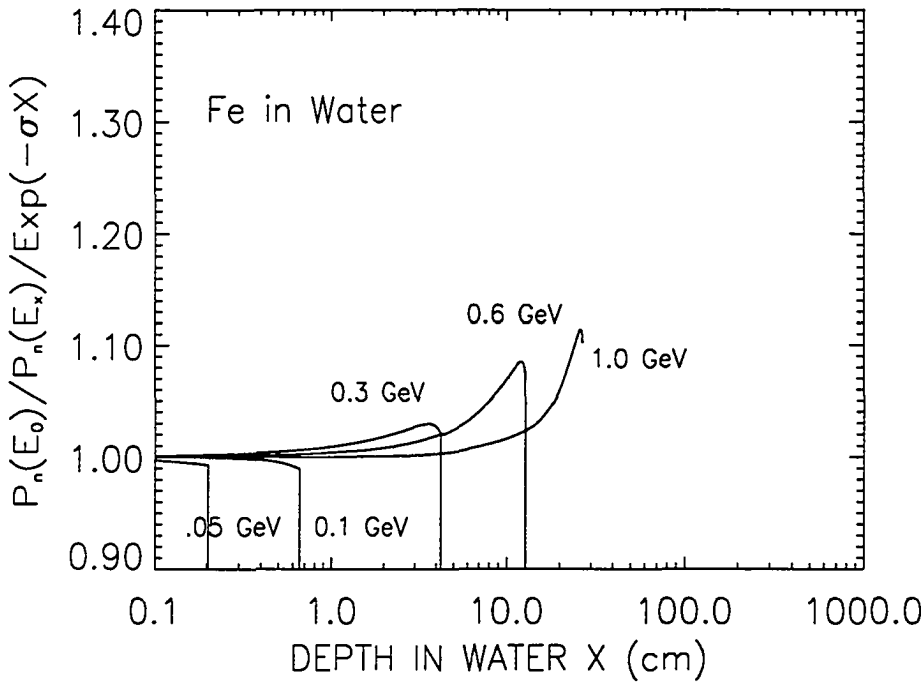

Figure 4.5 The ratio of the attenuation coefficients obtained from the energy-dependent Green's function and from the energy-independent Green's function for ^{56}Fe ions incident on a water target as a function of depth.

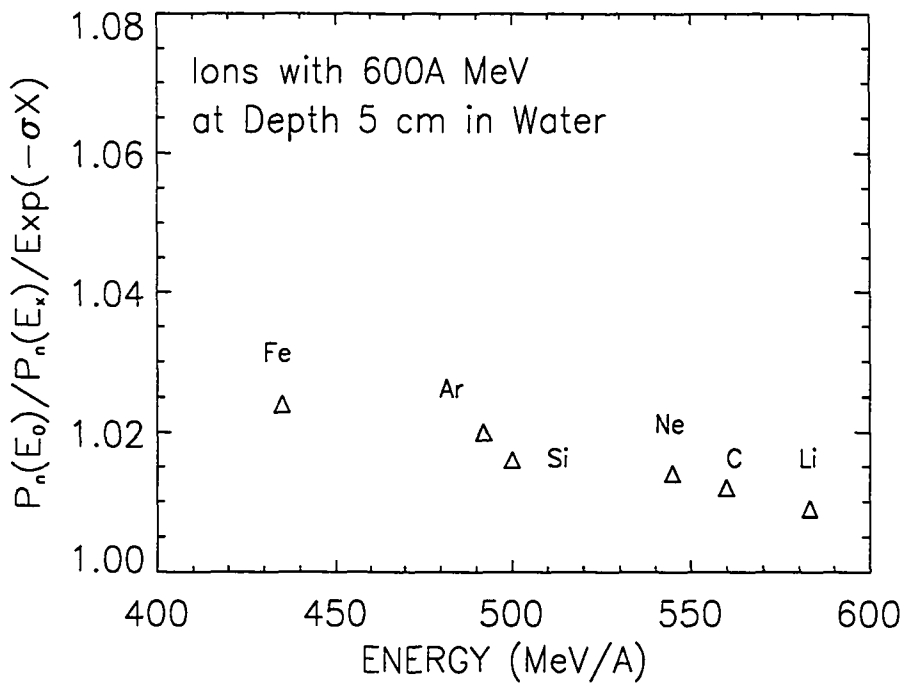

Figure 4.6 The ratio of the attenuation coefficients obtained from the energy-dependent Green's function and from the energy-independent Green's function for ^{7}Li, ^{12}C, ^{20}Ne, ^{30}Si, ^{40}Ar, and ^{56}Fe ions with 600A MeV in water at a depth of 5 cm as a function of energy.

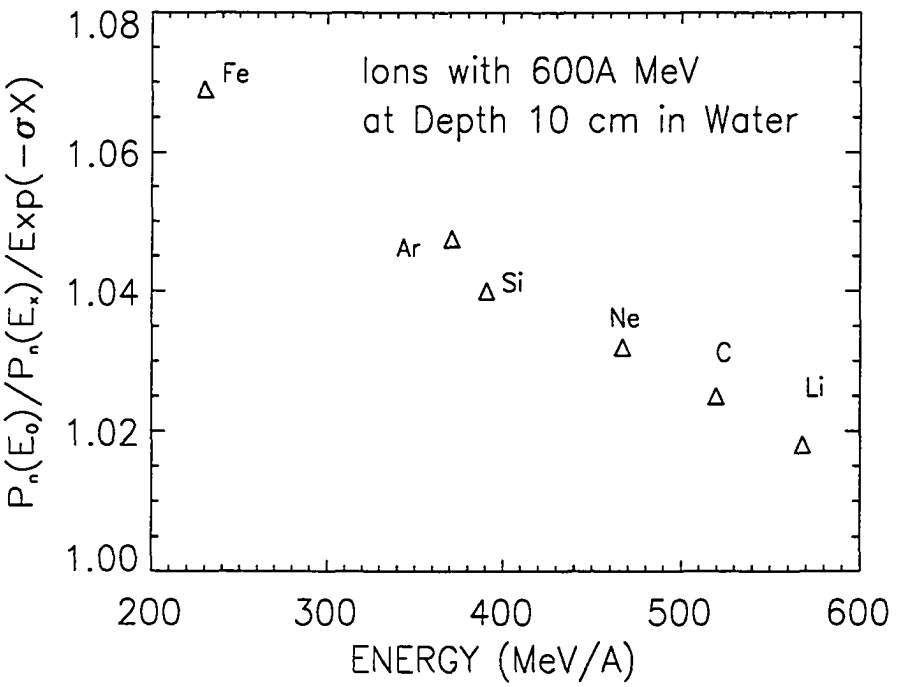

Figure 4.7 The ratio of the attenuation coefficients obtained from the energy-dependent Green's function and from the energy-independent Green's function for ^{7}Li, ^{12}C, ^{20}Ne, ^{30}Si, ^{40}Ar, and ^{56}Fe ions with 600A MeV in water at a depth of 10 cm as a function of energy.

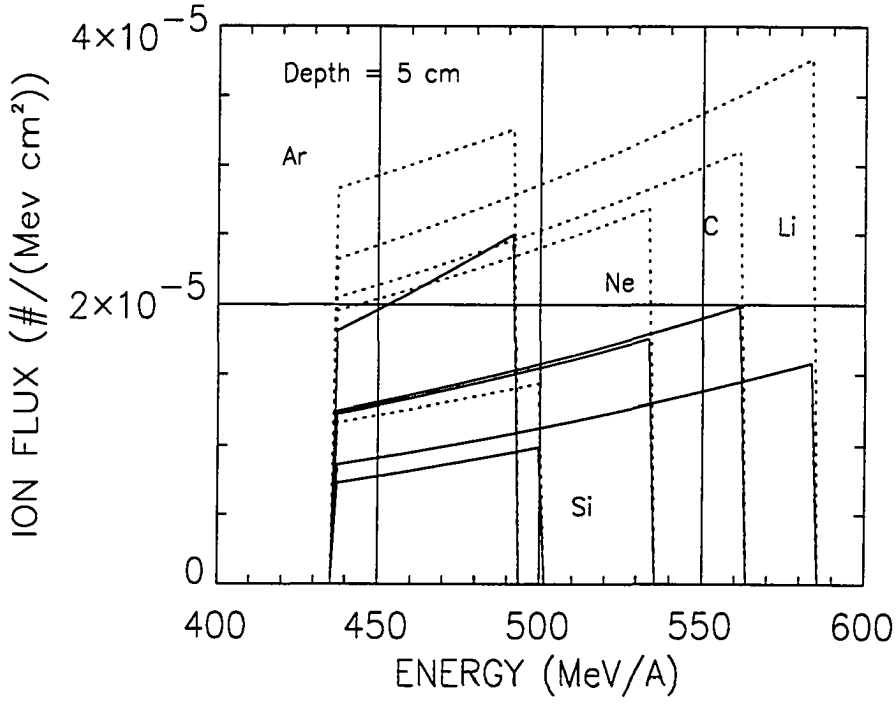

Figure 4.8 The energy-dependent (solid line) and the energy-independent (dotted line) first-collision ion fluxes of ^{7}Li, ^{12}C, ^{20}Ne, ^{30}Si, and ^{40}Ar fragments produced by 600A MeV monoenergetic ^{56}Fe ions in water at a depth of 5 cm.

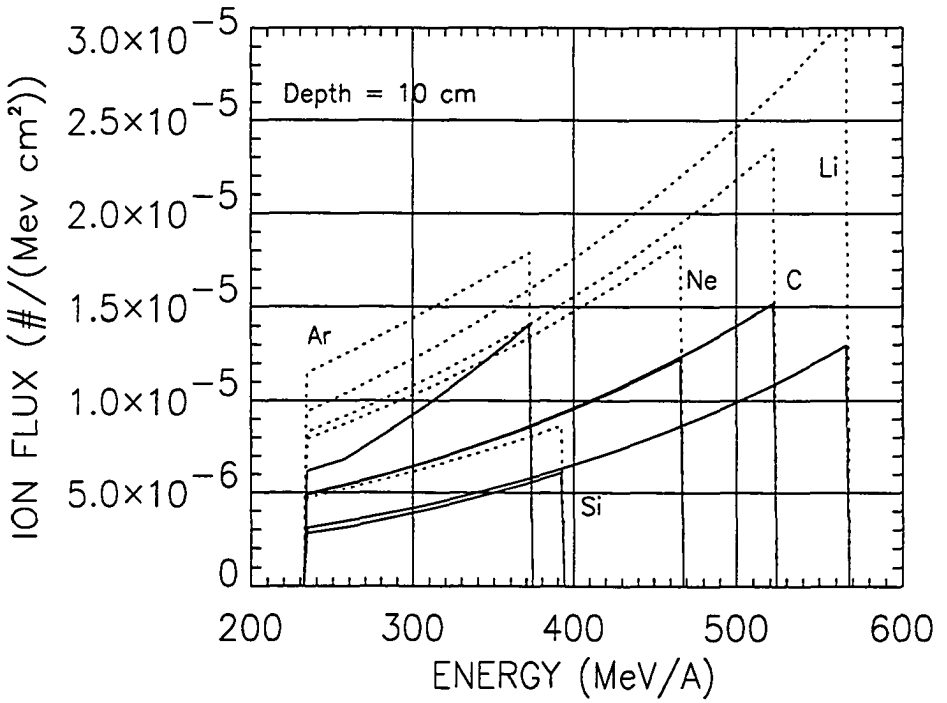

Figure 4.9 The energy-dependent (solid line) and the energy-independent (dotted line) first-collision ion fluxes of ^{7}Li, ^{12}C, ^{20}Ne, ^{30}Si, and ^{40}Ar fragments produced by 600A MeV monoenergetic ^{56}Fe ions in water at a depth of 10 cm.

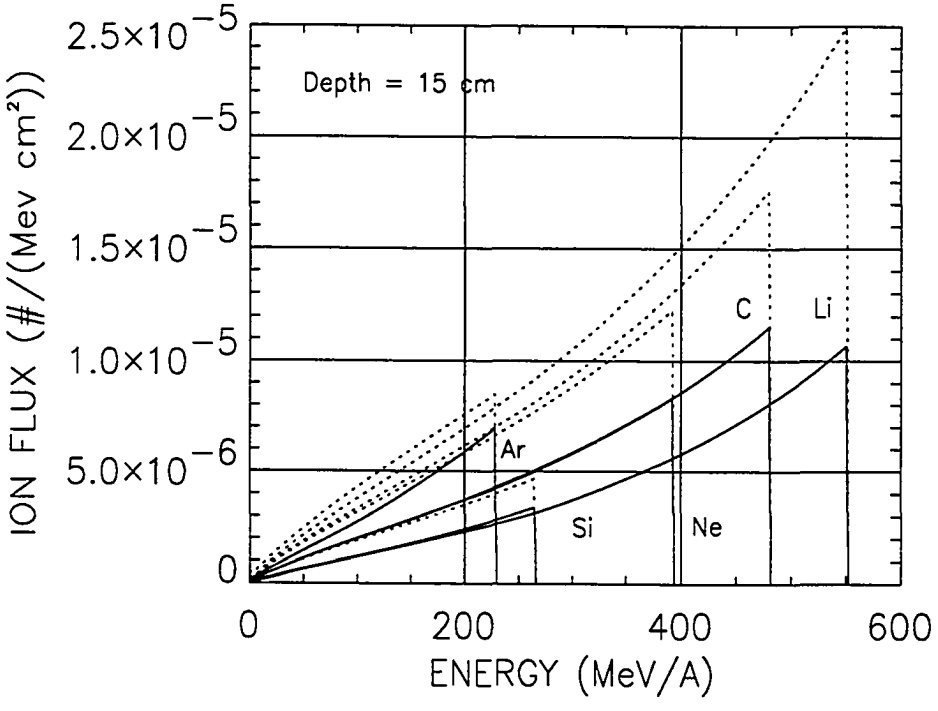

Figure 4.10 The energy-dependent (solid line) and the energy-independent (dotted line) first-collision ion fluxes of ^{7}Li, ^{12}C, ^{20}Ne, ^{30}Si, and ^{40}Ar fragments produced by 600A MeV monoenergetic ^{56}Fe ions in water at a depth of 15 cm.

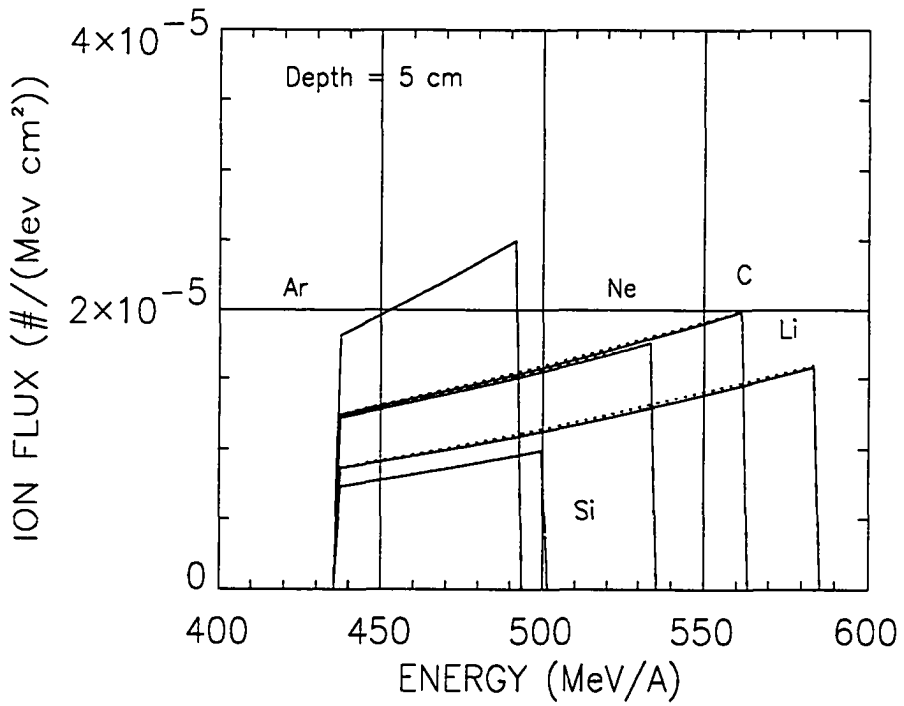

Figure 4.11 The approximate (solid line) and the exact (dotted line) energy-dependent first-collision ion fluxes of ^{7}Li, ^{12}C, ^{20}Ne, ^{30}Si, and ^{40}Ar fragments produced by 600A MeV monoenergetic ^{56}Fe ions in water at a depth of 5 cm.

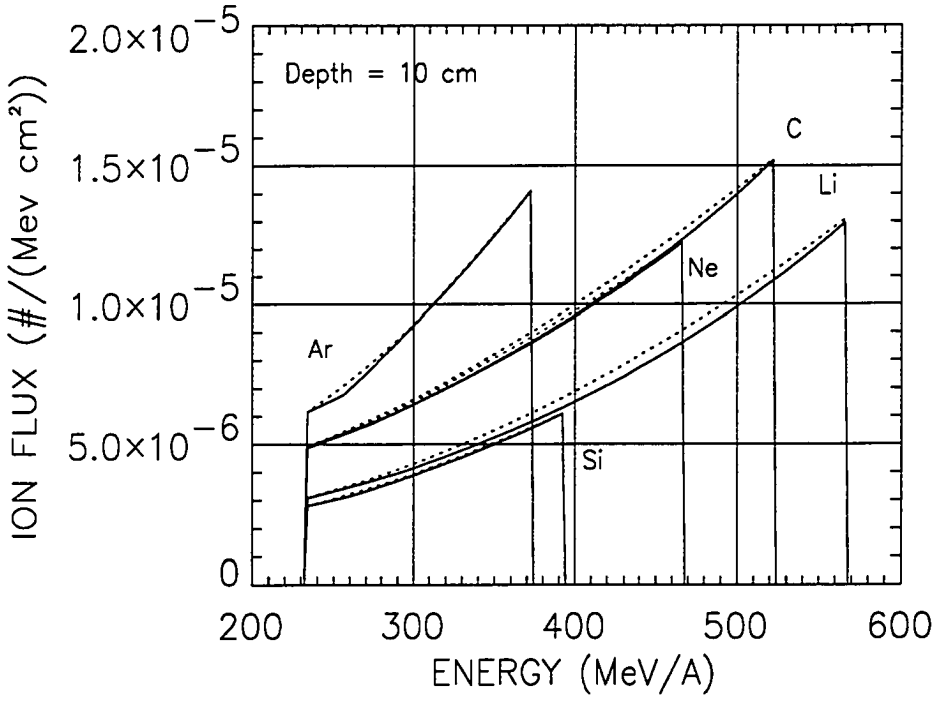

Figure 4.12 The approximate (solid line) and the exact (dotted line) energy-dependent first-collision ion fluxes of ^{7}Li, ^{12}C, ^{20}Ne, ^{30}Si, and ^{40}Ar fragments produced by 600A MeV monoenergetic ^{56}Fe ions in water at a depth of 10 cm.

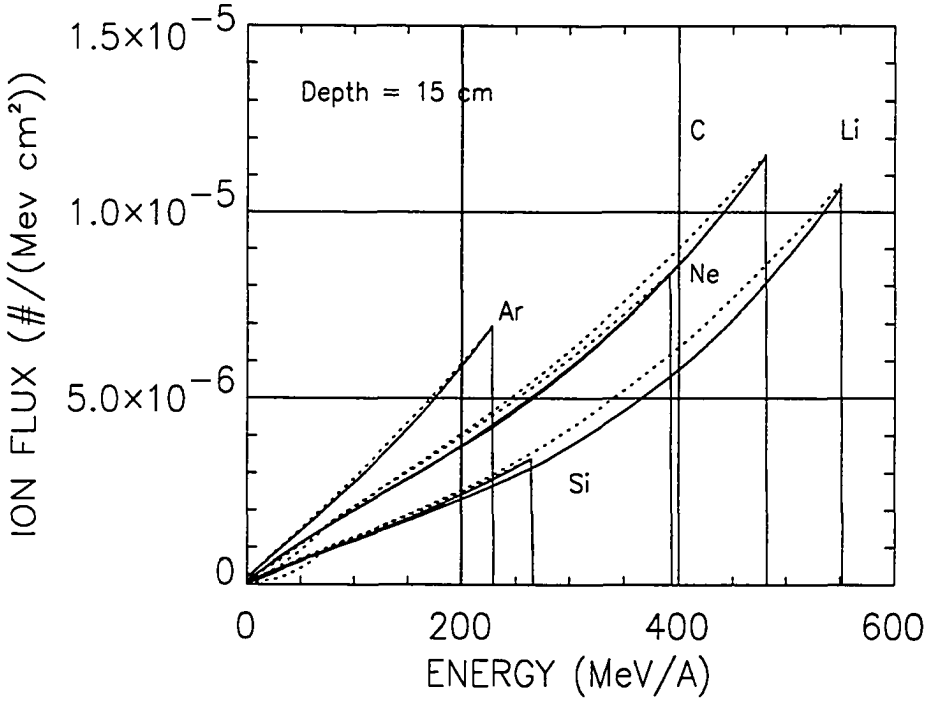

Figure 4.13 The approximate (solid line) and the exact (dotted line) energy-dependent first-collision ion fluxes of ^{7}Li, ^{12}C, ^{20}Ne, ^{30}Si, and ^{40}Ar fragments produced by 600A MeV monoenergetic ^{56}Fe ions in water at a depth of 15 cm.

CHAPTER 5

RESULTS AND COMPARISON 2: PARTICLE FLUX AND DOSE

One of the objectives of this work is to develop a laboratory validated code for estimating biological damages by heavy ions. This goal can be accomplished by obtaining a factor called the average quality factor. In this work, the particle fluxes produced by $600A$ MeV ^{56}Fe ions incident on a water target are calculated. The three-dimensional distribution of the particle flux is obtained. After evaluating the particle fluxes and the Green's functions, we determine doses, dose-equivalents, depth-dose distributions, and average quality factors for ^{20}Ne, ^{40}Ar, and ^{56}Fe ions incident on a water target. The depth-dose distributions are compared with the data measured on the Lawrence Berkely Laboratory (LBL) BEVALAC accelerator[33,34] and with the values obtained from the energy-independent method.[74]

5.1 PARTICLE FLUX

In the Green's function method, the particle flux $\phi_j(x,E)$ for a boundary distribution $f_m(E_0)$ can be obtained by the superposition of Green's functions over the boundary.[31] Thus,

$$\phi_j(x,E) = \int_0^\infty G_{jm}(x,E,E_0)\, f_m(E_0)\, \mathrm{d}E_0 \tag{5.1}$$

where $f_m(E_0)$ is the particle distribution function at the boundary ($x = 0$). For a laboratory ion beam, the Gaussian distribution with energy spread Δ at its boundary is used. The Gaussian distribution function is given by

$$f_m(E_0) = \frac{1}{\sqrt{2\pi}\Delta} \exp\left[- \frac{(E_0 - E_0')^2}{2\Delta^2} \right] \tag{5.2}$$

where E_0' is the mean energy of the incident ion. In a series form, the particle flux $\phi_j(x, E)$ for a distribution $f_m(E_0)$ at its boundary may be approximated by

$$\phi_j(x, E) \approx \sum_{i=0}^{\infty} \phi_j^{(i)}(x, E) \tag{5.3}$$

where

$$\phi_j^{(i)}(x, E) = \int_{E_{0,\min}}^{E_{0,\max}} G_{jm}^{(i)}(x, E, E_0) f_m(E_0) \, \mathrm{d}E_0 \tag{5.4}$$

The attenuation term is obtained in terms of the survival probability as

$$\phi_j^{(0)}(x, E) = \frac{\widetilde{S_j}(E_0)}{\widetilde{S_j}(E)} \frac{P_j(E_0)}{P_j(E)} f_m(E_0) \, \delta_{jm} \tag{5.5}$$

where $E_0 = R_m^{-1}[x + r_j]$. The first-collision term is obtained from Eq. (2.35) as

$$\phi_j^{(1)}(x, E) = \frac{1}{\widetilde{S_j}(E)} \frac{\nu_j}{|\nu_k - \nu_j|} \delta_{km} \int_{E_{0,\min}}^{E_{0,\max}} \sigma_{jk}(E') \times \frac{P_k(E_0)}{P_k(E')} \frac{P_j(E')}{P_j(E)} f_m(E_0) \, \mathrm{d}E_0 \tag{5.6}$$

where E' is given in Eq. (2.36), and $E_{0,\min}$ and $E_{0,\max}$ are the limits of the incident energy given in Eq. (2.38).

The energy-independent particle fluxes are obtained in a similar fashion by introducing the energy-independent Green's functions given in Eq. (2.45) and in Eq. (2.46). The lowest few terms of the energy-independent particle flux are given by

$$\phi_j^{(0)}(x, E) = \frac{\widetilde{S_j}(E_0)}{\widetilde{S_j}(E)} \exp\{-\sigma_j x\} f_m(E_0) \, \delta_{jm} \tag{5.7}$$

$$\phi_j^{(1)}(x,E) = \frac{1}{\widetilde{S_j}(E)} \frac{\nu_j}{|\nu_k - \nu_j|} \delta_{km}\sigma_{jk} \times \int_{E_{0,\min}}^{E_{0,\max}} \exp\Big\{ -\frac{1}{2}\sigma_j (x - r_j - \eta') - \frac{1}{2}\sigma_k (x + r_j + \eta') \Big\} f_m(E_0)\,\mathrm{d}E_0 \tag{5.8}$$

where η' is given in Eq. (2.47). The energy domain for the first-collision term is obtained from the limits given in Eq. (2.37) and in Eq. (2.38). The energy-dependent particle flux for the first-collision term $\phi_j^{(1)}(x,E)$ is approximated as

$$\phi_j^{(1)}(x,E) = \overline{G}_{jm}^{(1)}(x,E)\, I_m + B_{jm}^{(1)}(x,E)\,(I'_m - \overline{E}_0\, I_m) \tag{5.9}$$

where $I_m = \int_{E_{0,\min}}^{E_{0,\max}} f_m(E_0)\,\mathrm{d}E_0$ and $I'_m = \int_{E_{0,\min}}^{E_{0,\max}} E_0\, f_m(E_0)\,\mathrm{d}E_0$.
Using the approximate Green's function for higher-order terms, the approximate energy-dependent particle flux $\phi_j^{(i)}(x,E)$ for $i \geq 2$ is written as

$$\phi_j^{(i)}(x,E) = G_{jm}^{(i)}(x,E,E_0)\, I_m \qquad (i \geq 2) \tag{5.10}$$

where the Green's function $G_{jm}^{(i)}(x,E,E_0)$ for $i \geq 2$ is given in Eq. (5.10).

In order to make a comparison between the two formalisms and to check the reliability of the energy-dependent Green's function method, we evaluated the particle fluxes of the fragments produced by $600A$ MeV ^{56}Fe ions incident on a water target. The energy spread Δ is taken as $1.5A$ MeV. We calculated the fluxes of 80 fragments as a function of the particle's energy at depths of 5 cm, 10 cm, and 15 cm. The results are plotted three-dimensionally for the fragments, and are shown in Figure 5.1 through Figure 5.3. The large contribution of light nuclei, such as α, t, d, and p, can be seen in the figures. This is due to the fact that many heavy fragments break into pieces of light fragments during the propagation. The light fragments below Z=6 are reduced in the figures for a graphical view, and the actual unit is 20 ions MeV^{-1}

cm^{-2}. Neutrons are not included in this calculation, even though the contribution is quite large compared with that of a light fragment. Since the neutron is chargeless, the three-dimensional transport equation should be solved.

The light ions are still emitted at depths greater than the range, as shown in Figure 5.3. The range of a 600A MeV ^{56}Fe ion is approximately 12.8 cm. The propagation of the incident ion and produced fragments can be clearly noticed in Figure 5.1 and in Figure 5.2. As the primary ion propagates deeper, it loses energy and slows down, while more fragments are produced with a wide energy distribution. The fragments produced inside a medium also propagate until they lose all their energy, and finally come to a stop. As a result, at a depth of 15 cm, the propagation of the incident ion is no longer seen. Only the propagation of the produced fragments can be seen. The energy-independent method with 2000A MeV nuclear cross sections overestimated the particle fluxes of fragments throughout the entire depths. For light fragments, the energy-independent method underestimated the total particle fluxes.

5.2 DEPTH-DOSE CURVE

When a charged ion passes through a medium, energy is transferred from the incident ion and the produced fragments to a certain volume of the target material. In this process, the amount of energy absorbed in a unit mass is called the dose. To provide a factor that describes the relative effectiveness of a given absorbed dose of a specific type of radiation, the quality factor is introduced. The resultant modified dose is called the dose-equivalent. We evaluated the dose and the dose-equivalent by the use of the energy-dependent Green's functions and the energy-dependent particle fluxes. We also evaluated the relative depth-dose distributions for 625A MeV ^{20}Ne ions and 517A MeV ^{40}Ar ions incident on a water target.

The dose and the dose-equivalent are expressed in series forms, and the energy-dependent approximate Green's functions are used. The dose of an ion at a depth x

is then given by

$$D_m(x) = \sum_j A_j \int_0^\infty \widetilde{S_j}(E)\,\phi_j(x,E)\,\mathrm{d}E \tag{5.11}$$

where $\phi_j(x,E)$ is the particle flux at depth x with energy E, $\widetilde{S_j}(E)$ is the energy loss per unit length (stopping power) of the ions of type j, m is the type of the incident ion, and A_j is the mass of fragment ions. The dose-equivalent is defined in a similar manner using the quality factor which is a function of the linear energy transfer L_j. Then, the dose-equivalent is expressed as

$$H_m(x) = \sum_j A_j \int_0^\infty \widetilde{S_j}(E)\,Q(L_j)\,\phi_j(x,E)\,\mathrm{d}E \tag{5.12}$$

where $Q(L_j)$ is the quality factor of the ions of type j with the linear energy transfer L_j. In the present work, the quality factor of the ICRP 1990[15] recommendation is used, and this is given by

$$Q(L_j) = \begin{cases} 1 & L < 10 \quad (keV/\mu m) \\ 0.32L - 2.2 & 10 \le L \le 100 \quad (keV/\mu m) \\ 300/\sqrt{L} & L > 100 \quad (keV/\mu m) \end{cases} \tag{5.13}$$

The total dose is expressed as

$$D_m(x) \approx \sum_i D_m^{(i)}(x) \tag{5.14}$$

where

$$D_m^{(i)}(x) = \sum_j A_j \int_0^\infty \widetilde{S_j}(E)\,\phi_j^{(i)}(x,E)\,\mathrm{d}E \tag{5.15}$$

and the total dose-equivalent is written as

$$H_m(x) \approx \sum_i H_m^{(i)}(x) \tag{5.16}$$

where

$$H_m^{(i)}(x) = \sum_j A_j \int_0^\infty \widetilde{S_j}(E)\, Q(L_j)\, \phi_j^{(i)}(x,E)\, \mathrm{d}E \tag{5.17}$$

The particle fluxes $\phi_j^{(i)}(x,E)$ for a monoenergetic boundary distribution are the Green's functions, given in Eq. (2.33), Eq. (2.35), and Eq. (2.62). For a laboratory boundary distribution $f_m(E_0)$, the particle fluxes are given in Eq. (5.5), Eq. (5.6), and Eq. (5.10).

The lowest few terms of the dose for a monoenergetic boundary distribution are obtained as

$$D_m^{(0)}(x,E_0) = \sum_j S_j(E)\, \frac{P_j(E_0)}{P_j(E)}\, \delta_{jm} \tag{5.18}$$

$$D_m^{(1)}(x,E_0) = \sum_j A_j\, \frac{\nu_j}{|\nu_k - \nu_j|}\, \delta_{km} \int_{E_{\min}}^{E_{\max}} \{\zeta(E)\, E_0 + \kappa(E)\}\, \mathrm{d}E \tag{5.19}$$

where $\zeta(E)$ and $\kappa(E)$ are given in Eq. (2.58) and in Eq. (2.59), and $E_{\min}$ and $E_{\max}$ are the limits given in Eq. (2.37). For a laboratory boundary distribution $f_m(E_0)$, we found

$$D_m^{(0)}(x) = \sum_j A_j\, \delta_{jm} \int_{E_{\min}}^{E_{\max}} \widetilde{S_j}(E_0)\, \frac{P_j(E_0)}{P_j(E)}\, f_m(E_0)\, \mathrm{d}E \tag{5.20}$$

$$D_m^{(1)}(x) = \sum_j A_j\, \frac{\nu_j}{|\nu_k - \nu_j|}\, \delta_{km} \int_{E_{\min}}^{E_{\max}} \{\zeta_m(E) + \kappa_m(E)\}\, \mathrm{d}E \tag{5.21}$$

where $\zeta_m(E) = \zeta(E)\, I'_m$ with $I'_m = \int_{E_{0,\min}}^{E_{0,\max}} E_0\, f_m(E_0)\, \mathrm{d}E_0$ and $\kappa_m(E) = \kappa(E)\, I_m$ with $I_m = \int_{E_{0,\min}}^{E_{0,\max}} f_m(E_0)\, \mathrm{d}E_0$.

For the higher-order collision terms ($i \geq 2$), the dose and the dose-equivalent are approximated using the g-function.[1,22,23] For a monoenergetic boundary, the higher-order terms for the dose are given by

$$D_m^{(i)}(x, E_0) = \sum_j A_j \, G_{jm}^{(i)}(x, E) \, I_{Q,j} \qquad (i \geq 2) \qquad (5.22)$$

and for a realistic boundary, these are expressed as

$$D_m^{(i)}(x) = \sum_j A_j \, G_{jm}^{(i)}(x, E) \, I_m \, I_{Q,j} \qquad (i \geq 2) \qquad (5.23)$$

where

$$I_{Q,j} = \int_{E_{\min}}^{E_{\max}} \widetilde{S}_j(E) \, \mathrm{d}E \qquad (5.24)$$

In Eq. (5.24), $I_{Q,j}$ is a smooth function of energy E but it fluctuates at low-energy.

The attenuation term and the first-order collision term of the dose-equivalent for a monoenergetic boundary are expressed as

$$H_m^{(0)}(x, E_0) = \sum_j S_j(E) \frac{P_j(E_0)}{P_j(E)} Q(L_j) \, \delta_{jm} \qquad (5.25)$$

$$H_m^{(1)}(x, E_0) = \sum_j A_j \frac{\nu_j}{|\nu_k - \nu_j|} \delta_{km} \int_{E_{\min}}^{E_{\max}} \{\zeta(E) \, E_0 + \kappa(E)\} \, Q(L_j) \, \mathrm{d}E \qquad (5.26)$$

For a laboratory boundary distribution function $f_m(E_0)$, these are written as

$$H_m^{(0)}(x) = \sum_j A_j \, \delta_{jm} \int_{E_{\min}}^{E_{\max}} \widetilde{S}_j(E_0) \frac{P_j(E_0)}{P_j(E)} Q(L_j) \, f_m(E_0) \, \mathrm{d}E \qquad (5.27)$$

$$H_m^{(1)}(x) = \sum_j A_j \frac{\nu_j}{|\nu_k - \nu_j|} \delta_{km} \int_{E_{\min}}^{E_{\max}} \{\zeta_m(E) + \kappa_m(E)\} \, Q(L_j) \, \mathrm{d}E \qquad (5.28)$$

where $\zeta_m(E)$ and $\kappa_m(E)$ are given in Eq. (5.21). For the higher-order terms ($i \geq 2$) with a monoenergetic boundary distribution, the dose-equivalent is

$$H_m^{(i)}(x, E_0) = \sum_j A_j \, G_{jm}^{(i)}(x, E) \, I'_{Q,j} \qquad (i \geq 2) \qquad (5.29)$$

and for a laboratory boundary distribution $f_m(E_0)$, it is expressed as

$$H_m^{(i)}(x) = \sum_j A_j \, G_{jm}^{(i)}(x, E) \, I_m \, I'_{Q,j} \qquad (i \geq 2) \qquad (5.30)$$

where

$$I'_{Q,j} = \int_{E_{\min}}^{E_{\max}} \widetilde{S_j}(E) \, Q_j(L_j) \, \mathrm{d}E \qquad (5.31)$$

Using Eq. (5.21) through Eq. (5.31), we obtained the dose and the dose-equivalent as a function of depth for 625A MeV ^{20}Ne ions and 517A MeV ^{40}Ar ions in water. The results are compared with the experimental values measured on the LBL BEVALAC accelerator.[33,34] in Figure 5.4 and in Figure 5.5. The dotted lines in the figures denote the partial sum of the energy-dependent perturbation terms. The lowest dotted line from bottom represents the contribution of attenuation term, and the following dotted line from bottom represents the sum of those contributions due to attenuation term and the first-order collision term. The actual experimental incident energy for ^{20}Ne ions was 670A MeV.[33] However, the incident energy when the neon beam enters the water column after passing through several experimental apparatuses[33] was approximately 625A MeV. The results are evaluated by assuming 0.25 percent energy spread. This is a slightly smaller value than the value used in the energy-independent results of Wilson et al.[32] As shown in Figure 5.4 and in Figure 5.5, both the energy-dependent Green's function and the energy-independent Green's function methods slightly underestimated the LBL experimental values. The fluctuation of nuclear fragmentation cross section data causes the difference between the two formalisms and the experimental results. For ^{40}Ar ions, the values from the energy-independent

method are slightly lower than those values obtained from the energy-dependent method.

5.3 AVERAGE QUALITY FACTOR

The average quality factor is an effective quantity based on the quality factor and the linear energy transfer. The average quality factor is known to be an appropriate quantity after surveying many measured values of the relative biological effectiveness (RBE) of radiation, especially at a low absorbed dose. In this work, we obtained average quality factors for 454A MeV ^{20}Ne, 620A MeV ^{40}Ar, and 813A MeV ^{56}Fe ion beams.

In general, the dose-equivalent H_m for a specific type of incident ion m can be related to the dose D_m through a weighting factor $\overline{Q}_m$ which is called the effective quality factor or the average quality factor. Therefore, we may write

$$H_m = \overline{Q}_m D_m \tag{5.32}$$

From Eq. (5.32), the average quality factor $\overline{Q}_m(L)$ is simply defined by

$$\overline{Q}_m(x) = \frac{H_m(x)}{D_m(x)} \tag{5.33}$$

where x is the depth, $D_m(x)$ is the energy transferred to the target medium per unit mass and per unit length, and m refers to the incoming particle. The average quality factor for a monoenergetic boundary is then given by

$$\overline{Q}_m(x, E_0) = \frac{H_m(x, E_0)}{D_m(x, E_0)} \tag{5.34}$$

We evaluated $\overline{Q}_m(x, E_0)$ and $\overline{Q}_m(x)$ for a fixed range R=20 cm for 454A MeV ^{20}Ne, 620A MeV ^{40}Ar, and 813A MeV ^{56}Fe ions in water using the approximate energy-dependent Green's functions. The calculated average quality factors are shown

in Fiqure 5.6 through Figure 5.8. Since we used series forms for the Green's functions and the particle fluxes, the average quality factor is also obtained in a series form. For a monoenergetic boundary distribution, the average quality factor is expressed as

$$\overline{Q}(x, E_0) = \frac{\sum_{i\geq 0} H_m^{(i)}(x, E_0)}{\sum_{i\geq 0} D_m^{(i)}(x, E_0)} \tag{5.35}$$

and for the laboratory boundary with $f_m(E_0)$, we used

$$\overline{Q}(x) = \frac{\sum_{i\geq 0} H_m^{(i)}(x)}{\sum_{i\geq 0} D_m^{(i)}(x)} \tag{5.36}$$

The quantities $H_m^{(i)}(x, E_0)$, $D_m^{(i)}(x, E_0)$, $H_m^{(i)}(x)$, and $D_m^{(i)}(x)$ are given in Eq. (5.21) through Eq. (5.31).

The average quality factor is relatively constant over the range of the primary beam except in the Bragg peak region. For the monoenergetic beam, the average quality factor for ^{20}Ne ions increases quite rapidly around the Bragg peak and then drops. The average quality factor declines slowly at the higher depths over the range because only lighter ions penetrate to those large depths. The average quality factors for ^{40}Ar and ^{56}Fe ions show different characteristics. The strong reduction of the average quality factor at the Bragg peak is shown for ^{40}Ar and ^{56}Fe ions. This is due to the fact that the primary ion quality factor declines as $300/\sqrt{L}$ in Eq. (5.13). Beyond the Bragg peak, a rapid rise in the primary ion quality factor is seen for the monoenergetic boundary distribution. The energy-dependent results with a Gaussian boundary distribution agreed with the energy-independent results with a monoenergetic boundary distribution because we used a relatively small energy spread. Both the energy-dependent method and the energy-independent method show reasonable agreement.

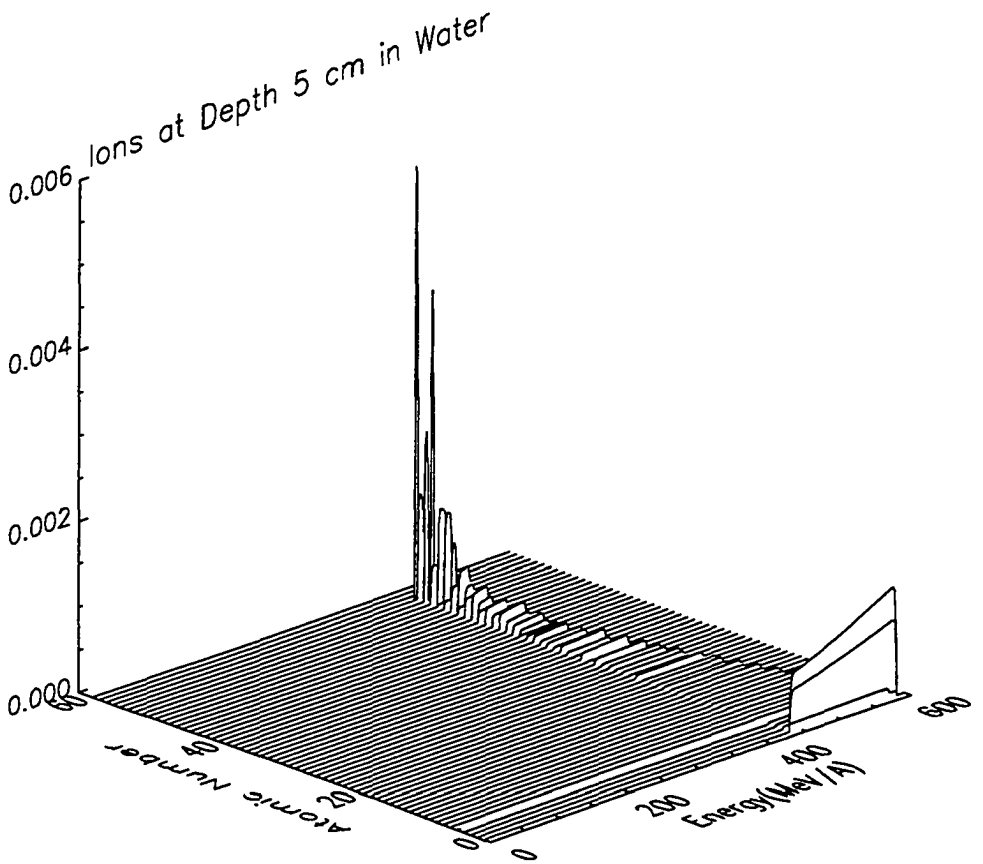

Figure 5.1 Total energy-dependent particle fluxes (ions MeV^{-1} cm^{-2}) as a function of the energy of fragments produced by 600A MeV ^{56}Fe ions at a depth of 5 cm in water.

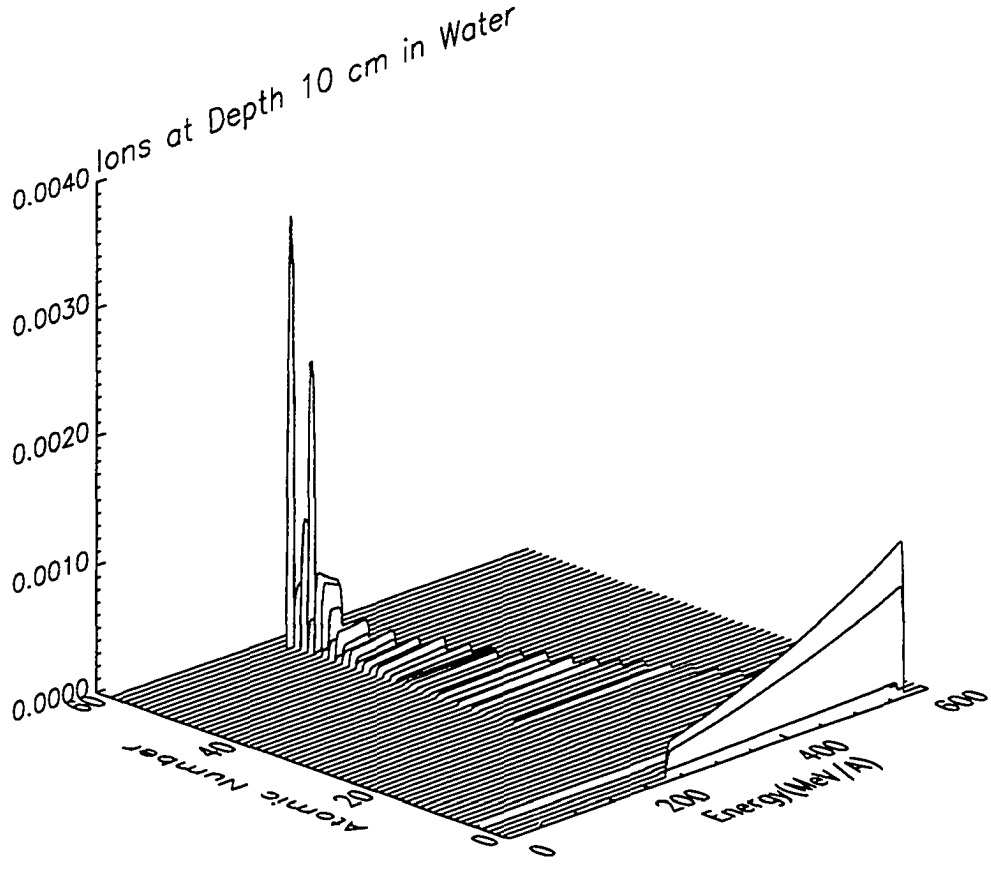

Figure 5.2 Total energy-dependent particle fluxes (ions MeV^{-1} cm^{-2}) as a function of the energy of fragments produced by $600A$ MeV ^{56}Fe ions at a depth of 10 cm in water.

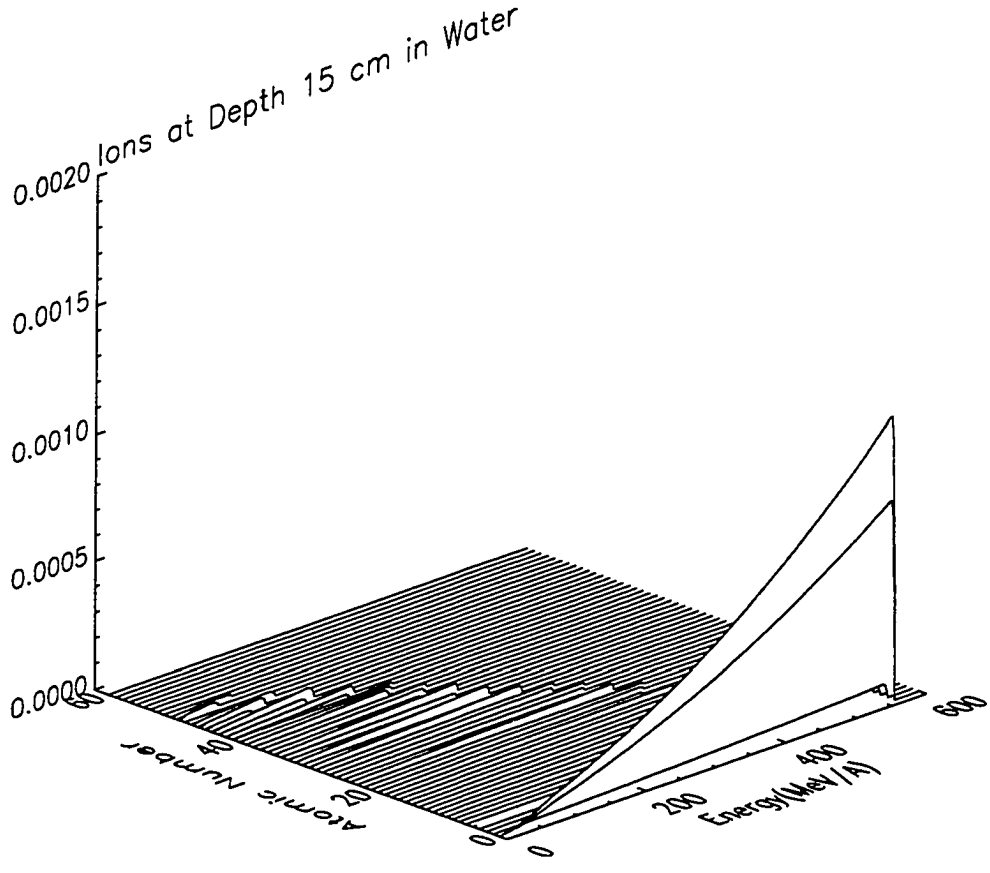

Figure 5.3 Total energy-dependent particle fluxes (ions MeV^{-1} cm^{-2}) as a function of the energy of fragments produced by $600A$ MeV ^{56}Fe ions at a depth of 15 cm in water.

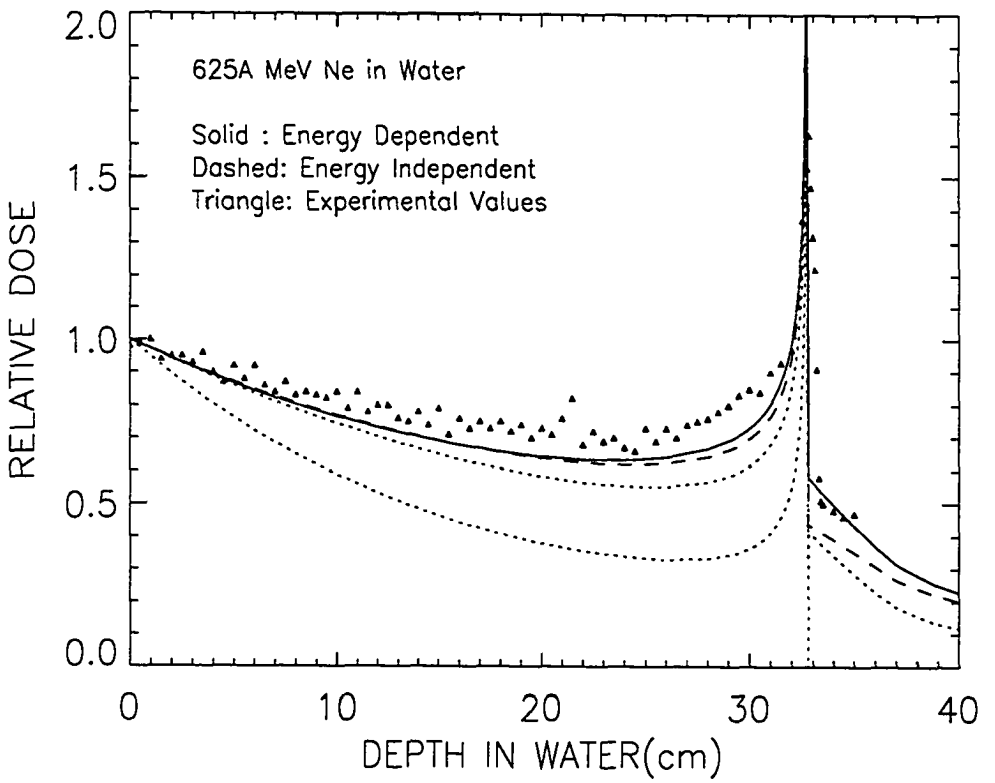

Figure 5.4 The relative depth-dose distribution (Bragg curve) of 625A MeV ^{20}Ne ion beams in water. The values from the energy-dependent method (solid line) are compared with the values from the energy-independent method (dashed line) and the LBL experiments (triangles).

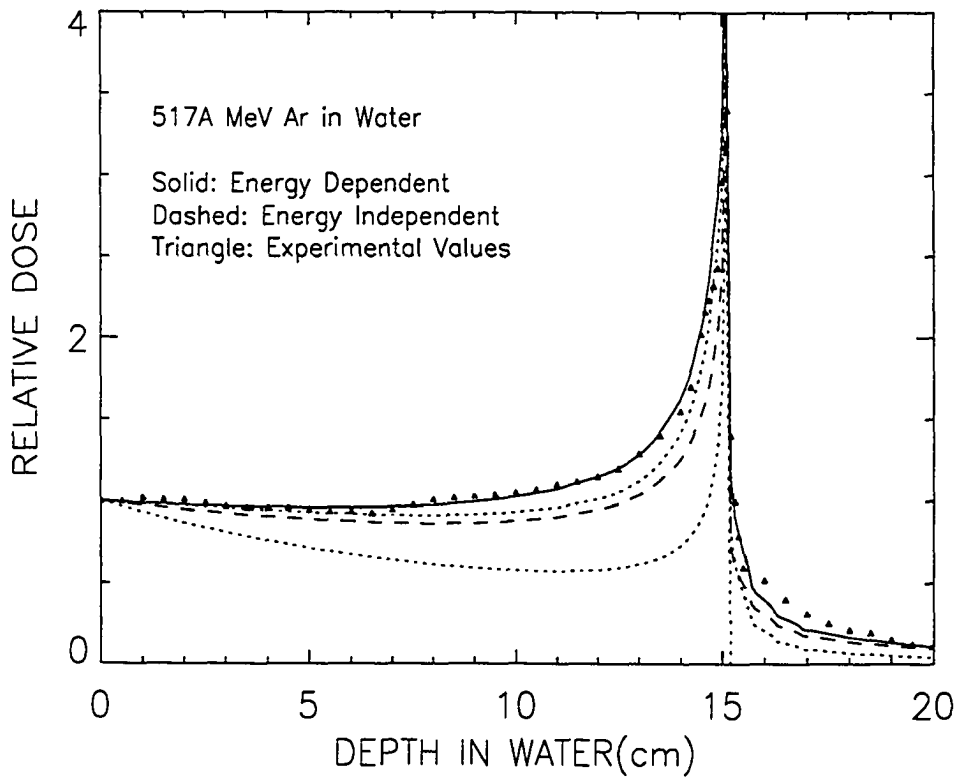

Figure 5.5 The relative depth-dose distribution (Bragg curve) of 517A MeV ^{40}Ar ion beams in water. The values from the energy-dependent method (solid line) are compared with the values from the energy-independent method (dashed line) and the LBL experiments (triangles).

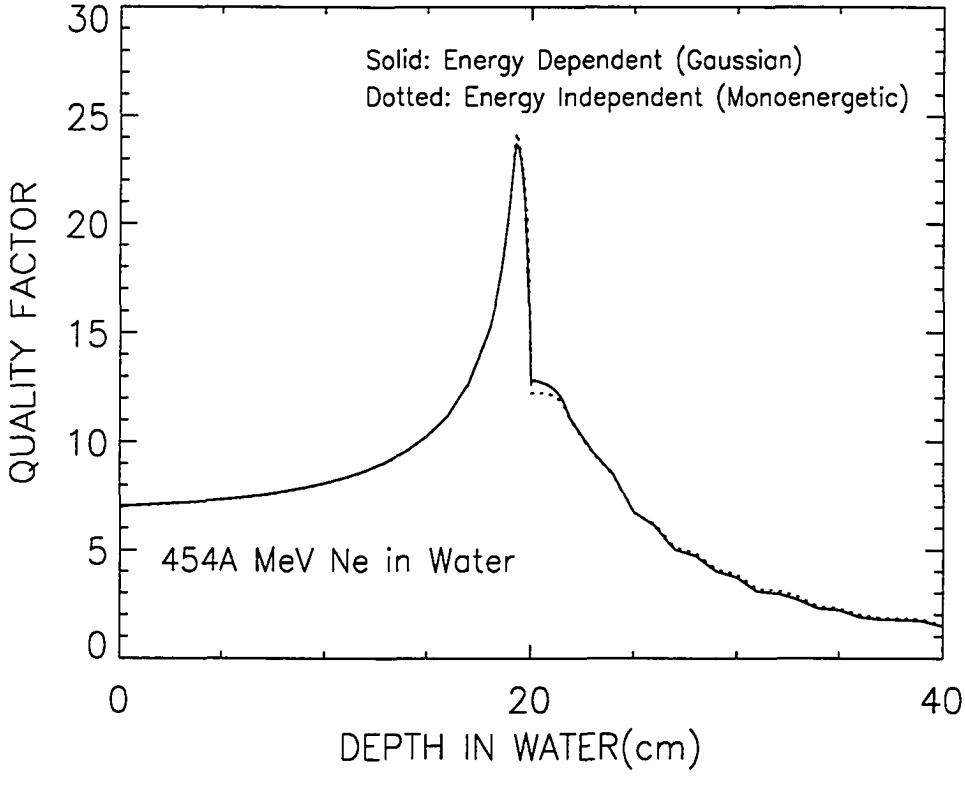

Figure 5.6 Energy-dependent Gaussian (solid line) and energy-independent monoenergetic (dotted line) average quality factors for 454A MeV ^{20}Ne ions in water for a fixed range R =20 cm.

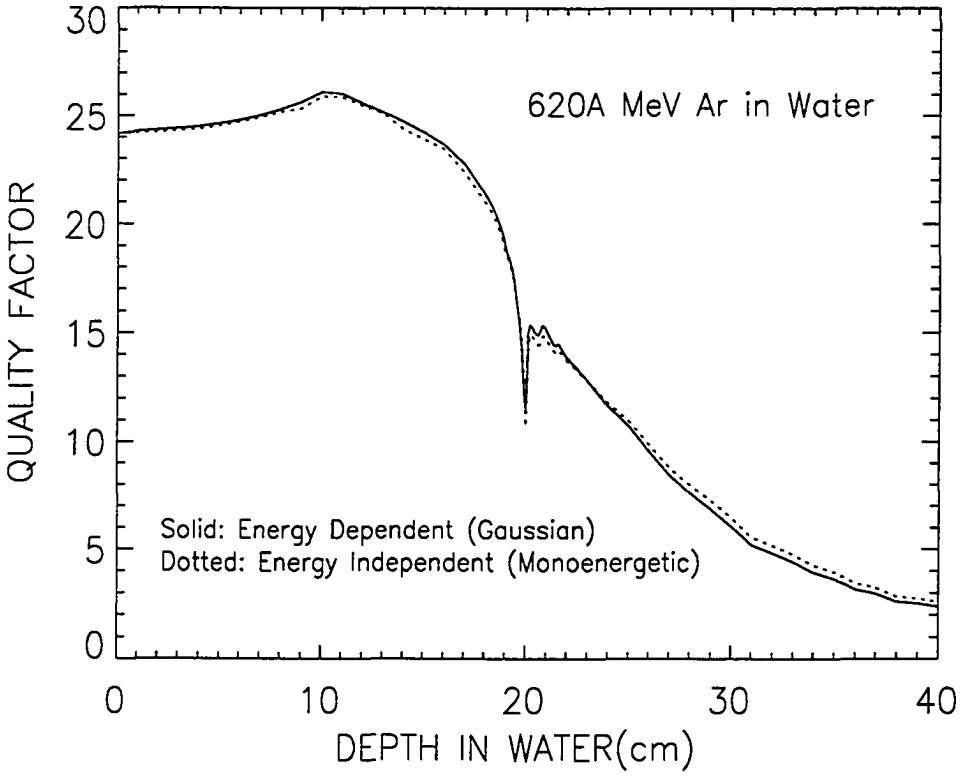

Figure 5.7 Energy-dependent Gaussian (solid line) and energy-independent monoenergetic (dotted line) average quality factors for 620A MeV ^{40}Ar ions in water for a fixed range R =20 cm.

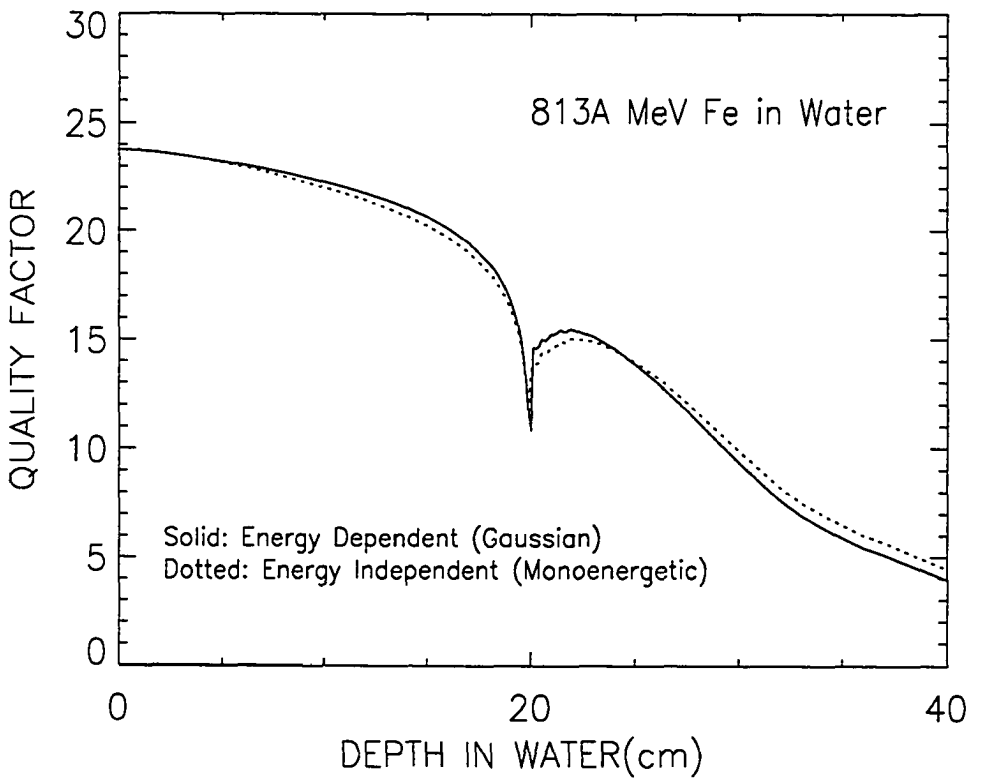

Figure 5.8 Energy-dependent Gaussian (solid line) and energy-independent monoenergetic (dotted line) average quality factors for 813A MeV ^{56}Fe ions in water for a fixed range R =20 cm.

CHAPTER 6
CONCLUSION

In this work, we have solved a heavy-ion transport equation. This work improved the Green's function method and provided more accurate approach to estimate possible biological damage due to the heavy ions in cosmic rays. We obtained the attenuation particle flux of the incident ion and the first-collision particle fluxes of the produced fragments by introducing a fully energy-dependent formalism. The calculated results were compared with the values obtained from the energy-independent formalism. We found that the energy-independent method underestimated the attenuation term and overestimated the first-collision terms of the Green's function for $600A$ MeV ^{56}Fe ions in a water target.

We also developed approximations for the collision terms. For the first-order collision term, we used a linear function. The higher-order collision terms are approximated by removing the ionization-loss term in the transport equation. After evaluating the energy-dependent Green's functions and the fragment fluxes of $600A$ MeV ^{56}Fe ions in water, we obtained depth-dose distributions for $625A$ MeV ^{20}Ne and $517A$ MeV ^{40}Ar ions incident on a water target. We evaluated the average quality factors of ^{20}Ne, ^{40}Ar, and ^{56}Fe ions in water for a fixed range of 20 cm. The calculated depth-dose distributions for $625A$ MeV ^{20}Ne and $517A$ MeV ^{46}Ar ions in water were well agreed with the values measured at the Lawrence Berkeley Laboratory (BEVALAC).[33,34]

In the LBL experiments, comprehensive measurements for $625A$ MeV ^{20}Ne ions incident on a water target have been performed.[33] For $517A$ MeV ^{40}Ar ion beams,

the experimental depth-dose curves were also published.[34] In the ^{20}Ne experiment, the energy spectra of ^{7}Be, ^{9}B, ^{12}C, ^{14}N, ^{16}O, ^{18}F, and ^{20}Ne fragments were measured. The values from the energy-independent formalism were compared with the experimental values in the recent study of Wilson et al.[22] The results obtained from the energy-independent method were reasonably matched within 30 percent. However, the dynamic range of the LBL detector system was found to be inadequate for more specific comparisons for ^{7}Be and ^{9}B. The energy-dependent results showed reasonable agreement with the values obtained from the energy- independent Green's function method.

Until now, fully analyzed experimental data for 600A MeV ^{56}Fe ion beams in water were not available. Due to the strong energy-dependence of the acceptance function of the LBL detector system, it is very hard to compare the calculated results with the experimentally measured values directly. To investigate the validity of the energy-dependent formalism for heavy incident ions, such as ^{56}Fe ion, the energy-dependence of the acceptance function in the detector system should be provided. When we compared the present results with the calculation of Wilson et al.,[22] the energy-dependent results showed reasonable agreement, and the energy-dependent method generated particle spectra quite well. To understand and predict the comparative risks of high LET and low LET radiations due to the energy- dependence of the nuclear cross section, more accurate experimental informations must be provided.

In the future, the accuracy of the higher-order approximation in the two formalisms should be addressed. The development of an accurate nuclear cross section data base is very important. A multidimensional model to include the secondary neutron transport and the target fragmentation should be reformulated using the present energy-dependent formalism. Some other shortcomings of the present calculation, such as the straight-ahead approximation and the velocity conserving assumption, should be resolved.

LIST OF REFERENCES

1. J. W. Wilson, L. W. Townsend, W. Schimmerling, G. S. Khandelwal, F. Khan, J. E. Nealy, F. A. Cucinotta, L. C. Simonsen, J. L. Shinn, and J. W. Norbury, *Transport Methods and Interactions for Space Radiations*, NASA-RP-1257, NASA, Washington, D.C., 1991.

2. J. W. Wilson, L. W. Townsend, and F. F. Badavi, Rad. Res. **109**, 1 (1987).

3. W. Schimmerling, M. Wong, B. Ludewigt, M. Phillips, E. L. Alpen, P. Powers-Risius, R. J. de Guzman, L. W. Townsend, and J. W. Wilson, "Biophysical Aspects of Heavy-ion Interaction in Matter," in *Proc. Conf. on High-energy Radiation Background in Space*, Sanibel Island, ed. by A. C. Rester, Jr., and J. I. Trombka, American Institute of Physics, New York, 1989.

4. M. R. Shavers, J. Miller, W. Schimmerling, J. W. Wilson, and L. W. Townsend, "Multi-generation Transport Theory as an Analytical Heavy-ion Transport Model," in *Proc. of Topical Meeting on New Horizons in Radiation Protection and Shielding*, Pasco, American Nuclear Society, 1992.

5. E. G. Stassinopoulos, "Charged Particle Radiation Exposure of Geocentric Satellites," in *Proc. Conf. on High Energy Radiation background in Space*, Sanibel Island, ed. by A. C. Rester, Jr., and J. I. Trombka, American Institute of Physics, New York, 1989.

6. T. W. Armstrong, and R. G. Alsmiller, Jr., Nucl. Sci. and Eng. **37**, 337 (1969)

7. V. F. Hess, and J. Eugster, *Cosmic Radiation and It's Biological Effects*, Fordham Univ. Press, New York, 1949.

8. J. E. Nealy, L. C. Simonsen, and S. A. Striepe, "Natural Radiation Environment Fluence and Dose Predictions for Missions to the Moon and Mars," in *Proc. of Topical Meeting on New Horizons in Radiation Protection and Shielding*, Pasco, American Nuclear Society, 1992.

9. W. Atwell, E. R. Beever, A. C. Hardy, R. G. Richmond, and B. L. Cash, "Space Radiation Shielding Analysis and Dosimetry for the Space Shuttle Program," in *Proc. Conf. on High-Energy Radiation background in Space*, Sanibel Island, ed. by A. C. Rester, Jr., and J. I. Trombka, American Institute of Physics, New York, 1989.

10. J. W. Wilson, and J. E. Nealy, "Model and Data Base for Background Radiation Exposure of High-Altitude Aircraft," in *Proc. of Topical Meeting on New Horizons in Radiation Protection and Shielding*, Pasco, American Nuclear Society, 1992.

11. K. O'Brian, W. Friedberg, F. E. Duke, L. Snyder, E. B. Darden, Jr., and H. H. Sauer, "Extraterrestrical Radiation Exposure of Aircraft Crews," in *Proc. of Topical Meeting on New Horizons in Radiation Protection and Shielding*, Pasco, American Nuclear Society, 1992.

12. W. Friedberg, D. N. Faulkner, L. Snyder., E. B. Darden, K. O'Brien, Aviation, Space, and Environmental Medicine, 1104 (1989).

13. J. T. Lyman, and J. Howard, Int. J. Rad. Oncology Biol. Phys. **3**, 81 (1977).

14. K. M. V. Apparao, *Composition of Cosmic Radiation*, Gordon and Breach Science Publishers, London, 1975.

15. ICRP, International Commission on Radiological Protection, *1990 Recommendation of the International commission on Radiological Protection*, ICRP Publication 60, Pergamon Press, New York, 1991.

16. M. W. Friedlander, *Cosmic Ray*, Harvard Univ. Press, Cambridge, 1989.

17. J. W. Wilson, L. W. Townsend, S. Y. Chun, W. W. Buck, F. Khan, and F. A. Cucinotta, *BRYNTRN: A Baryon Transport Computer Code, Computation Procedure and Data Base*, NASA-TM-4037, NASA, Washington, D.C., 1988.

18. J. W. Wilson, L. W. Townsend, J. E. Nealy, S. Y. Chun, B. S. Hong, W. W. Buck, S. L. Lamkin, B. D. Ganapol, F. Khan, and F. A. Cucinotta, *BRYNTRN: A Baryon Transport Model*, NASA-TM-2887, NASA, Washington, D.C., 1989.

19. B. D. Ganapol, L. W. Townsend, S. L. Lamkin, and J. W. Wilson, *Benchmark Solutions for the Galactic Heavy-ion Transport Equations with Energy and Spatial Coupling*, NASA-TP-3112, NASA, Washington D.C., 1991.

20. H. G. Paretzke, "Advances in Energy Deposition Theory," in *Advances in Radiation Protection and Dosimetry in Medicine* ed. by R. H. Thomas, and V. Perez-Mendez, Plenum Press., New York, 1980.

21. H. G. Paretzke, "Radiation Track Structure Theory," in *Kinetics of Nonhomogeneous Processes*, ed. by G. R. Freeman, Wiley-Interscience, New York, 1987.

22. J. W. Wilson, R. C. Costen, J. L. Shinn, and F. F. Badavi, *Green's Function Methods in Heavy-ion Shielding*, NASA-TP-3311, NASA, Washington, D.C., 1993.

23. J. W. Wilson, F. F. Badavi, R. C. Costen, and J. L. Shinn, *Nonperturbative Methods in HZE Ion Transport*, NASA-TP-3363, NASA, Washington, D.C., 1993.

24. W. A. Rhodes, *The TORT Three-Dimensional S_n Code*, ORNL-TM-9919, Oak Ridge National Lab., 1986.

25. B. A. Clark, *The Development and Application of the Discrete Ordinates Transfer Matrix Hybrid Method for Deterministic Streaming Calculations*, LA-9357, Los Alamos National Lab., 1982.

26. J. W. Wilson, *Analysis of the Theory of High-Energy Ion Transport*, NASA-TN-D-8381, NASA, Washington, D.C., 1977.

27. J. W. Wilson, S. Y. Chun, F. F. Badavi, L. W. Townsend, and S. L. Lamkin, *HZETRN: A Heavy-ion/Nucleon Transport Code for Space Radiations*, NASA-TP-3146, NASA, Washington, D.C., 1991.

28. J. W. Wilson, and S. L. Lamkin, Nucl. Sci. and Eng. **57**, 292 (1975).

29. J. W. Wilson, *Heavy-ion Transport in the Straight Ahead Approximation*, NASA-TP-2178, NASA, Washington, D.C., 1983.

30. J. W. Wilson, L. W. Townsend, B. D. Ganapol, S. Y. Chun, W. W. Buck, Nucl. Sci. and Eng. **99**, 285 (1988).

31. J. W. Wilson, and G. S. Khandelwal, Nucl. Tech. **23**, 298 (1974).

32. J. W. Wilson, L. W. Townsend, H. B. Bidasaria, W. Schimmeling, M. Wong, and J. Howard, Health Phys. **46**, 1101 (1984).

33. W. Schimmerling, J. Miller, M. Wong, H. Rapkin, J. Howard, H. G. Spieler, and B. V. Jarret, Rad. Res. **120**, 36 (1989).

34. E. A. Blakely, C. A. Tobias, T. C. H. Yang, K. C. Smith, and J. T. Lyman, *Inactivation of Human Kidney Cells by High-Energy Monoenergetic Heavy-ion Beams*, LBL Report, Univ. of California, Berkeley, 1980.

35. L. W. Townsend, and J. W. Wilson, "Nuclear Cross Sections for Estimating Secondary Radiations Produced in Spacecraft," in *Proc. Conf. on High-energy Radiation background in Space*, Sanibel Island, ed. by A. C. Rester, Jr., and J. I. Trombka, American Institute of Physics, New York, 1989.

36. J. W. Wilson, L. W. Townsend, and F. F. Badavi, Nucl. Inst. and Methods in Phys. Res. **B18**, 225 (1987).

37. L. W. Townsend, J. W. Wilson, R. K. Tripathi, J. W. Norbury, F. F. Badavi, and F. Khan, *HZEFRG1: An Energy Dependent Semiempirical Nuclear Fragmentation Model*, NASA-TP-3310, NASA, Washington, D.C., 1993.

38. J. F. Ziegler, Appl. Phys. Lett. **31**, 544 (1977).

39. J. F. Ziegler, *Helium Stopping Powers and Ranges*, Elmsford, New York, Pergamon Press, 1977.

40. L. W. Townsend, and J. W. Wilson, Rad. Res. **106**, 283 (1986).

41. J. W. Wilson, and L. W. Townsend, Can. J. Phy. **59**, 1569 (1981).

42. H. L. Bradt and B. Peters, Phys. Rev. **77**, 54 (1950).

43. J. D. Bowman, W. J. Swiatecki, and C. F. Tsang, *Abrasion and Ablation of Heavy Ions*, LBL-2908, Lawrence Berkeley Lab., Univ. of California, 1973.

44. R. Dymarz, and T. Kohmura, *The Mean Free Path of Protons in Nuclei and Nuclear Radius*, Nucl. Phys. Lab. Rep. 58, Oxford Univ., 1982.

45. G. Rudstam, Zeitschrift für Naturforschung **210**, 1027 (1966).

46. J. W. Wilson, S. Y. Chun, F. F. Badavi, and S. John, *Coulomb Effects in Low-Energy Nuclear Fragmentation*, NASA-TP-3352, NASA, Washington, D.C., 1993.

47. W. R. Webber, D. A. Brautigam, J. C. Kish, and D. A. Schrier, NASA-CP-2376, NASA, Washingtin, D.C., 1985.

48. D. Guerreau, V. Borrel, D. Jacquet, J. Galin, B. Gatty, and X. Tarrago, Phys. Lett. **B131**, 293 (1983).

49. M Lefort, "Mass Distribution in Dissipative Reactions - The Frontier Between Fusion and Deep Inelastic Transfers," in *Deep Inelastic and Fusion Reactions with Heavy Ions*, ed. by W. von Oertzen, vol. 117 of Lecture Notes in Physics, Springer-Verlag, 1980.

50. U. Lynen, "A Fast Splitting of Projectile-like Fragments in the Reaction ^{86}Kr + ^{166}Er at 12.1 MeV/u" in *Deep Inelastic and Fusion Reactions with Heavy Ions*, ed. by W. von Oertzen, vol. 117 of Lecture Notes in Physics, Springer-Verlag, 1980.

51. G. S. Khandelwal, and E. Merzbacher, Phys. Rev. **144**, 349 (1966).

52. G. S. Khandelwal, and E. Merzbacher, Phys. Rev. **151**, 12 (1966).

53. G. S. Khandelwal, Phys. Rev. **167**, 136 (1968).

54. G. S. Khandelwal, Nucl. Phys. **A116**, 97 (1968).

55. G. S. Khandelwal, Phys. Rev. **A5**, 2983 (1982).

56. L. C. Northcliffe, and R. F. Schilling, Nucl. Data Tables **7**, 233 (1970).

57. Y. J. Xu, G. S. Khandelwal, and J. W. Wilson, Phys. Lett. **A100**, 137 (1984).

58. Y. J. Xu, G. S. Khandelwal, and J. W. Wilson, Phys. Rev. **A29**, 3419 (1984).

59. Y. J. Xu, G. S. Khandelwal, and J. W. Wilson, Phys. Lett. **A32**, 629 (1985).

60. Y. J. Xu, G. S. Khandelwal, and J. W. Wilson, Phys. Lett. **A115**, 37 (1986).

61. W. H. Bragg and R. Kleema, Philos. Mag. **10**, 318 (1905).

62. W. H. Barkas, *Nuclear Research Emulsion - Techniques and Theory*, Academic Press, New York, 1963.

63. W. H. Barkas, Phys. Rev. **89**, 1019 (1953).

64. F. Khan, G. S. Khandelwal, and J. W. Wilson, Phys. Rev. **A38**, 6159 (1988).

65. F. Khan, G. S. Khandelwal, and J. W. Wilson, Astrophys. J. **329**, 493 (1988).

66. G. S. Khandelwal, F. Khan, and J. W. Wilson, Astrophys. J. **336**, 504 (1989).

67. G. S. Khandelwal, W. M. Pritchard, G. Grubb, and F. Khan, Phys. Rev. **A39**, 3960 (1989).

68. G. S. Khandelwal, S. Y. Chun, W. M. Pritchard, J. W. Wilson, and F. Khan, *Generalized Oscillator Strengths and Proton-Impact Excitation to N^1-P Levels of the Helium Sequence*, ODURF Rep., MNU-90-01, Old Dominion University Research Foundation, 1990.

69. J. F. Ziegler, *Handbook of Stopping Cross Sections for Energetic Ions in All Elemets*, Pergamon Press, 1980.

70. J. Lindhard, M. Scharff, and H. E. Schiott, "Range Concepts and Heavy Ions," Mat. Phys. Medd. - K. Dan. Vid. Selsk. **33**, 1 (1963).

71. J. P. Biersack, and J. F. Ziegler, Nucl. Inst. and Meth. **194**, 93 (1982).

72. U. Littmark, and J. F. Ziegler, *Ranges of Energetic Ions in Matter*, Phys. Rev. **A23**, 64 (1981).

73. U. Littmark, and J. F. Ziegler, *Handbook of Range Distribution for Energetic Ions in All Elements*, Pergamon Press, New York, 1980.

74. J. W. Wilson, M. Reginatto, F. Hajnal, and S. Y. Chun, *Exposures to High Charge and Energy Ion Beams* (to be published).

75. T. K. Fowler, Phys. Rev. **112**, 1325 (1958).

76. J. P. Garron, J. C. Jacmart, M. Riou, C. Ruhla, J. Teillac, C. Caverzasio, and K. Strauch, Phys. Rev. Lett. **7**, 261 (1961).

77. G. Brown, and H. Murihead, A Journal of Theoretical Experimental Appl. Phys. **8**, 473 (1956).

78. M. S. Hussein, R. A. Rego, and C. A. Bertulani, Phys. Rep. **201**, 279 (1991).

79. A. de Shalit, and H. Feshbach, *Theoretical Nuclear Physics, Vol. I. Nuclear Structure*, John Wiley & Sons Inc., New York, 1972.

80. J. W. Wilson, *Composite Particle Reaction Theory,* Ph.D. Dissertation, College of William and Mary, 1975.

81. L. W. Townsend, *Harmonic Well Matter Densities and Pauli Correlation Effects in Heavy-Ion Collisions*, NASA-RP-2003, NASA, Washington, D.C., 1982

82. K. Kikuchi, and M. Kawai, *Nuclear Matter and Nuclear Reactions,* North-Holland Pub. Inc., New York, 1968.

83. M. L. Goldberger, Phys. Rev. **74**, 1269 (1948).

APPENDIX

EFFECTIVE NUCLEON-NUCLEON MEAN FREE PATHS

1. INTRODUCTION

In the recent years, there has been growing interest in the nucleon-nucleon (N-N) correlations inside nuclei. In this work, we will describe a simple analytical effort to understand the Pauli-blocking and the Fermi-motion in the N-N two-body interaction inside a nucleus. The analysis is carried out within a framework of simple kinematics and basic quantum statistics. The subject is analytically described and tedious mathematical procedures are not given, but it is organized as much as possible in a self-contained manner. The kinematical procedure is very similar in the relativistic calculation unless one uses the on-the-energy-shell transition matrix or the medium correction in the definition of the N-N cross section.

The purpose of this work is to obtain a simple kinematical description of the N-N two-body cross section inside a nucleus, which is called the effective two-body N-N cross section or the quasi-elastic N-N cross section.[75–77] The effective two-body N-N cross sections are very important for the microscopic approach of nuclear reaction theory.[78] In the microscopic nuclear reaction approach, the interaction probability of an incident nucleon or a heavy-ion with a given impact parameter b can be described in terms of the N-N scattering processes. Unlike the free N-N two-body interaction, the N-N interaction inside a nucleus is strongly affected by the Pauli-blocking and the Fermi-motion, and these two medium effects limit the available phase space of the free N-N scatterings inside the nucleus. In this work, in a classical sense, the effective N-N cross section is derived using the Galilean transformation, and the effective mean free

path of constituent nucleons inside a nucleus is obtained. We compared the results with the values obtained from the free N-N interaction.

Since our main interest is on the medium effect due to the Pauli-blocking and the Fermi-motion on the N-N two-body scattering inside a nucleus, it is natural to choose the Fermi-gas model. The Fermi-gas model is the simplest independent-particle model and has been well exploited in many existing reports.[79] The main reason for choosing the Fermi-gas model is the simplicity of the nuclear model. In a many-nucleon system, the nuclear shell model is very difficult to adopt as a nuclear model due to its complexity. For the N-N two-body scattering inside a nucleus, loosely bound nucleons are probable candidates, and only a small fraction of the constituent nucleons near the Fermi-surface is easily excited with a certain amount of the momentum transfer from one occupied state to another state higher than the Fermi-surface. Therefore, the Fermi-gas model is preferable, and it is practically very difficult to use the nuclear shell model. When the incident energy of the projectile nucleon is lower than 200 MeV, these medium effects are very important although we will neglect the Coulomb effect in the present work.

2. PAULI-BLOCKING AND FERMI-MOTION

In the Fermi-gas model, the constituent nucleon moves with a certain momentum below the Fermi-momentum, and this is called the Fermi-motion. As a result, the differential N-N cross section and the total N-N cross section are quite different from those in the rest frame of the target constituent nucleon. When the target nucleus is in its ground state, all the energy states are occupied up to the Fermi-momentum. When a collision occurs between the projectile nucleon and the target constituent nucleons, the only available phase-space for these nucleons to be excited is above the Fermi-surface. Otherwise, collisions can not occur because the Pauli principle prevents two different nucleons from being in the same state. This is called the Pauli-blocking.

When the target nucleus is excited, only a small fraction of the constituent nucleons near the Fermi-surface is easily transferrable. When a collision has occurred, the incident nucleon loses a portion of its energy. If the transferred energy is large enough to get over the Fermi-sea of the target nucleus, the two-body N-N scattering is allowed. When the energy is not large enough to get over the Fermi-energy, the collision is not allowed because there is no available phase-space in the ground state nucleus. Therefore, the final momenta of the two body N-N scattering should exceed the Fermi-momentum in the effective N-N scattering. The role of the binding energy is in the emission process. If the transferred energy is large enough to get over the Fermi-energy, but not large enough to get over the potential well including the Coulomb barrier, the amount of the energy transferred is deposited as excitation energy.

In the Fermi-gas model, a nucleus is considered to be a system of A noninteracting free fermions each with mass of m_N in its ground state. The nucleus has a volume V, and each constituent nucleon has a momentum p_2 with spin s and iso-spin τ. Each nucleon can be described by a well-defined wave function, and the wave function is considered to be a plane wave. The nucleus is assumed to be a quantum gas which obeys the Fermi-Dirac statistics, and shows characteristics of a quantum many-particle system, especially when the de Broglie wavelength of the incoming nucleon becomes comparable to the average spacing between the constituent nucleons. It is assumed that the degenerate Fermi-gas has the property that the system parameters are not modified by the individual interactions. It retains the essential properties of a non-degenerate fermion system, and has a well-defined momentum. This is called the Fermi-momentum.

The nucleon distribution in an element of the phase space inside a nucleus is given by

$$\mathrm{d}N = \lambda \frac{\mathrm{d}^3x\,\mathrm{d}^3p}{h^3} n(\varepsilon) \qquad (A.1)$$

where λ refers to the spin and iso-spin degeneracy, h is the Planck's constant, and $n(\varepsilon)$ is the occupation number. The occupation number $n(\varepsilon)$ for a ground state nucleus is given by

$$n(\varepsilon) = \frac{1}{e^{\beta\varepsilon} + 1} \qquad \text{(for fermions)} \tag{A.2}$$

where ε is the energy of the constituent nucleon, T is the nuclear temperature with $\beta = kT^{-1}$, and k is the Boltzman constant. For a ground state nucleus, the nuclear temperature is zero and the occupation number $n(\varepsilon)$ is then expressed as

$$n(\varepsilon) = \begin{cases} 1 & (\varepsilon < E_F) \\ 0 & (\varepsilon > E_F) \end{cases} \tag{A.3}$$

where E_F is the Fermi-energy. The degeneracy λ represents the spin and iso-spin degree of freedom, and is given by $\lambda = (2s+1)(2\tau+1)$, where s is the spin degeneracy and τ is the iso-spin degeneracy. Since a nucleon has spin $\frac{1}{2}$ and iso-spin $\frac{1}{2}$, the value 4 for λ is used.

The total number of nucleons inside a nucleus is obtained by integrating Eq. (A.1) with $n(\varepsilon) = 1$ over the energy up to E_F as

$$A = \int_0^{E_F} \lambda \frac{2\pi V}{h^3} (2m_N)^{3/2} \sqrt{\varepsilon}\, \mathrm{d}\varepsilon \tag{A.4}$$

The Fermi-energy and the Fermi-momentum for a ground state target nucleus are derived from Eq. (A.4) as

$$E_F = \frac{\hbar^2}{2m_N} \left(\frac{3\pi^2}{2} \rho_0 \right)^{2/3} \tag{A.5}$$

$$p_F = \left(\frac{3\pi^2}{2} \rho_0 \right)^{1/3} \tag{A.6}$$

where ρ_0 is the uniform nuclear density. In Eq. (A.5) and in Eq. (A.6), one can use $\rho(r)$ with the local density approximation to account for the realistic nuclear matter density.

The single particle nuclear matter density ρ_0 is determined from the electron scattering of nuclei and the N-N scattering experiments.[80] The density distribution ρ_0 is obtained from the uniform nuclear radius as

$$R_0 = 1.29 < r^2 >^{\frac{1}{2}} \tag{A.7}$$

where $< r^2 >^{\frac{1}{2}}$ is the nuclear rms (root-mean-square) radius. The nuclear rms radius $< r^2 >^{\frac{1}{2}}$ is obtained in terms of the charge rms radius $< r_c^2 >^{\frac{1}{2}}$ and the mean square of the charge radius as

$$< r^2 >^{\frac{1}{2}} = < r_c^2 >^{\frac{1}{2}} - < r^2 >_p^{\frac{1}{2}} + \frac{N}{Z} < r^2 >_n^{\frac{1}{2}} \tag{A.8}$$

where $< r^2 >_p^{\frac{1}{2}}$ and $< r^2 >_n^{\frac{1}{2}}$ refer to the mean square of the charge radius of the proton and the neutron respectively. The inclusion of the neutron mean square charge radius takes into account the rms charge difference between isotopes. The quantity $< r_c^2 >^{\frac{1}{2}}$ is taken as[80]

$$< r_c^2 >^{\frac{1}{2}} = \begin{cases} 0.84 & A = 1 \\ 2.17 & A = 2 \\ 1.78 & A = 3 \\ 1.63 & A = 4 \\ 2.40 & 6 \leq A \leq 14 \\ .82A^{\frac{1}{3}} + .58 & A \geq 16 \end{cases} \tag{A.9}$$

with $< r^2 >_p = .64$ and $< r^2 >_n = .117$ in units of fm. The above Eq. (A.9) is very accurate for light nuclei but is less accurate for $A \geq 20$. Eq. (A.9) assumes that the nuclear matter distribution is a Gaussian function.

The non-uniform nuclear matter distribution is assumed to be a harmonic oscillator form for light nuclei ($A < 16$). For nuclei heavier than oxygen, the Wood-Saxon form

is assumed. The harmonic oscillator nuclear matter density distribution is taken from a parameterization[81] as

$$\rho(r) = C_0 (C_1 + C_2 r^2) \exp(-C_3 r^2) \qquad A \leq 16 \qquad (A.10)$$

where C_0, C_1, C_2, and C_3 for several nuclei are given in Table A.1 taken from reference 81. The density for nuclei heavier than oxygen is given by

$$\rho(r) = \rho_N \left[1 + \exp\left(\frac{r - R_h}{\alpha}\right)\right]^{-1} \qquad A \geq 16 \qquad (A.11)$$

where R_h is the radius at half-density, and α is the surface diffuseness. The surface diffuseness α is related to the skin-thickness t as $t = 4.4\alpha$, and ρ_N is determined throgh a normaization. The values for the skin-thickness are shown in Table A.2[80]

3. EFFECTIVE TWO-BODY N-N CROSS SECTIONS

Let us consider a reaction $1 + 2 \rightarrow 3 + 4$ with two nucleons in the initial states before the collision, and two nucleons in the final states after the collision. The particle 2 is the constituent nucleon, and the particle 1 is the projectile nucleon. The collision has occurred in a nucleus, and the constituent nucleon is moving with a certain momentum p_2, which is lower than the Fermi-momentum p_F, before the collision. The angular components of the constituent nucleon are θ_2 and ϕ_2. The incoming nucleon with momentum p_1 and angular components θ_1 and ϕ_1 collides with the constituent nucleon and gets scattered out when the phase-space is available. Therefore, the collision is allowed only if the energies of the scattered nucleon and the recoiled nucleon are over the Fermi-energy E_F.

In the rest frame of the nucleus, we transform the projectile nucleon's momentum $\vec{p}_1$ and the constituent nucleon's momentum $\vec{p}_2$ into a coplanar system using sucessive rotational operations. The momenta $\vec{p}_1$ and $\vec{p}_2$ are then mapped into the coplanar

momenta $\vec{k}_1$ and $\vec{k}_2$. The rotation matrices are $R_z(\phi_1)$, $R_y(\theta_1)$, $R_z(\phi_2)$, and $R_y(\theta')$, where θ' is the angle which aligns the direction of the product of two momentum vectors along the z-axis. In the laboratory system, the rotated momentum vectors are given by

$$\vec{k}_1 = \left\{ \frac{-p_1 p_2 \sin\theta_2}{\sqrt{p_1^2 + p_2^2 + 2p_1 p_2 \cos\theta_2}}, 0, \frac{p_1(p_1 + p_2\cos\theta_2)}{\sqrt{p_1^2 + p_2^2 + 2p_1 p_2 \cos\theta_2}} \right\} \qquad (A.12)$$

$$\vec{k}_2 = \left\{ \frac{p_1 p_2 \sin\theta_2}{\sqrt{p_1^2 + p_2^2 + 2p_1 p_2 \cos\theta_2}}, 0, \frac{p_2(p_2 + p_1\cos\theta_2)}{\sqrt{p_1^2 + p_2^2 + 2p_1 p_2 \cos\theta_2}} \right\} \qquad (A.13)$$

where $p_1 = m_1|\vec{v}_1|$ and $p_2 = m_2|\vec{v}_2|$ are the projectile nucleon momentum and the constituent nucleon momentum respectively. The quantities m_1, v_1, m_2 and v_2 are the masses and the velocities of the projectile nucleon and the constituent nucleon respectively.

Using the Galilean transformation, we found the energies of the scattered nucleon and the recoiled nucleon in the center of mass system as

$$\overline{E}_3 = \frac{m_2^2}{(m_1 + m_2)^2} \frac{|\vec{k}_1 - \frac{m_1}{m_2}\vec{k}_2|^2}{|\vec{k}_1|^2} E_1 \qquad (A.14)$$

$$\overline{E}_4 = \frac{m_1 m_2}{(m_1 + m_2)^2} \frac{|\vec{k}_1 - \frac{m_1}{m_2}\vec{k}_2|^2}{|\vec{k}_1|^2} E_1 \qquad (A.15)$$

where the bar "–" denotes the center of mass system. For simplicity, let us use the one-component Fermi-gas model. The masses of the projectile nucleon and the constituent nucleon are assumed to be the same: $m_1 = m_2 = m_N$. Since the interaction is not allowed unless

$$E_3 > E_F \qquad \text{and} \qquad E_4 > E_F \qquad (A.16)$$

we found the differential energy dE_3 of the scattered particle after the collision in terms of the differential scattering angle $d\overline{\Omega}$ in the center of mass system as

$$\mathrm{d}E_3 = \frac{1}{4}\frac{E_1}{\pi}\frac{|\vec{k}_1 - \vec{k}_2|\,|\vec{k}_1 + \vec{k}_2|}{|\vec{k}_1|^2}\,\mathrm{d}\overline{\Omega} \qquad (A.17)$$

where E_1 is the incident energy of the incoming nucleon, and E_3 is the energy of the scattered nucleon.

The cross section is defined as the transition rate Γ_{fi} per unit incident flux per target constituent nucleon. The transition rate for a given reaction process is given by the product of the square of a transition matrix and the available phase-space volume. The transition probability rate is then given by

$$\mathrm{d}\Gamma_{fi} = \frac{2\pi}{\hbar}|T_{fi}|^2\frac{V\lambda}{(2\pi\hbar)^3}\,\mathrm{d}\vec{p}\,\delta(\overline{E}_f - \overline{E}_i) \qquad (A.18)$$

where "i" and "f" denote the initial state and the final state respectively. In Eq. (A.18), V is the nuclear volume, $\hbar$ is the reduced Planck's constant, and λ is the degeneracy. The transition matrix operator T_{fi} can be obtained in free space using the Lippmann-Schwinger equation. In Eq. (A.18), the δ-function is introduced to ensure the energy conservation. In applying the definition of the free N-N cross section, we ignore the energy-dependence of the target constituent nucleon in the transition matrix so that T_{fi} is treated as the "off-the-energy-shell" transition matrix.

From Eq. (A.18), the free two-body N-N cross section is obtained as

$$\sigma_{free} = 4\pi\, m_N\, \lambda\xi \qquad (A.19)$$

where ξ is defined as

$$\xi \equiv V^2\frac{4\pi^2}{\hbar^4}|T_{fi}|^2 \qquad (A.20)$$

Since both the projectile nucleon and the target constituent nucleon are treated to be free in Eq. (A.19), the square of T_{fi} is proportional to the inverse of the nuclear volume. Consequently, the free N-N cross section, given in Eq. (A.19), is independent on the nuclear volume. The free differential N-N cross section is then expressed as

$$\left(\frac{\mathrm{d}\sigma}{\mathrm{d}E}\right)_{free} = \frac{1}{E_1}\sigma_{free} \tag{A.21}$$

where E_1 is the incoming nucleon energy.

In a similar fashion, the effective N-N cross section and the differential spectrum are obtained from Eq. (A.18) by replacing $d\overline{\Omega}$ with $\mathrm{d}E_3$ using Eq. (A.17). The effective N-N cross section is integrated over the Fermi-sphere. Therefore, the effective N-N cross section is obtained in terms of the free cross section as

$$\sigma_{eff} = \frac{3}{4\pi\, p_F^3}\frac{1}{p_1}\sigma_{free}\, I_1(\vec{p}_1,\vec{p}_2) \tag{A.22}$$

where

$$I_1(\vec{p}_1,\vec{p}_2) = \int \mathrm{d}^3k_2 \frac{|\vec{k}_1|^2 + |\vec{k}_2|^2 - 2p_F^2}{|\vec{k}_1 + \vec{k}_2|} \tag{A.23}$$

and the effective differential spectrum is

$$\left(\frac{\mathrm{d}\sigma}{\mathrm{d}E}\right)_{eff} = \frac{3m_N}{2p_F^3}\sigma_{free}\, I_2(\vec{p}_1,\vec{p}_2) \tag{A.24}$$

where

$$I_2(\vec{p}_1,\vec{p}_2) = \int \mathrm{d}^3k_2 \frac{|\vec{k}_1|}{|\vec{k}_1 + \vec{k}_2|} \tag{A.25}$$

The quantity $I_1(\vec{p}_1,\vec{p}_2)$ can be evaluated using the following relations:

$$\begin{aligned} 0 < |\vec{k}_2|^2 < p_F^2 \quad &\text{for} \quad |\vec{k}_1^2| \geq 2p_F^2 \\ 2p_F^2 - |\vec{k}_1|^2 < |\vec{k}_2|^2 < p_F^2 \quad &\text{for} \quad |\vec{k}_1^2| \leq 2p_F^2 \end{aligned} \tag{A.26}$$

The effective cross section is then written as

$$\sigma_{eff} = \sigma_{free} \begin{cases} 1 - \frac{7}{5}\zeta & \text{for } \zeta \leq \frac{1}{2} \\ 1 - \frac{7}{5}\zeta + \frac{2}{5}\zeta^{-3/2}(2\zeta - 1)^{5/2} & \text{for } \zeta \geq \frac{1}{2} \end{cases} \tag{A.27}$$

where $\zeta = \frac{E_F}{E_1}$.

The quantity $I_2(\vec{p}_1, \vec{p}_2)$ is evaluated using a simple quantum statistical concept that the available phase density $\Delta\rho_f$ is given by

$$\Delta\rho_f = \rho_f \begin{cases} 1 - (1 - \frac{\Delta E}{E_F})^n & \text{for } \Delta E \leq E_F \\ 1 & \text{for } \Delta E \geq E_F \end{cases} \tag{A.28}$$

where ρ_f is the phase density of the free N-N scattering, and ΔE is the transferred energy. The constant n is given by $n = \frac{3}{2}$ for a non-relativistic calculation and $n = 3$ for a relativistic case. Therefore, the non-relativistic differential energy spectrum is rewritten as

$$\left(\frac{\mathrm{d}\sigma}{\mathrm{d}E}\right)_{eff} = \frac{1}{E_1}\sigma_{free} \begin{cases} 1 - (1 - \frac{\Delta E}{E_F})^{3/2} & \text{for } \Delta E \geq E_F \\ 1 & \text{for } \Delta E \leq E_F \end{cases} \tag{A.29}$$

4. FREE N-N CROSS SECTION DATA

As shown in Eq. (A.27) and Eq. (A.29), the effective N-N cross section is expressed in terms of the free N-N cross section. We parameterized experimental free N-N cross sections. The total N-N cross section of the proton-proton scattering σ_{pp} is parameterized as

$$\sigma_{pp}(E) = \begin{cases} (1 + 5/E)\{40 + 109\cos(0.199\sqrt{E})\} \\ \qquad \times \exp[-0.451(E - 25.258)] & \text{for } E \geq 25MeV \\ \exp[6.51\exp[-(E/134)^{0.70}]] & \text{for } E < 25MeV \end{cases} \tag{A.30}$$

where E is the energy of the projectile nucleon. For the neutron-proton scattering cross section σ_{np}, we found

$$\sigma_{np}(E) = \begin{cases} 38 + 12500 \exp\left[- 1.187(E - 0.1)^{0.38} \right] & \text{for } E \geq 0.1 MeV \\ 26000 \exp\left[- \left(\frac{E}{0.282} \right)^{0.30} \right] & \text{for } E < 0.1 MeV \end{cases} \tag{A.31}$$

The forward free N-N differential spectrum is written as

$$f_f(E, E') = B \frac{\exp[-B(E' - E)]}{1 - \exp(-BE')} \tag{A.32}$$

where $B = \frac{2mc^2 s}{10^6}$ and mc^2 is the nucleon rest energy, and s is the slope parameter in units of GeV^{-2}. The slope parameter is expressed as

$$s = \begin{cases} 3 + 14 \exp\left(-\frac{E'}{200} \right) & \text{(for p-p scattering)} \\ 3.5 + 30 \exp\left(-\frac{E'}{200} \right) & \text{(for n-p scattering)} \end{cases} \tag{A.33}$$

where E' is the initial nucleon energy in the rest frame of the target constituent nucleon. The backward free N-N differential spectrum has a similar form:

$$f_b(E, E') = \frac{B \exp(-BE)}{1 - \exp(-BE')} \tag{A.34}$$

where we assume for the backward scattering slope parameter the forward value. The forward-to-backward ratio for the neutron-proton scattering is taken as

$$F_B(E') = 0.12 - 0.015E' + \frac{0.41}{1 + \exp[4(E' - 1.2)]} \tag{A.35}$$

where E' in Eq. (A.35) has units of GeV. $F_B(E') = 1$ for the proton-proton scattering. The total free N-N differential spectrum is then expressed as

$$f(E, E') = \frac{B \exp[-B(E' - E)] + F_B(E') B \exp(-BE)}{[1 - \exp(-BE')][F_B(E')]} \tag{A.36}$$

5. EFFECTIVE N-N MEAN FREE PATHS

The mean free path of a nucleon inside a nucleus at a given spatial coordinate $\vec{r}$ is defined by

$$\lambda(\vec{r}) = \{\rho(\vec{r})\,\sigma_{eff}\}^{-1} \tag{A.37}$$

where $\rho(\vec{r})$ is the target nuclear matter density distribution at $\vec{r}$, and σ_{eff} is the effective N-N two-body cross section. On the other hand, in the nucleus-nucleus collision, the mean free path is obtained by averaging the values for different incident nucleons in the target nucleus. Thus, the mean free path for a nucleus-nucleus collision is defined as

$$\lambda(\vec{r}) = \{\sigma_{eff} \int \mathrm{d}\vec{r} \int \rho_P(\vec{r}')\rho_T(\vec{r},\vec{r}')\,\mathrm{d}\vec{r}'\}^{-1} \tag{A.38}$$

where "P" and "T" refer to the projectile nucleus and the target nucleus respectively.

In this work, we obtained the mean free path of the neutron and the proton in ^{40}Ca and in ^{90}Zr with incident energies below 1 GeV using an uniform nuclear matter density distribution. We show the effective mean free path of the neutron in Figure A.1, and the effective mean free path of the proton in Figure A.2. They are compared with the free N-N cross sections. The experimental values and other theoretical values are taken from reference 44. Clearly, there exist quite large differences between the free N-N cross sections and the effective N-N cross sections. Since the proton mean free path is much bigger than the neutron mean free path, one may use an averaged cross section defined by

$$<\sigma>= 2\cdot\frac{Z(A-Z)}{A^2}\sigma_{pp,eff} + \frac{(A-Z)^2Z^2}{A^2}\sigma_{np,eff} \tag{A.39}$$

The effective mean free path of a nucleon is approximately 5 to 7 times bigger than that of the free N-N scattering at around 15 MeV. Between 10 MeV and 50 MeV,

the effective mean free paths drop rapidly. Above 40 MeV, the difference is reduced significantly.

6. CONCLUSION

In this work, we developed a simple kinematical approach to estimate the effective N-N two-body cross section inside a nucleus by using the Galilean transformation. This method will be used to calculate the charged particle emission spectra by the use of a transport algorithm. The present results were previously derived by Kikuchi et al.,[82] Goldberger,[83] and Brown et al.[77] independently. In this work, we started with two arbitrary momentum vectors $\vec{p}_1$ and $\vec{p}_2$ in the nuclear rest frame without aligning the center of mass vector along the z-axis. The present work requires tedious calculations, but it is relatively easy to transform the differential cross sections between the center of mass system and the nuclear rest frame. It can be easily applied to heavy-ion reactions. The relativistic calculation can be achieved in a similar manner using the Lorentz transformation. However, the medium effect is important for a low-energy nuclear reaction, and the Galilean transformation is relatively simple and valid. To improve the present method, the two-component Fermi-gas model should be considered.

Table A.1 Nuclear skin thickness.

$A^{1/3}$	t(fm)	$A^{1/3}$	t(fm)
1.75	1.81	3.46	2.16
2.02	1.75	3.71	1.90
2.19	1.51	3.90	1.69
2.38	1.19	4.13	1.53
2.46	1.01	4.43	1.67
2.66	0.90	4.73	1.77
2.83	1.08	5.11	1.83
2.94	1.44	5.50	1.80
3.03	1.78	5.86	1.77
3.22	2.06	6.00	1.75

Table A.2 Harmonic well matter density parameters.

Nucleus	C_0 fm^{-3}	C_1	C_2 fm^{-2}	C_3 fm^{-2}
^{7}Li	.0282	.906	.148	.380
^{9}Be	.0211	.829	.268	.370
^{11}B	.0225	.739	.419	.425
^{12}C	.0190	.571	.691	.452
^{14}N	.0156	.607	.625	.402
^{16}O	.0112	.591	.636	.350

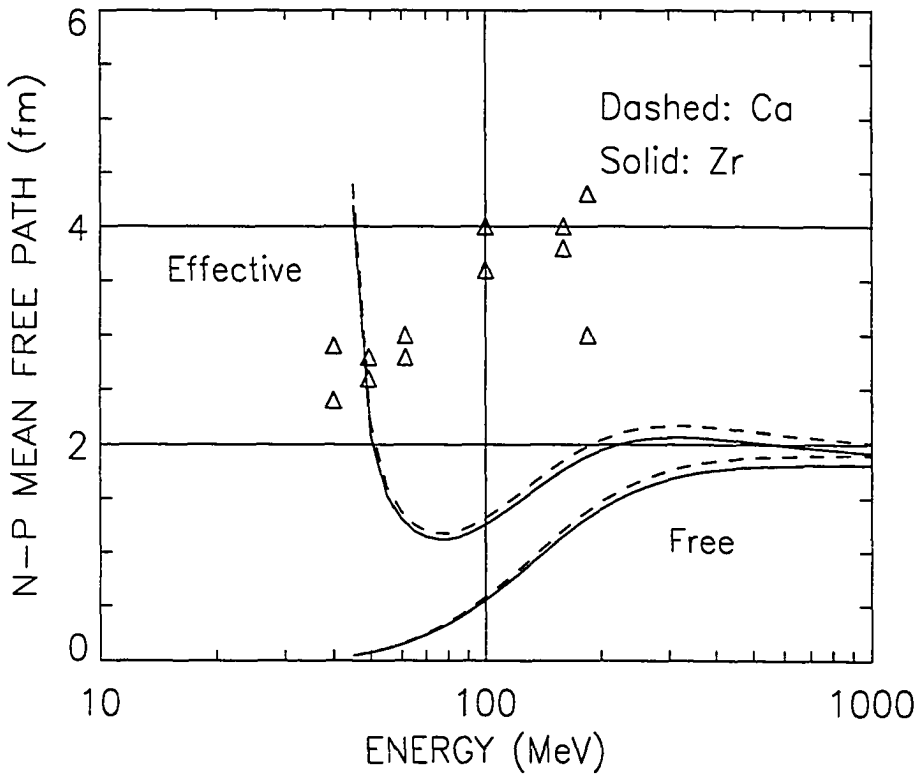

Figure A.1 The effective mean free paths of the neutron in ^{40}Ca (dashed line) and in ^{90}Zr (solid line) as a function of the energy measured from the bottom of the Fermi-sea. The experimental values (triangles) are taken from reference 44.

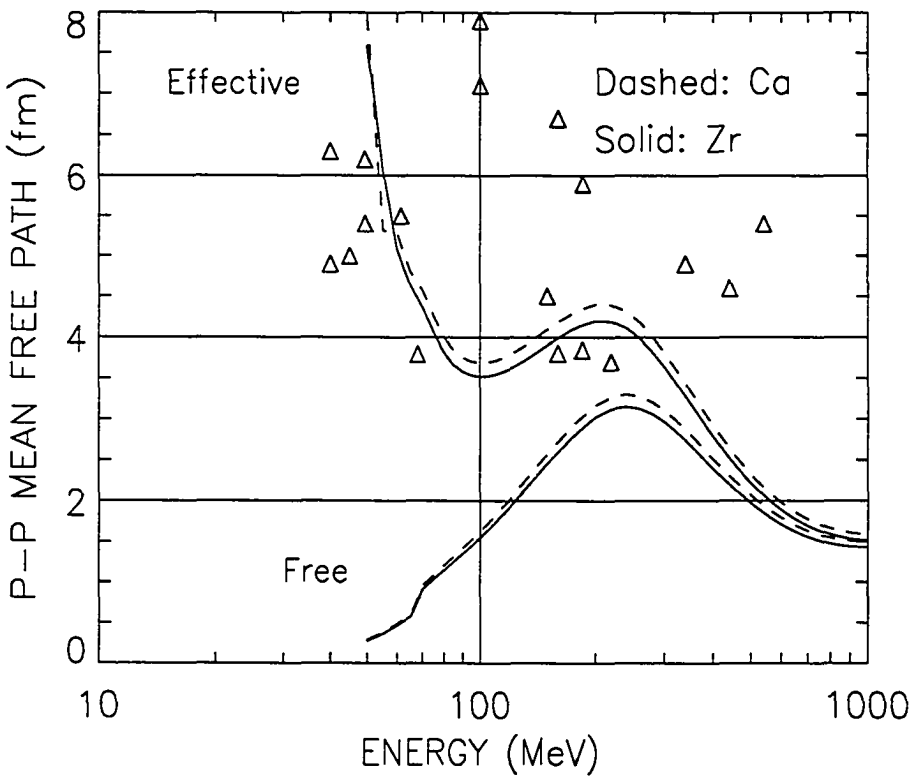

Figure A.2 The effective mean free paths of the proton in ^{40}Ca (dashed line) and in ^{90}Zr (solid line) as a function of the energy measured from the bottom of the Fermi-sea. The experimental values (triangles) are taken from reference 44.

SANG YULL CHUN

Sang Yull Chun was born on February 25, 1958 in Seoul, South Korea, as the second son of Sung Youn Chun and Bong Whowa Chun. He graduated from Seoul High School in February, 1976. He received his Bachelor of Science degree in Physics in February of 1981 from Kyung Hee University in Seoul, South Korea. After serving his mandatory military enlistment in Korea, he attended Purdue University in Indiana and Hampton University in Virginia. In May, 1988, he obtained a Master of Science degree in Physics from Hampton University. He entered Old Dominion University in August, 1988, to work toward his doctorate in physics.

At Old Dominion, his research was primarily concerned with nucleon transport theory and nuclear data base developement for space shielding simulation. Beginning in 1986, he collaborated with scientists formerly of the High-Energy Science Branch of NASA Langley Research Center on these problems. He played a key role in the development of the nucleon transport shielding code BRYNTRN and the heavy-ion transport code HZETRN. He also developed a neutron data base for the transport codes and improved the nuclear fragmentation data base for a low-energy reaction.

His efforts to understand radiation effects have ranged from the development of a computational method for estimating the KERMA factors in neutron dosimetry to the study of intra-nuclear cascade theory. In addition to his early work on estimating particle emission spectra arising from nucleon transport inside nuclei, he has also investigated the longitudinal beam instability in heavy-ion fusion drivers and the generalized oscillator strength for helium-like ions.

He has co-authored many technical articles and NASA publications. He has spent many years as a research assistant and as a teaching assistant, including a brief time as an instructor at Hampton University. Mr. Chun is also a member of American Physical Society.